

RETRIEVING SURFACE VARIABLES BY
INTEGRATING GROUND MEASUREMENTS AND
EARTH OBSERVATION DATA IN FOREST CANOPIES

A CASE STUDY IN SPEULDERBOS FOREST, THE
NETHERLANDS

Kitsiri Weligepolage

Examining committee:

Prof.dr.ir. M.G. Vosselman
Prof.dr. F.D. van der Meer
Prof.dr. J. Sobrino
Prof.dr.ir. E.J. Moors

Dr. F.C. Bosveld
Prof.dr. Y.Ma

University of Twente
University of Twente
University of Valencia
Alterra - Wageningen UR,
Free University of Amsterdam
KNMI
Chinese Academy of Sciences

ITC dissertation number 269
ITC, P.O. Box 217, 7500 AE Enschede, The Netherlands

ISBN 978-90-365-3876-3
DOI 10.3990/1.9789036538763

Cover designed by Benno Masselink
Printed by ITC Printing Department
Copyright © 2015 by Kitsiri Weligepolage



UNIVERSITY OF TWENTE.

ITC FACULTY OF GEO-INFORMATION SCIENCE AND EARTH OBSERVATION

RETRIEVING SURFACE VARIABLES BY
INTEGRATING GROUND MEASUREMENTS AND
EARTH OBSERVATION DATA IN FOREST CANOPIES

A CASE STUDY IN SPEULDERBOS FOREST, THE
NETHERLANDS

DISSERTATION

To obtain
the degree of doctor at the University of Twente,
on the authority of the Rector Magnificus,
prof.dr. H. Brinksma,
on account of the decision of the graduation committee,
to be publicly defended
on Thursday 16 April 2015 at 14.45 hrs

by

Kitsiri Weligepolage

born on 06-10-1966

in Colombo, Sri Lanka

This thesis is approved by
Prof.dr. Zhongbo (Bob) Su, promoter

Acknowledgements

This dissertation would not have been possible without the support and cooperation of many people to whom I am deeply indebted. I use this opportunity to express my gratitude to each and every one though I mention only few names in this acknowledgement.

First and foremost, I would like to express my heartfelt gratitude to my promoter, Prof. Bob Su, for guiding me throughout the extended period of my research both internally and away from ITC. His endless support and encouragements together with excellent scientific contribution shaped the outcome of this work. Bob's doors were always opened for quick discussions and whenever I contacted via emails for a feedback, he responded within a short time amid his busy schedule. I am truly indebted to Bob for his immense patience and generosity extended to me during this period of PhD research.

Also I am greatly indebted to Dr. Ambro S.M. Gieske for his valuable advises on technical matters which helped me to take this research in the right direction. His thorough knowledge on physics, remote sensing, atmospheric modelling and computer programming helped me immensely to improve the quality of my work. Also his contributions during the preparation of journal articles specially his meticulous correction of draft manuscripts allowed me to produce some quality outputs. It is regrettable that I was not able to receive his valuable contribution during the final phase of thesis writing.

I gratefully acknowledge the financial support I received from the Faculty of Geo-information Science and Earth Observation, University of Twente. I also thank Irrigation Department of Sri Lanka for granting me study leave enabling me to pursue this research. Also I thankfully acknowledge the administrative staff of Bureau of Education and Research Affairs, particularly Ms. Loes Colenbrander, Ms. Bettine Geerdink, Ms. Theresa van den Boogaard, Ms. Marie Chantal Metz, Job Duim, Benno Masselink, and Ms. Marion Pierik of Financial and Economic Affairs Division of ITC, for their continuous support and help. Many thanks go to Ms. Anke de Koning and Ms. Tina Butt Castro administrative secretaries of Water Resources Department.

Many thanks to the academic staff of Water Resources Department particularly the organizers of EAGLE 2006 field campaign, Wim Timmermans, Remco Dost, Joris Timmermans and Christiaan van der Tol for their technical support in acquiring the ground data used in this research. Also I am very happy to have met many friends both national and international at Enschede during the period I spent for my PhD studies. I thank each and every one for

the friendship bestowed and sharing your time with me. Because of your company, life at ITC was always a pleasant and enjoyable one for me.

Back at home I would like to gratefully acknowledge the support of my superiors and colleagues at Irrigation Department, Sri Lanka. I specially thank Eng. W. Gamage and Dr. Palitha Bandara for not only facilitating my leave from the job at Irrigation Department but also for their continuous moral support and encouragements to achieve this target.

Finally I want to thank my family members, my beloved wife Jayani and my dearest children Dulana, Dinoki and Thevinu for your inspiration and love throughout this journey. Words cannot express my gratitude to you all for the sacrifices you made on behalf of me. I believe that all the hard work and sacrifices have finally paid off.

Table of Contents

Acknowledgements.....	i
Table of Contents.....	iii
List of figures.....	v
List of tables.....	viii
1 Introduction.....	1
1.1 Current progress and future needs of EO.....	2
1.2 EAGLE 2006 Field Campaign.....	3
1.3 Problem Statement.....	4
1.4 Statement of Objectives.....	5
1.5 Study Area Description.....	6
1.6 Structure of the thesis.....	8
2 Estimation of canopy aerodynamic roughness using morphometric methods.....	11
2.1 Introduction.....	13
2.2 TLS and ALS Data.....	15
2.3 Some basic concepts & terminology.....	17
2.3.1 Models to estimate roughness parameters.....	17
2.3.2 Generation of Canopy Height Models (CHM).....	19
2.3.3 Estimation of roughness parameters using CHMs.....	24
2.3.4 Estimation of obstacle parameters (d_0) and (h).....	24
2.4 Determination of aerodynamic parameters.....	27
2.4.1 Representation of roughness elements using basic geometric shapes.....	30
2.4.2 Determination of d_0 and h^* using cumulative area-height relationship.....	31
2.5 Conclusions.....	34
3 Effect of Sub-layer corrections on the roughness parameterization of a Douglas fir forest.....	37
3.1 Introduction.....	39
3.2 Experimental Setup.....	41
3.3 Modified Monin-Obukhov similarity theory.....	43
3.3.1 Different forms of RSL profile functions.....	44
3.4 Estimation of roughness parameters for neutral stability.....	46
3.4.1 Selection of data for near-neutral stability.....	47
3.4.2 Correction for roughness sub-layer effect.....	48
3.5 Estimation of roughness parameters using EC measurements.....	49
3.5.1 Selection of data for unstable conditions.....	50
3.5.2 Estimation of sensible heat flux.....	50
3.5.3 Evaluation of coefficients.....	51
3.5.4 Estimation of d_0 and z_0	51
3.6 Results and Discussion.....	52
3.7 Conclusions.....	61
4 Effect of spatial resolution on estimating surface albedo.....	65
4.1 Introduction.....	67
4.2 Data.....	68
4.2.1 Imagery dataset.....	68
4.2.2 Tower-based surface radiation measurements.....	70
4.3 Theory and Methods.....	71

4.3.1	Tower-based surface albedo estimation	71
4.3.2	Image pre-processing	71
4.3.3	Estimation of broadband surface albedo	73
4.3.4	Forest species classification using AHS image	74
4.3.5	Semivariograms.....	75
4.3.6	Characterizing forests spatial structure.....	76
4.4	Results.....	77
4.4.1	Outputs of MODTRAN interrogation technique	77
4.4.2	Tower-based surface albedo results	80
4.4.3	Spatial variability in canopy surface albedo estimated with image data.....	80
4.5	Discussion	83
4.5.1	Analyses of temporal variability of tower-based albedo	83
4.5.2	Analysis of forest class-sensor dependency	83
4.5.3	Analysis of spatial structure and effect of pixel size	85
4.6	Conclusions	88
5	Retrieving directional temperature using multiplatform thermal data ...	91
5.1	Introduction.....	93
5.2	Extraction of atmospheric parameters.....	94
5.2.1	Inversion of Land Surface Temperature	95
5.2.2	Temperature and Emissivity Separation algorithm.....	96
5.3	Measurements	98
5.3.1	Tower-based radiometric measurements	98
5.3.2	Contact temperature measurements	100
5.3.3	Airborne data acquisition.....	100
5.4	Results.....	102
5.4.1	Output of MODTRAN4	102
5.4.2	Tower-based temperature measurements.....	104
5.4.3	Comparison of tower measurements vs. LST	107
5.5	Summary and Conclusions	110
6	Conclusions and Recommendations.....	113
6.1	Conclusions	114
6.2	Suggestions for further research	116
	Bibliography	119
	Summary.....	129
	Samenvatting	131
	ITC Dissertation List	134

List of figures

Figure 1-1: Location of the Speulderbos experimental site; the right panel shows the forest border and the measurement tower located in the centre. ..	7
Figure 1-2: Forest stand distribution of the surrounding area of the measurement tower (after Bosveld, 1997). Thick and thin lines represent minor roads and stand borders respectively. The diamond in the centre represents the tower.	8
Figure 2-1: Terrestrial Laser Scanning (TLS) at Speulderbos. Panel (a) shows the scaffolding Tower and the vertical movement of the scanner. Panel (b) shows the plan view from three directions (Tower and two ground locations TLS1, TLS2).	16
Figure 2-2: Digital Elevation Model created by interpolating the ALS terrain elevation data and the power semi-variogram model used for ordinary kriging.....	20
Figure 2-3: Panel (a) shows correlation between TLS and ALS canopy heights for 226 data points and Panel (b) shows histograms of TLS and ALS canopy heights (bin size 2 m).	21
Figure 2-4: Histogram of entire TLS canopy data set (bin size 1 m) showing bimodal character.	22
Figure 2-5: ALS Canopy Height Models interpolated by ordinary kriging with the exponential semi-variogram models with nugget 7 (panel a) and nugget 0 (panel b).	23
Figure 2-6: TLS Canopy Height Models. (panel-a) Gaps filled by IDW and (panel-b) Running a Median filter (5X5 pixels). The dashed lines indicate the distribution of transects for two principal directions.	24
Figure 2-7: Plot of the average obstacle density versus moving average number. Solid lines indicate the mean λ values for 10 profiles. Dashed lines show the range of λ for each curve.	26
Figure 2-8: Sensitivity of d_0 and z_0 estimated from different models with respect to λ	30
Figure 2-9: Area height relationship of the CHM showing the fitted geometrical models. The solid lines show the values obtained from the canopy height models. Short dashed lines indicate the paraboloid model. Long dashed lines indicate the conical model.....	32
Figure 2-10: A typical crown section fitted with cone in hexagonal packing and paraboloid in square packing shapes. TLS point data for two principal directions are compared.	34
Figure 3-1: Comparison of wind speed at 35m and 47m at Speulderbos	43
Figure 3-2: Comparison of wind direction at 35m and 47m at Speulderbos .	43
Figure 3-3: Predicted wind profiles for neutral conditions. (a) Forward calculations with different $\psi_u(z)$. Dotted line: Mölder et al. (1999); dashed line: De Ridder (2010); dash-dotted line: Harman and Finnigan (2007); solid line: the simple logarithmic profile. (b) Different solutions. Solid line: the simple exponential solution; dotted line: non-iterative solution by Nakai et al.	

(2008a); dashed line: fully iterative solution (proposed here). Two filled circles indicate the wind speed corresponding to measuring heights.....53

Figure 3-4: The observed linear relationship between d_0 and z_0 estimated for neutral stability. (a) No RSL corrections; (b) With RSL corrections- $\psi_u(z)$ of Mölder et al. (1999); (c) With RSL corrections - $\psi_u(z)$ of Harman and Finnigan (2007); (d) With RSL corrections - $\psi_u(z)$ of De Ridder (2010). Dashed lines: regression by ordinary least square technique. Solid line: described linear equation obtained with geometric mean regression technique.....54

Figure 3-5: Displacement height d_0 (in panel a) and Aerodynamic canopy height h_a (in panel b) as a function of h_c for selected forest studies. Solid lines show the described quadratic equations. Crosses show the result of the present study. The results in the same study area: the 1989 study by Bosveld (1997) and the present study carried out in 2006 are enclosed with circles.55

Figure 3-6: Comparison of vertical profiles of mean wind speed above the canopy to average observations in neutral conditions. Solid line: predicted profile using the $\psi_u(z)$ given by Harman and Finnigan (2007); dashed line: predicted profile using the $\psi_u(z)$ given by De Ridder (2010); dotted line: the extrapolated surface layer profile. Filled circles denote the average observed values at 35 m and 47 m above the ground where the error bars denote the standard deviation.57

Figure 3-7: Comparison of eddy covariance H vs. estimated H using σ_T and u measurements as in option A.60

Figure 3-8: Comparison of eddy covariance H vs. estimated H using σ_T and σ_w measurements as in option B.60

Figure 3-9: Comparison of H estimated from options A (horizontal) and B (vertical).61

Figure 4-1: Land cover distribution of the study area obtained by the supervised classification using AHS low-altitude image data. The areas denoted by (a), (b) and (c) were used to calculate experimental semivariograms for needleleaf, broadleaf and mixed forest classes respectively.....75

Figure 4-2: Spectra of six effective atmospheric parameters derived using MIT for different Sun-sensor geometries for (a) AHS low-altitude flight and (b) ASTER image.....78

Figure 4-3: Band averaged values of six effective atmospheric parameters for (a) AHS band 1 to 20 and (b) ASTER band 1 to 9.....79

Figure 4-4: (a) Temporal distribution of surface albedo estimated with tower-based measurements over the needleleaf forest from DOY-159 to 165. (b) Diurnal variation of half hourly mean albedo estimated for the same period.80

Figure 4-5: Albedo spatial variability of the study area estimated with image data. Histograms and descriptive statistics for albedo distribution at different

spatial resolutions. (a) 2.5 m AHS low-altitude; (b) 7.5 m AHS high-altitude (c) 15m ASTER	82
Figure 4-6: Albedo spatial distribution of different forest classes obtained using (a) AHS low-altitude image; (b) AHS high-altitude image; (c) ASTER image.....	84
Figure 4-7: Experimental semivariograms obtained for (a) needleleaf forest; (b) Mixed forest; (c) broadleaf forest classes fitted with spherical and exponential models. The range and sill values of semivariogram models are listed for each forest class.	86
Figure 4-8: Comparison of spatially averaged albedo of needleleaf forest, estimated with different images against the half hourly averages of tower-based albedo estimated for sensor overpass days. The symbols open circle, square and the triangle denote ASTER, AHS high-altitude and AHS low-altitude based spatial averages respectively. The error bars denote the standard deviations.	88
Figure 5-1: Spectral response functions of AHS thermal bands 71 to 80 with atmospheric transmissivity for different flight altitudes.	102
Figure 5-2: Basic output parameters of MODTRAN 4 run	103
Figure 5-3: Atmospheric parameters from MODTRAN 4 outputs	103
Figure 5-4: AHS Band specific atmospheric parameters	103
Figure 5-5: Tower-based radiometric temperature at two different view directions.....	104
Figure 5-6: Contact temperature measurements of canopy components all at 24 m level.....	105
Figure 5-7: LST distribution from AHS images; (a) & (b) show the nadir view of the tower location acquired by high-altitude and low-altitude flights respectively. (c) & (d) show the off-nadir view of the same acquired by low-altitude flights.	106
Figure 5-8: Spatial and temporal distribution of LST of the Douglas fir forest (shown here is an area of approximately 100 m X 100 m enclosing the tower) Panels (a) to (f) indicate the local time of image acquisition. The cross in the middle denotes the location of the Speulderbos tower.	107
Figure 5-9 : Comparison of tower-based vs. remotely sensed temperature of Douglas fir forest. The tower-based observations are one minute averages of needle temperature at 24 m and radiometric temperature with off-nadir view. The LST from AHS images (red triangles) are the spatial averages of the area of interest. The error bars indicate the standard deviation of temperature for same.....	109
Figure 5-10 : Comparison of tower-based vs. remotely sensed temperature of Douglas fir forest. The tower-based observations are one minute averages of trunk temperature at 17 m and radiometric temperature with nadir view. The LST from AHS images (red triangles) are the spatial averages of the area of interest. The error bars indicate the standard deviation of temperature for same.....	109

List of tables

Table 2-1: Statistical Summary of TLS-CHM derived canopy surface features for different directions.	26
Table 2-2: Statistical Summary of ALS-CHM derived canopy surface features for different directions	27
Table 2-3: Summary of results for spatially average canopy height and obstacle density.....	27
Table 2-4: Estimated roughness parameters using original model parameters	28
Table 2-5: Comparison of model parameters in Raupach (1992) and Raupach (1994) models.....	29
Table 2-6: Estimated roughness parameters using proposed model parameters	29
Table 2-7: Results obtained with different geometrical models after fitting the TLS-CHM	33
Table 2-8: Results obtained with different geometrical models after fitting the ALS-CHM	33
Table 3-1: Overview of the instrumentation at the Speulderbos location.....	42
Table 3-2: Comparison of roughness sub-layer effect on aerodynamic parameters using different RSL corrections.	54
Table 3-3: The best performing values of d_0 and z_0 estimated by varying the coefficient C_1	58
Table 3-4: The best performing values of d_0 , a and b estimated by varying the coefficient C_1	59
Table 3-5: Model results for recommend coefficients and best performing values of roughness parameters.	59
Table 4-1: AHS spectral information for Port 1 (0.43 – 1.03 μm) and the corresponding E_{SUN} values and weighting coefficients.....	69
Table 4-2: ASTER spectral information for Visible and Near-Infrared group (0.52 – 0.86 μm) and the corresponding E_{SUN} values and weighting coefficients.....	70
Table 4-3: The observation conditions of air-borne and satellite imageries..	70
Table 4-4: Main input parameters used for MODTRAN4 - tape 5 card	73
Table 4-5: Comparison of spatially average albedo in needleleaf forest versus tower-derived albedo estimates.....	88
Table 5-1: Various thermal instruments and their measurement frequency .	99
Table 5-2: Main technical specifications of field radiometers	100
Table 5-3: Description of NTC sensors attached to different parts of the canopy	100
Table 5-4: Observation details of AHS images acquired over Speulderbos area	101
Table 5-5: Spectral characteristics of AHS thermal bands.....	101

Table 5-6: Spatial statistics of AHS derived LST estimates for the area of interest.....	108
--	-----

1 Introduction

Understanding the interaction between the Earth's surface and the lower part of the atmosphere is of paramount importance for many applications in meteorology, hydrology and related fields. It is well-known that this interaction is determined to an important extent by atmospheric state, exchange processes, and land-surface properties across the land atmosphere interface (Stull, 1988). Statistics of global land cover show that 30% of the dry land area of the Earth's surface is covered by forest canopies (FAO, 2012). There is ample evidence, largely from modelling studies, which suggests that forests have a noticeable impact on the atmospheric boundary layer and precipitation patterns (Dolman et al., 2004). According to Pitman et al. (1999) most of the evidence for effect of land-surface properties on the atmosphere at a range of temporal and spatial scales, is available from global scale modelling studies. Dolman et al. (2004) have emphasized that, mostly the evidence of forest-atmosphere interaction comes from global circulation model (GCM) modelling studies, in which one land cover type, for instance, grassland, is replaced by another, for instance, forest. More recently Teuling et al. (2010) have analyzed the contrasting response of forest and grassland energy exchange to heatwaves in Europe and have concluded that forest contributes to increased temperature in the short term but mitigates the impacts of extreme events.

Forests are noticeably different from those of vegetation of lower density and height in various physical characteristics (see e.g. Dolman et al., 2003). In general forests are tall and for that reason forests carry more leaf area per unit ground surface where the leaf-area densities typically exceed 3. Because of the tallness and leaf-area density, aerodynamic and radiative properties of forests are fundamentally different from lower vegetations such as grassland and agricultural crops. Besides the leaf area density the distribution of leaf area with height and the spectral characteristics and orientation of leaves affect the transmission of radiation and the reflectivity of forests. Apart from that, forests are more effective in capturing short-wave radiation than lower vegetation (e.g. Oke, 1978), an important effect of forest on the atmosphere is enhanced recycling of water through evaporation, i.e. the atmospheric moisture-precipitation chain. Many studies have demonstrated the strong effects of surface heterogeneity on factors such as radiation temperature (Bosveld et al., 1999), roughness length (Oleson et al., 2000), and albedo (Rowe, 1993) which are the primary inputs for quantifying the land-atmosphere interactions, particularly the exchange of energy and mass between the land surface and the atmosphere.

Several studies have indicated the importance of forests in temperate and boreal climates for the global carbon cycle, since they currently contain 16-

24% of the world's soil carbon (e.g. Sellers et al., 1996). Therefore boreal ecosystems have been constantly investigated by Earth observing scientific community particularly interested in quantifying the land surface atmosphere exchanges. Nonetheless unresolved issues associated with surface properties pose a major challenge in such ecosystems particularly for modelling surface atmosphere interactions. Bonan et al. (1993) have shown that inherent heterogeneity in boreal coniferous forests have a highly nonlinear effect on model estimated fluxes of sensible heat and latent heat with errors as high as 40%. Many studies have emphasized the importance of accurate characterization of surface parameters in forest ecosystems, in order to effectively represent the surface heterogeneity in models used to understand land-surface, processes in these regions. However accurate surface parameterization needs adequate observations to capture the surface variability and to obtain high accuracies in heterogeneous surfaces with a limited number of ground-based measurements is a challenging task. On the other hand Earth observation (EO) using remote sensing (RS) techniques offer the possibility to capture surface features at global scale and in combination with sparse ground observations these techniques are capable of estimating surface parameters with a reasonable accuracy.

EO is a branch of Earth science which is relatively inexpensive and fast for estimating land surface characteristics across broad geographic regions and temporal scales. RS techniques started in early sixties with the NOAA/AVHRR, METEOSAT and LANDSAT programs. Since then, the capacity of EO data to monitor land surface processes has been developed to a great extent through a number of such programs. EO data acquired by means of sensor on-board satellites primarily provide consistent and frequent observations of spectral reflectance and thermal emittance at local, regional and global scale (Sellers et al., 1990). With the increasing ability to estimate the land surface parameters such as surface albedo, land surface temperature and emissivity using the EO data, important progress has been made in the improvement of surface flux parameterization processes in hydro-meteorological models. Especially by integrating EO data with minimal in-situ measurements to suitable models, Earth system scientists have developed a variety of surface energy balance algorithms to compute spatially distributed surface fluxes. Pioneering work of Kustas et al. (1989), Menenti et al. (1991), Menenti and Choudhury (1993), Bastiaanssen et al. (1998), Roerink et al. (2000) and Su (2002) are few examples for such surface energy balance algorithms.

1.1 Current progress and future needs of EO

The capacity of existing EO missions for research and operational applications is being constantly improved by introducing new scientific and operational satellites with state-of-the-art technology. Nevertheless, in order to

understand the full potential of these novel missions for operational applications carrying out experimental work at ground level is imperative. The importance of complementing ground measurements with EO data for better quantification of land-atmosphere interactions has been highlighted in recent reviews on the EO data applications (Fernandez-Prieto, et al., 2013). They have emphasized that the integrated use of EO data and ground-based measurements will lead to improved estimates of spatially distributed surface fluxes resulted from such interactions. In the coming years advanced EO missions to enhance the capacity of monitoring land surface and atmosphere are planned to be launched by space agencies. In order to exploit such increasing multi-mission observational capacity, the combined effort of EO scientists and modelling community in developing novel techniques by integrating advanced EO data with in-situ observations is indispensable. Considering the fact that a range of models and algorithms presented by the EO scientists are available, conducting studies to compare and contrast the results to understand the robustness of these models, constrains and limitations of algorithms is a future challenge.

It has been realized that enhanced knowledge of inconsistencies due to scale issues between the in-situ measurements and multi-scale EO data acquired using different platforms will provide more chances to build better models and obtain reliable outputs. Principally by reducing discrepancies due to scale issues amongst the ground-based measurements and multi-scale EO data, existing incompatibilities between the biophysical models and the EO data retrieved from satellites can be minimized. In order to accomplish the task, dedicated multi-scale data acquisition experiments facilitating the analysis of inter-scale relationships between ground-based point measurements including measurements made aloft using tall towers bridging the gap between surface and airborne measurements, need to be promoted. More emphasis should be made on experimental work targeting multi-angle airborne data acquisitions at different resolutions parallel to the multi-sensor space borne observations. Owing to various complexities in obtaining necessary observational capacity along with various difficulties in coordinating intensive field campaigns, very few have been successfully conducted in the past. EAGLE 2006 is one such field campaign executed with internationally coordinated effort targeting forests and grasslands.

1.2 EAGLE 2006 Field Campaign

EAGLE2006 is a multi-purpose, multi-angle, multi-sensor and multi-platform data acquisition campaign performed over grassland and forest sites in central part of the Netherlands. During this intensive field campaign different airborne sensors including an optical imaging sensor, an imaging microwave radiometer, and a flux airplane were used for data acquisition and to collect

extensive ground measurements simultaneously over grassland (at Cabauw) and two forest sites (at Loobos & Speulderbos), in addition to acquisition of multi-angle and multi-sensor satellite data. EAGLE2006 campaign is an internationally coordinated scientific endeavour where 67 people from 16 different institutions coming from 6 different countries got involved for data acquisition. The datasets provide a unique opportunity to address following general objectives having listed in the final report of EAGLE2006 campaign (Timmermans et al., 2008) and subsequently by Su et al. (2009) as;

1. Advancement of process understanding in description of radiative and turbulent processes in land-atmosphere interactions.
2. Validation of primary bio-geophysical parameters derived from satellite data using in-situ and airborne data.
3. Development of operational algorithms to extract land surface parameters and heat fluxes from the future missions.

Furthermore the EAGLE2006 campaign specifically aimed at some of the programmatic needs of Sentinel-1 and 2 mentioned in the EAGLE 2006 final report (Timmermans et al., 2008) as follows.

1. To assess the impact of Sentinel-1 and Sentinel-2 sensor and mission characteristics for land applications (land use mapping, parameter retrieval) over forest and grassland.
2. To provide a basis for the quantitative assessment of sensor or mission trade-off studies, e.g. spatial and radiometric resolution.
3. Simulate Sentinel-1 and Sentinel-2 image products over the land (forest and grassland).

The EAGLE2006 dataset also includes ground-based radiometric measurements both in solar range and thermal domains, a range of micro-meteorological measurements, surface energy budget data (using both Eddy Covariance (EC) system and Large Aperture Scintillometer (LAS)), contact temperature measurements, forest biophysical parameters, surface emissivity and terrestrial laser scanning data for calibration and validation of airborne and space borne sensor observations, and also to be used as input parameters and validation data for modelling activities.

1.3 Problem Statement

Land surface roughness, albedo and temperature are three of the key spatially distributed variables for modeling land-atmosphere interactions. Conventionally these variables are estimated using synoptic measurements made at ground observation points. However these point estimates do not represent the regional distribution of surface variables which are highly

variable in space and time. EO data with increased spatial and temporal resolution provide land surface characteristics over the scales of space and time. The variability associated with key land surface characteristics can be easily captured if the variables can be linked to EO data distributed in space and time. After decades of experimental work many natural surfaces have been studied to establish relationships between surface specific point estimates and EO data. In spite of this, experimental work performed over tall forest canopies is rare mainly because it is hard to find extensive homogeneous forests, costly to erect tall towers, and difficult to maintain the very high accuracy requirements of the observations. Moreover most of the experimental work performed over tall forest canopies has focused primarily on profile and turbulent flux measurements and less attention has been paid to complement the ground based observations with EO data from satellites or airborne platforms. Under these circumstances we are motivated by the comprehensive and high-quality dataset acquired during EAGLE2006 campaign to embark on a complementary analysis covering a forest surface.

1.4 Statement of Objectives

The general objective of this study is to fill the above mentioned gaps by integrating tower-based measurements with EO data for estimating spatially and temporally distributed surface variables of a forest canopy for improved quantification of surface-atmosphere interactions.

In accordance with the general objective, the specific objectives are:

1. To make use of high resolution Terrestrial Laser Scanning (TLS) data together with Airborne Laser Scanning (ALS) data to digitally map the upper canopy surface of a Douglas fir forest.
2. To develop a framework to extract canopy morphometric details using the digital canopy height model (CHM) with the aim of estimating aerodynamic roughness of a region covered by the forest.
3. To evaluate two aerodynamic approaches within the context of estimating roughness parameters of a moderately dense forest using measurements made in the roughness sub-layer.
4. To examine the spatial and temporal variability of surface albedo of a needleleaf forest stand using atmospherically corrected multi-scale remote sensing data and in-situ solar radiation measurements.

5. To examine the effect of spatial resolution in discriminating albedo characteristics of three distinct forest classes by quantifying the spatial structure of forest classes using a variogram analysis.
6. To demonstrate the retrieval process of directional land surface temperature from Airborne Hyperspectral Scanner (AHS) data and to validate against the in-situ temperature measurements collected during the image acquisition.

1.5 Study Area Description

The selected study area the Speulderbos forest is a well-known research site, located in the central part of the Netherlands near the village of Garderen (52° 15'N, 5° 41'E). In this location a 46 meter high micro-meteorological measurement tower (Speulderbos tower) operated by the National Institute for Public Health and the Environment (RIVM) is placed within a 2.5 ha Douglas fir (*Pseudotsuga menziesii*) stand surrounded by a large forested area (see Figure 1-1)). The experimental site has been extensively studied by many Dutch researchers (see e.g. Bosveld, 1999). During the EAGLE 2006 field campaign conducted in June 2006, extensive measurements of atmospheric boundary layer (ABL) variables were made at the Speulderbos tower in addition to the various measurements of biophysical parameters carried out within the Douglas fir forest (Su et al., 2009). The forest has been planted in 1962, and stand density of 780 trees per hectare was reported in early nineties without a significant understory. Based on the 1993 observations, Dorsey et al. (2004) reported that there was a high degree of canopy closure with no tree foliage below 10 m. The single sided leaf area index (LAI) as reported in Bosveld (1999) based on a research carried out in 1991 is about 10 m²m⁻². More recently, Van der Tol et al. (2009) reported an optical LAI of approximately 5 m²m⁻² based on Photosynthetically Active Radiation (PAR) measurements above and below the canopy. An analysis of a longer time series with a model that includes crown clumping resulted in an average optical LAI of 3.4 for the years 2008-2010 (van der Tol, unpublished data).

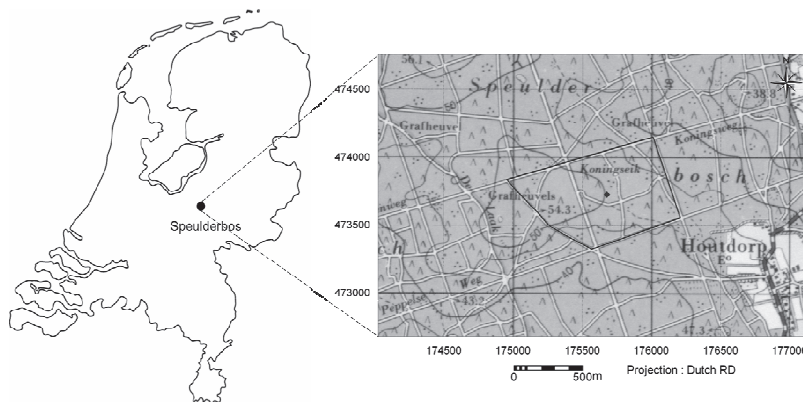


Figure 1-1: Location of the Speulderbos experimental site; the right panel shows the forest border and the measurement tower located in the centre.

The mean tree height of the Douglas fir stand which was about 22m in early nineties, increased to 32m in 2006. The surrounding forest stands have typical dimensions of a few hectares and varying tree heights. Dominant species in the neighborhood of the Douglas fir stand are Japanese Lark (*Larix pinaceae*), Beech (*Fagus sylvatica*), Scotch Pine (*Pinus sylvestris*) and Hemlock (*Tsuga canadensis*). The vegetation consists of forest at distances of one to several kilometers (Bosveld, 1997). The topography of the study area is slightly undulating with elevation varying from 30m to 50m. Land cover data, originating from the Corine Land cover database (EEA, 1992), is available for the study area in the ArcView Shape format. Figure 1-2 shows the forest stand distribution of the study area in the vicinity of the measurement tower. The vegetation around the tower consists of forest spreading to all the directions for several kilometers except to the east where the forest extends about 1.5 km before meeting a heath area. Apart from the small clearing located 100 m to the north of Douglas fir stand, the tree height variation in rest of the surrounding forest stands within a distance of 200 m is small. By means of an aerial view on the Speulderbos tower at 46 m elevation, it appears that the upwind terrain of the south-east to south-west sector consists of forest stands with somewhat shorter trees compared to the Douglas fir stand. For remaining wind sectors, the tree height of forest stands within the upwind terrain is not much different from the Douglas fir stand.

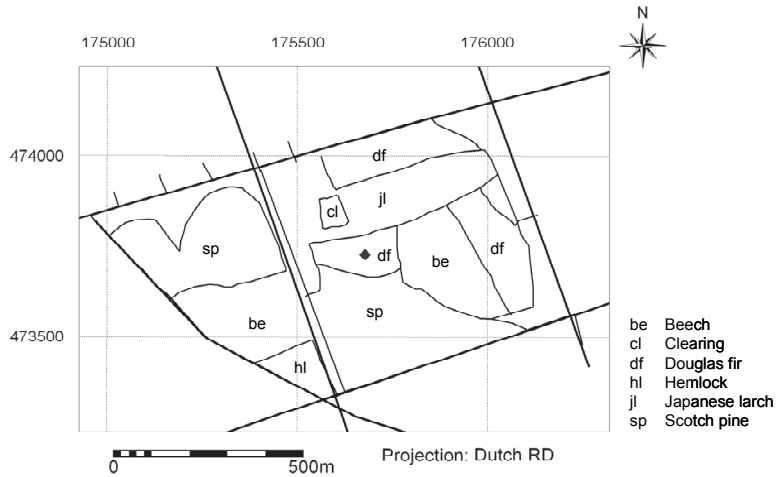


Figure 1-2: Forest stand distribution of the surrounding area of the measurement tower (after Bosveld, 1997). Thick and thin lines represent minor roads and stand borders respectively. The diamond in the centre represents the tower.

In order to understand the prevailing fetch condition for flux measurements, a source area analysis is useful. Previous analysis of flux footprint at Speulderbos tower by Bosveld (1997) has indicated that when the measurements are made 12 m above the forest canopy, 50% of the flux at the sensor location originates from upwind direction of approximately 80 m distance for neutral conditions. However the footprint models used by Bosveld (1997) are intended to be used in the surface-layer, thus for measurements made in the Roughness Sub-Layer, the source areas should be somewhat closer to the measuring points (because of the enhanced mixing compared to the surface-layer) than the estimated value particularly for neutral and unstable conditions. The climate of the area is maritime with year-round rainfall. The mean annual air temperature of the study area is about 4^o C whereas the mean monthly temperature in June is about 16^o C. The soil in the area is a well-drained Haplic Podzol, consisting of fluvial deposits with textures ranging from fine sand to sandy loam. The water table is 40 m below the surface. The 30-year mean annual rainfall is 834 mm (Tiktak and Bouten, 1992; Van der Maas, 1990).

1.6 Structure of the thesis

This thesis consists of six chapters in total. Three of the four core chapters have been published as peer-reviewed papers (Chapter 2, 3 and 4).

Chapter 2 presents a framework to extract canopy morphometric details using the digital canopy height model (CHM) with the aim of estimating aerodynamic roughness of a region covered by the forest.

Chapter 3 investigates two aerodynamic approaches within the context of estimating roughness parameters of a moderately dense forest using measurements made in the roughness sub-layer.

Chapter 4 examines the spatial and temporal variability of surface albedo of a needleleaf forest stand using atmospherically corrected multi-scale remote sensing data and in-situ solar radiation measurements.

Chapter 5 demonstrate the retrieval process of directional land surface temperature from multiplatform and multi-directional Airborne Hyperspectral Scanner (AHS) data and to validate against the in-situ radiometric and contact temperature measurements collected during the image acquisition.

Chapter 6 presents some concluding remarks of this work and elaborate on future research directions.

2 Estimation of canopy aerodynamic roughness using morphometric methods*

* **This chapter is based on**

Weligepolage, K., Gieske, A.S.M. and Su, Z., 2012. Surface roughness analysis of a conifer forest canopy with airborne and terrestrial laser scanning techniques. *Int. J. Appl. Earth Observation and Geoinformation*, 14, 192-203

Abstract

Two digital Canopy Height Models (CHMs) were generated using the novel Terrestrial Laser Scanning (TLS) technique combined with Airborne Laser Scanning (ALS) data, acquired over a conifer forest. The CHMs were used to extract cross-sections in order to derive surface geometric parameters. Different morphometric models were applied to estimate aerodynamic roughness parameters: the roughness length (z_0) and the displacement height (d_0). The CHMs were also used to derive the area-height relationship of the canopy surface. In order to estimate roughness parameters the observed canopy area-height relationship was modelled by uniform roughness elements of paraboloid or conical shape. The estimated average obstacle density varies between 0.14 and 0.24 for both CHMs. The canopy height distribution is approximately Gaussian, with average heights of about 26 m and 21 m for CHMs generated with data from TLS and ALS respectively. The estimated values of z_0 and d_0 depend very much on the selected model. It was observed that the Raupach models with parameters tuned to resemble the forest structure of the study area can be applied to a wide range of roughness densities. The cumulative area-height modelling produced results which are compatible with other models. This approach is particularly useful because a smaller number of empirical constants is needed in comparison to the former models. Also the results confirm that, to model the upper canopy surface of the conifer forest, both the cone and the paraboloid shapes are fairly appropriate.

2.1 Introduction

Understanding the interaction between the Earth's surface and the lower part of the atmosphere is of paramount importance for many applications in meteorology, hydrology and related fields. It is known that this interaction is determined to an important extent by different exchange processes across the land atmosphere interface (Stull, 1988). One of the important exchange processes associated with the movement of air (wind speed) at the Earth's surface is the exchange of momentum (the product of mass and velocity of a volume of air). In the "free" atmosphere the movement of air is forced by the pressure gradient (difference in atmospheric pressure over a specified distance) resulting from differential solar heating of the surface and internal motion in the atmosphere. Once the moving air mass interacts with the surface of earth, the bottom layer is affected by the frictional forces (surface drag) acting against the motion. The surface drag acting on the bottom layer is transferred to the upper layers of the atmosphere by the internal stresses resulting in turbulence or irregular fluctuations in air motion. This entire process of momentum exchange at the surface of the earth is dominated by the surface roughness characteristic or the aerodynamic roughness.

Land surface models to estimate momentum exchange between the earth's surface and atmosphere often employ wind-profile relations above the surface using the flux-gradient approach or more specifically the relationship between momentum flux density (mass per unit area per unit time) and vertical gradient of wind speed above a surface (Garratt, 1992). However, the accuracy of model results depends much on the parameterization of aerodynamic roughness. Furthermore, the parameterization of aerodynamic roughness is important because it influences not only the momentum transfer, but also the exchange of heat, gases and aerosols across the earth. Parameterization of aerodynamic roughness has been done in hydro-meteorology by introducing two aerodynamic parameters: aerodynamic roughness length (z_0) and zero plane displacement height (d_0). The aerodynamic roughness length (also called momentum roughness length) is a surface length scale defined specifically by the logarithmic wind law for neutral conditions (Brutsaert, 1982). For homogeneous terrain under neutral conditions, the aerodynamic roughness length is the height at which the mean wind speed becomes zero, when extrapolating the logarithmic wind profile through the surface layer. When the wind blows over tall roughness elements like a vegetative canopy, there will be a vertical shift in the logarithmic form of the wind profile due to the surface roughness effects. The zero plane displacement height is the adjustment that has to be made in the measurement height due to this vertical shift from the ground surface. In physical terms, the displacement height is comparable to the level of action of the surface drag on the main roughness elements (Garratt, 1992). Using a

semi-logarithmic plot of mean wind speed versus logarithm of height above the displacement height ($z - d_0$), z_0 may be graphically represented as the zero velocity intercept of the resulting straight line.

In general, roughness parameters are determined from micrometeorological or anemometric methods that use wind measurements by means of meteorological towers or balloon releases. Apart from anemometric methods, morphometric methods are also used. These methods use algorithms that relate roughness parameters to measurable dimensions of surface roughness elements. A review can be found in the literature (Hiyama et al., 1996; Grimmond and Oke, 1999; De Vries et al., 2003). Morphometric methods have distinct advantages over anemometric methods because they do not only avoid cumbersome measurements of meteorological variables but also allow estimation of roughness parameters for all wind directions. However, morphometric methods do have the disadvantage that they are mostly based on empirical relations and laboratory simulations and therefore require validation for natural environments.

Several studies were carried out recently to validate morphometric methods for different natural land surfaces. Hiyama et al. (1996) have evaluated algorithms to estimate regional roughness parameters of a complex landform with patches of various surface types. Grimmond and Oke (1999) have tested several morphometric methods to estimate aerodynamic parameters of urban landscapes. Menenti and Ritchie (1994) have computed the effective aerodynamic roughness in a complex landscape using airborne laser altimeter or LiDAR (Light Detection And Ranging) data to derive surface geometric features. Aerodynamic roughness of a natural forested area was determined with satellite imagery by Jasinski and Crago (1999) using Landsat images. Hasager et al. (2003) have used both Landsat and SPOT (Satellite Pour l'Observation de la Terre) images to estimate the aerodynamic roughness of a flat agricultural area with hedges. In a recent study, De Vries et al. (2003) have evaluated the use of laser altimeter data to extract surface geometric features of an area characterized by coppice dunes with interdunal areas partially covered with grass. More recently, Colin and Faivre (2010) estimated aerodynamic roughness length of landscapes ranging from desert to grassland and irrigated farmland in the northwest of China from very high-resolution LiDAR data.

Although many surface types have been covered previously, few studies have used morphometric methods on surfaces dominated by forest canopies. However forests are complex ecosystems with unique characteristics and presently account for 30 percent of the global land area. Given the significant role of forests on the global energy and water balance, carrying out additional research to investigate aerodynamic roughness of such landscape

is warranted. Particularly more attention should be paid to explore morphometric methods, those that employ state-of-the-art technology to determine aerodynamic roughness of forest surfaces. In order to develop operational methods to estimate forest aerodynamic roughness at regional scale, some improvements to existing methods are required. To be able to deal with large areas, the techniques should be computationally efficient and at the same time should produce results with a reasonable accuracy. In this regard progress can be made by adopting the recent advancement made in laser scanning techniques to map the upper canopy surface with a reasonable accuracy. When such detailed canopy surface maps are available, the method can be further refined by exploring new techniques to derive required surface morphometric parameters.

The aim of this study is to evaluate several morphometric methods to estimate the aerodynamic roughness of a region covered by forest. We adopted two different techniques to estimate surface morphometric variables of a densely vegetated terrain. We assumed that the upper canopy of a dense forest in principle acts as a spatially continuous impenetrable surface. Based on this assumption we digitally mapped the upper canopy surface which in turn was used to derive surface morphometric variables. One of the objectives of the study is to make use of a recently developed high resolution Terrestrial Laser Scanning (TLS) technique to digitally map the upper canopy surface through a multi-scanning approach including a range of different heights. Additionally, we used Airborne Laser Scanning (ALS) data to digitally map the canopy surface of the forest. Although the ALS technique is well established for large-scale canopy surface mapping (Hollaus et al., 2006), only few studies are known where this technique is applied to canopy surface roughness estimation.

2.2 TLS and ALS Data

During the EAGLE 2006 campaign, a detailed 3-D representation of the Speulderbos forest site was obtained using the Leica HDS2500 pulsed laser scanner (Su et al., 2009). In order to obtain the 3D geometry of the canopy, the laser scanner was mounted on the tower site elevator to scan at different heights and at two other ground locations. Figure 2-1-a shows the scan configuration of the TLS procedure. The instrument has a single-point range accuracy of ± 4 mm, angular accuracies of ± 60 μ rad, and a beam spot size of only 6mm from 0-50 m range, including point-to-point spacing as fine as 1.2 mm at 50 m. The data is available in ASCII .xyz format in the Dutch RD (Rijks Driehoeksmeting) system with reference to new Amsterdam zero level (NAP).

The raw data was pre-processed to pixels of 10 by 10 cm and in each cell the maximum height was recorded. The colours in Figure 2-1-b show the resulting heights with respect to mean sea level. The polygon shows the area used for the forest roughness analysis, while the rectangular area indicates the area used for the ALS analysis. Since TLS was performed at multiple levels by mounting the scanner to the elevator (Figure 2-1-a), reflected points below the forest canopy level (trunk-space) were also recorded as horizontal slices. By plotting the horizontally sliced points obtained from the trunk-space on the x-y plane, it was possible to locate the positions of the individual tree trunks. These have been indicated as small black dots in Figure 2-1-b.

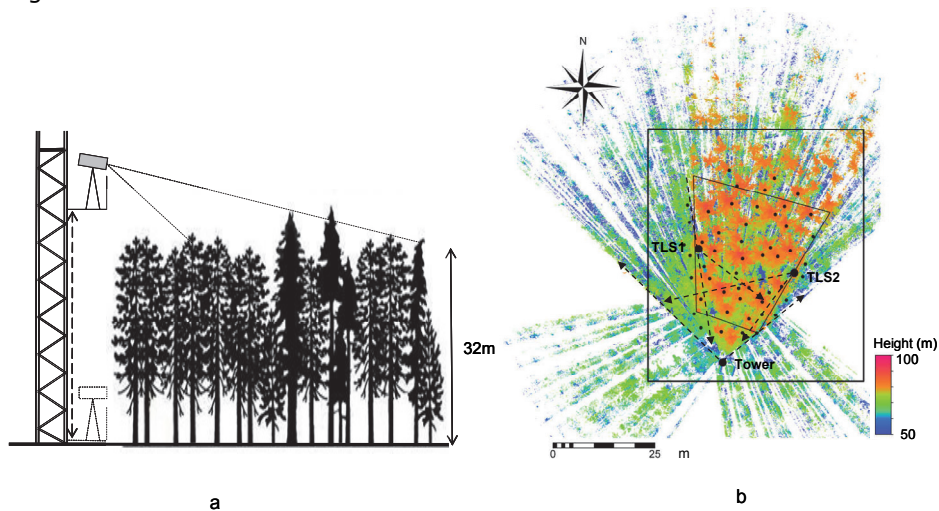


Figure 2-1: Terrestrial Laser Scanning (TLS) at Speulderbos. Panel (a) shows the scaffolding Tower and the vertical movement of the scanner. Panel (b) shows the plan view from three directions (Tower and two ground locations TLS1, TLS2).

AHN provides high density ALS data which describe the elevations of The Netherlands and the dataset is available through the product AHN-1. The raw data set used for this study has been acquired in year 2000 and contains the reflection of the laser beam on the vegetation, any manmade object present on the terrain or the ground itself. The terrain elevations have been obtained subsequently through a filtering procedure (Van Heerd et al., 2000). Both the raw data set (tree-top elevations) and the corresponding filtered dataset (terrain elevations) are available for the study area in the ASCII .xyz format with reference to the Dutch RD coordinate system. The terrain elevation dataset can be subsequently used to generate a digital terrain model (DTM) of the area.

2.3 Some basic concepts & terminology

In principle rough surfaces can be categorized as either bluff-rough or permeable rough according to the response of the roughness elements to wind flow (Brutsaert, 1982). A surface is called a bluff-rough surface when the roughness elements act as impermeable obstacles. A ploughed agricultural field, rigid vegetation like a cabbage plantation, an urban area closely packed with buildings are few examples for bluff-rough surfaces. However most of the natural surfaces consist of roughness elements which are permeable to wind, hence do not behave as bluff-rough surfaces.

For surfaces with large scale permeable roughness elements, the total stress (τ_t) exerted by turbulent boundary-layer flow is shared between the roughness elements and the underlying substrate surface and can be expressed as:

$$\tau_t = \tau_f + \tau_s \quad (2-1)$$

where τ_f is the form drag on the roughness elements per unit horizontal area and τ_s is the shear stress or the frictional force per unit area acting on the underlying substrate surface.

It is also important to differentiate the definitions used in forestry to describe the stand height of a forest canopy. The average tree-top height within a forest stand is defined as the arithmetic mean of individual tree heights usually measured in the field using equipments such as hypsometers, electronic total stations etc. Another definition adopted is the Lorey's mean height where the individual tree heights are weighted in proportion to their basal area. The canopy height which is more relevant to remote sensing studies is defined as the vertical extent of the vegetation canopy from the ground surface to the top of the canopy over a regular grid. Usually the canopy height is more in agreement with the Lorey's mean height.

2.3.1 Models to estimate roughness parameters

For bluff-rough surfaces, Kutzbach (1961) proposed the following empirical relationship to estimate d_0 .

$$\frac{d_0}{h} = c_1 \lambda^{c_2} \quad (2-2)$$

λ is the obstacle density defined as the ratio sn/A where s is the cross sectional area of the obstacle measured in a vertical plane perpendicular to the wind direction, and n number of obstacles on a horizontal area A . The

constants c_1 and c_2 were determined by Kutzbach (1961) as $c_1 = 1.09$ and $c_2 = 0.29$ for a simulated bluff-rough surface.

Grant and Mason (1990) incorporated the concept of total stress and proposed the following equation to calculate the effective roughness of complex terrain.

$$z_0 = \frac{h}{2} \exp \left[\frac{-k}{\left(0.5c_{d0}\lambda + k^2 / \ln^2 \left(\frac{h}{2z_{01}} \right) \right)^{0.5}} \right] \quad (2-3)$$

where k is the von Karman's constant taken as 0.41, z_{01} is the local roughness length representing the shear stress component of the substrate surface and c_{d0} is the drag coefficient at $z=h/2$. For bluff bodies the value of c_{d0} varies between 0.2 and 0.8 depending on the shape of the obstacles (Mason, 1985). A value of $c_{d0} = 0.3$ was used by Grant and Mason (1990) to calculate the effective roughness length of an area of sinusoidal orography.

Using dimensional analysis and two physical hypotheses, Raupach (1992) developed a drag partition model and proposed a relationship to estimate momentum roughness length. Raupach's model not only considers the shelter effect of roughness elements on the substrate surface, but also that on the surrounding elements and proposed the following equation;

$$\frac{z_0}{h} = \left(\frac{h-d_0}{h} \right) \exp(\psi_h) \exp(-k\gamma) \quad (2-4)$$

where ψ_h is taken here as a profile correction constant equal to 0.193 (Raupach, 1995).

The parameter γ is the ratio (u_h/u_*) which is given by the following equation.

$$\gamma = (C_S + C_R\lambda)^{-1/2} \exp\left(\frac{c\lambda\gamma}{2}\right) \quad (2-5)$$

in which u_h is the wind speed at $z=h$, u_* is the friction velocity which is defined as the square root of the kinematic momentum flux $(\tau/\rho)^{1/2}$ where τ is the Reynolds' stress and ρ is the air density, C_S (taken as 0.003) is the

drag coefficient of the substrate surface, C_R (given as 0.3) is the drag coefficient for an isolated surface-mounted roughness element, and $c \approx 0.37$ is an empirical coefficient. Since (2-5) is an implicit equation specifying γ as a function of λ , in general a solution is obtained numerically. The method of fixed point iteration (Burden and Faires, 2010) has been used here to estimate γ using (2-5).

Raupach (1992) also proposed the following model to estimate the displacement height.

$$\frac{d_0}{h} = \frac{\beta\lambda}{1 + \beta\lambda} \left[1 - c_d \left(\frac{b}{h\lambda} \right)^{1/2} \frac{1}{\gamma} \right] \quad (2-6)$$

Where $\beta = C_R/C_S$, b is the width of the frontal part of a roughness element (here taken equal to 5.5 m), and c_d is a constant found to be around 0.6.

Raupach (1994) derived a simple analytical expression for roughness length of vegetated surfaces. Rather than using the full iterative solution of (5) for γ , he proposed the following approximation equation for all $\lambda < \lambda_{\max}$ which is about 0.3.

$$\frac{u_*}{u_h} = \min \left[(C_s + C_R \lambda)^{1/2}, (u_*/u_h)_{\max} \right] \quad (2-7)$$

Where $(u_*/u_h)_{\max}$ is a constant value of about 0.3, when $\lambda > \lambda_{\max}$ (which is also about 0.3).

The simplified approach of Raupach (1994) is given as

$$1 - \frac{d_0}{h} = \frac{1 - \exp\left(-\sqrt{2c_{d1}\lambda}\right)}{\sqrt{2c_{d1}\lambda}} \quad (2-8)$$

where c_{d1} is a free parameter found to be around 7.5 by fitting (2-8) to observed values.

2.3.2 Generation of Canopy Height Models (CHM)

The first step towards the generation of CHM is the generation of the DTM of the area. In order to generate the DTM we used a geo-statistical method (ordinary kriging) by which the irregularly spaced ALS terrain data points with x, y, z coordinates were interpolated. First the experimental semi-variogram was calculated using the ALS terrain elevation points and fitted

with a power semi-variogram model as shown in Figure 2-2. Using the power semi-variogram model, point data was interpolated through ordinary kriging. The resulting DTM, resampled to a resolution of 10x10cm, is also shown in **Error! Reference source not found.** The DTM was subsequently used for generating canopy height models with both the ALS and TLS canopy elevation data sets as described in the following paragraphs.

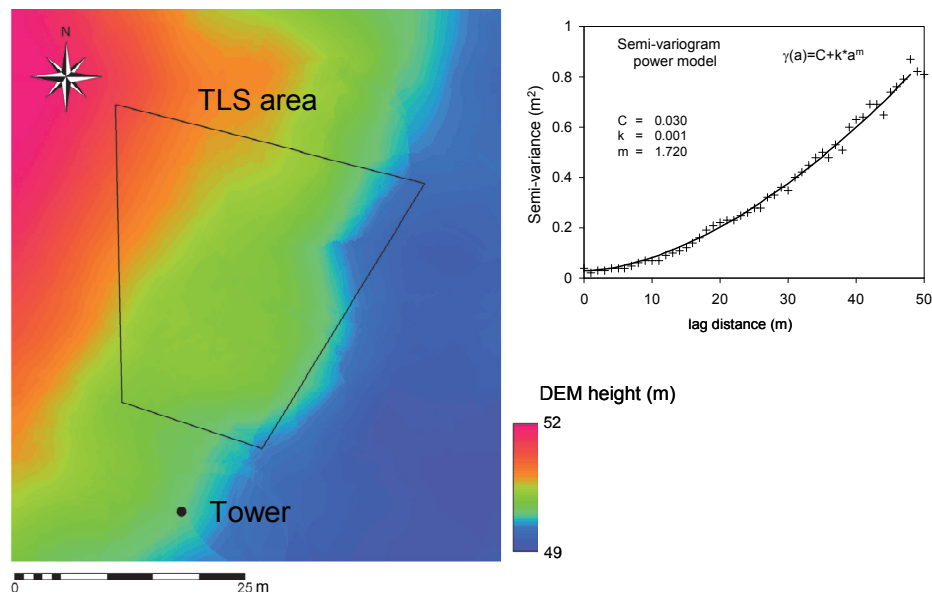


Figure 2-2: Digital Elevation Model created by interpolating the ALS terrain elevation data and the power semi-variogram model used for ordinary kriging.

Before further processing we made a comparison of canopy heights derived using the TLS and ALS raw data sets. This comparison made it possible to setup threshold values for minimum canopy heights and thereby to eliminate possible erroneous (low occurring) canopy height values present in both data sets. First using the pre-processed TLS raw data set with elevations for every 10 x 10 cm pixel, a polygonal area was selected for further analysis (see Figure 2-1). Then the ALS data set was used to select the canopy elevation points contained within that polygonal area. These points were subsequently used to extract the corresponding height values from the TLS raw data set. This was done using a GIS software by overlaying the point data from ALS on the raster image of TLS data. For each ALS point the corresponding elevation was obtained from the TLS image using few GIS operations. The corresponding terrain elevations for these data points were also obtained by repeating the same exercise using the previously generated DTM. The canopy heights for both the ALS and TLS data points were calculated by subtracting the terrain elevation from the respective canopy elevations.

The resulted canopy height data set of 226 points is shown in the scatter diagram of Figure 2-3-a, and as histograms in Figure 2-3-b. The Figure 2-3-b shows the apparent canopy height difference between the TLS and ALS points. Moreover panels a and b show the occurrence of low canopy values for both TLS and ALS data. Figure 2-3-a was subdivided in 4 quadrants by a horizontal and a vertical line to illustrate the situation. The upper left quadrant shows the situation where TLS records are high and ALS records are low. Apparently, the ALS laser beam has penetrated through gaps in the forest canopy. This mainly depends on the laser footprint size and the canopy closure. The lower right quadrant shows high ALS and low TLS values. The differences may be due to errors in coordinates, or due to obstacle shadow effects. In view of the fact that the study area is characterized by rather dense canopies, it was decided to compensate for these discrepancies by only allowing TLS values greater than 15 m and ALS values greater than 10m, i.e. restricting the data to the upper right quadrant of Figure 2-3-a.

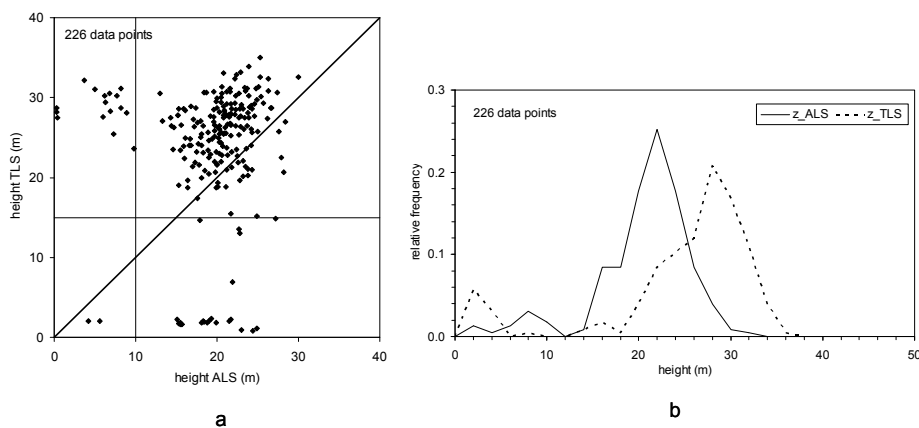


Figure 2-3: Panel (a) shows correlation between TLS and ALS canopy heights for 226 data points and Panel (b) shows histograms of TLS and ALS canopy heights (bin size 2 m).

Figure 2-4 shows the histogram for the entire TLS raw data set, illustrating the bimodal nature of the data with distinct peaks at about 2 m and 28 m. The threshold value of 15 m will effectively remove the lower part of the histogram.

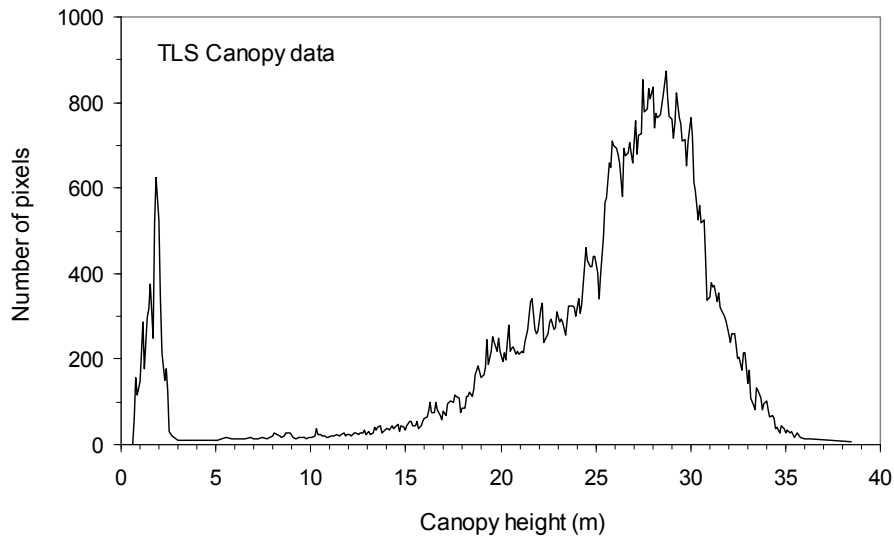


Figure 2-4: Histogram of entire TLS canopy data set (bin size 1 m) showing bimodal character.

Once the threshold values were identified, two data sets were further processed in the following manner. For the entire set of ALS data points the canopy heights were computed by subtracting terrain elevations from the canopy elevations. From the computed canopy height data set, all the points with canopy heights below 10 m were eliminated. The resulted ALS canopy height data set was then interpolated on a grid of 10 cm by 10 cm using an exponential semi-variogram model (Figure 2-5-a) with nugget 7 m², sill 10.3 m² and range 3.5 m. Next, the ALS data was also interpolated with nugget zero (Figure 2-5-b). The resulted canopy height models (ALS-CHM) are also shown in Figure 2-5 in panels a and b.

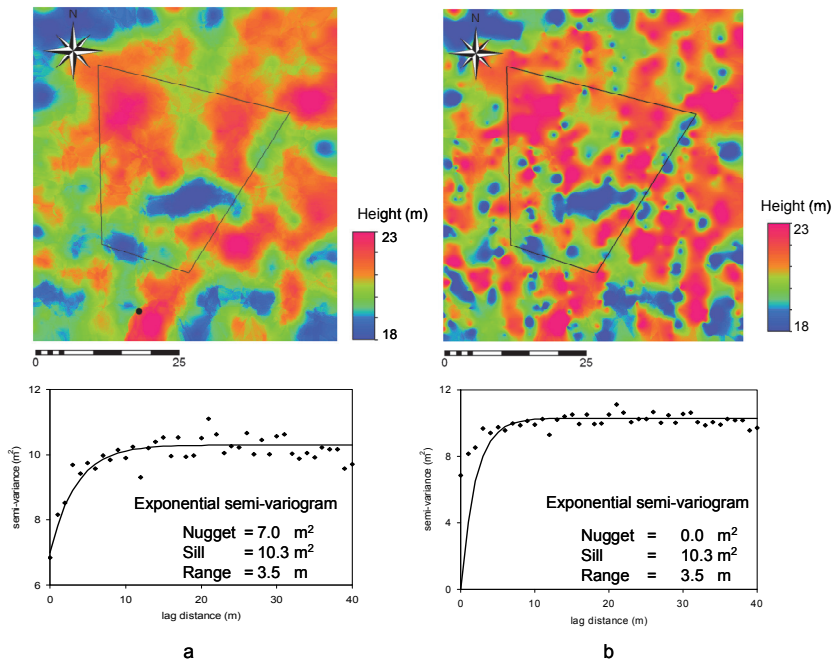


Figure 2-5: ALS Canopy Height Models interpolated by ordinary kriging with the exponential semi-variogram models with nugget 7 (panel a) and nugget 0 (panel b).

The processing of the TLS data set involved more steps. First, the raw canopy height model was obtained by subtracting the DTM values from the canopy surface elevations. Next, the pixels with raw canopy heights less than 15m were removed. These gaps were then filled by inverse distance weighing (IDW) (Figure 2-6-a). Finally, a median 5x5 filter was applied to smooth the image as shown in Figure 2-6-b.

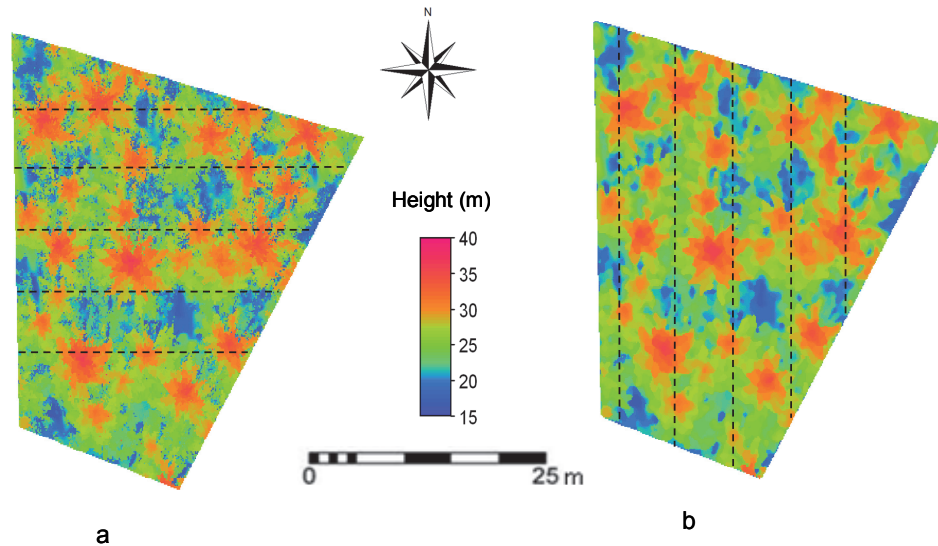


Figure 2-6: TLS Canopy Height Models. (panel-a) Gaps filled by IDW and (panel-b) Running a Median filter (5X5 pixels). The dashed lines indicate the distribution of transects for two principal directions.

2.3.3 Estimation of roughness parameters using CHMs

The CHM provides gridded three dimensional (3-D) information of the upper canopy surface. We adopted two different approaches to derive surface geometric parameters. In the first approach (described in this section), several cross-sections extracted from the CHM were used to derive obstacle density and mean canopy height. These surface features were then used to determine the roughness parameters with the algorithms described in section 2.3.1. In the second approach (see section 2.4.1), the observed area-height relationship of the CHM was modelled with basic geometric shapes.

2.3.4 Estimation of obstacle parameters (λ) and (h)

In the analysis we applied the algorithms of Grant and Mason (1990), Raupach (1992), Raupach (1994) and Kutzbach (1961) to estimate roughness length and displacement height. We calculated obstacle density λ using a method previously adopted by Hiyama et al. (1996) and de Vries et al. (2003). The method basically assumes that the surface is isotropic and the areal roughness density λ can be defined over a cross-sectional line as follows:

$$\lambda = \frac{\sum_{i=1}^n \Delta y_i}{\sum_{i=1}^n \Delta x_i} \quad \text{for } \Delta y_i > 0 \quad (2-9)$$

where Δy_i is the positive height difference for each Δx_i in the cross section. In order to estimate surface features we extracted several cross-sections (height at 10cm intervals) along North-South direction and East-West direction from the generated CHMs. The length of North-South TLS profiles are 30m on average whereas the length of East-West profiles varies between 20m and 25m. The distribution of selected profiles is shown in Figure 2-6. The ALS profiles were taken along the same lines as shown in Figure 2-6 (a) and (b) but extended to the full length and width of the ALS canopy area (Figure 2-5). The average profile height was estimated from the height values at 10cm horizontal resolution along the profile.

In order to calculate obstacle density we adopted the procedure described by de Vries et al. (2003). First, the height values were smoothed by block averaging using intervals of 10 measurements. Subsequently, a moving average with a variable number of measurements was applied to the block averages to reduce random and system noise present in the laser measurements. Obstacle density was computed by integrating positive height changes divided by the distance using equation (2-9). To determine the correct moving average, λ versus the number of measurements in a moving average was plotted in Figure 2-7. The figure shows three curves: (a) the curve derived from the TLS-CHM shown in Figure 2-6-a. The curve derived from Figure 2-6-b is not shown because it is very much the same as the one derived from Figure 2-6-a. (b) the curve derived from Figure 2-5-b (nugget zero) and (c) the curve from Figure 2-5-a (nugget 7). The curves decline rapidly at low numbers and less rapidly at higher numbers and converge at around a number of 7 measurements in an average, as was reported also by De Vries et al. (2003). The procedure was repeated for all 10 profiles (5 N-S and 5 E-W) to obtain a spatial average value for the areal roughness density of the represented canopy area. This resulted in 10 different sets of values for λ and h for the profiles extracted from each CHM. The statistical summary of the derived surface parameters are listed in Table 2-1 and Table 2-2 and the range in values is also indicated in Figure 2-7 by dashed lines.

Table 2-3 summarizes the average canopy heights and obstacle densities derived for the three curves of Figure 2-7. It is thought that the spatial interpolation of the ALS data with nugget 0 (Figure 2-5-b) reflects the real canopy surface better than the interpolation with nugget 7 (Figure 2-5-a). Interpolating with a high nugget value will smooth the canopy excessively.

For this reason the roughness values are calculated based on curves (a) and (b) shown in Figure 2-7.

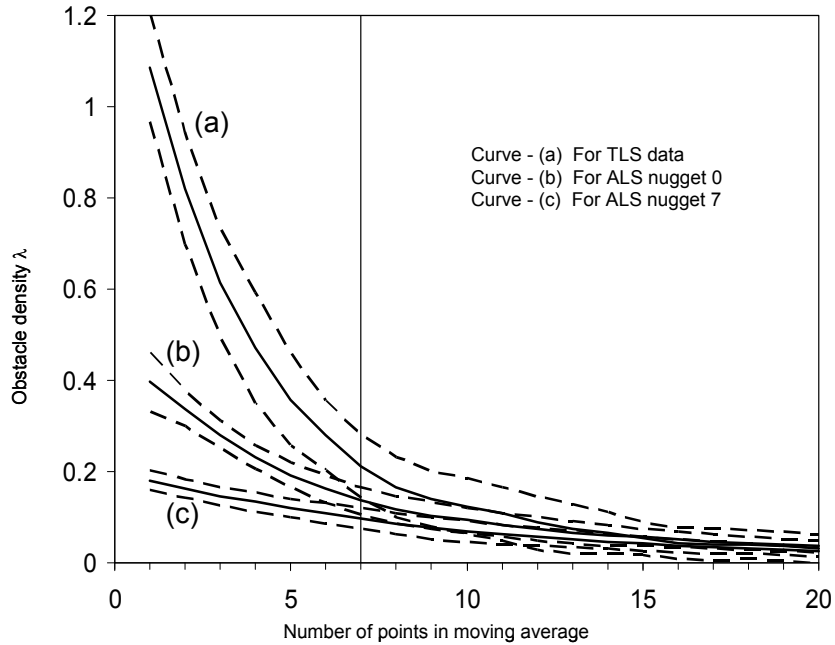


Figure 2-7: Plot of the average obstacle density versus moving average number. Solid lines indicate the mean λ values for 10 profiles. Dashed lines show the range of λ for each curve.

Table 2-1: Statistical Summary of TLS-CHM derived canopy surface features for different directions.

Direction	Parameter	TLS_IDW		TLS_M5		
		Average	Std. de.	Parameter	Average	Std. de.
N-S	λ	0.242	0.043	λ	0.242	0.043
	h (m)	25.890	0.700	h (m)	26.020	0.660
E-W	λ	0.179	0.067	λ	0.174	0.065
	h (m)	25.720	1.490	h (m)	26.000	1.620

Table 2-2: Statistical Summary of ALS-CHM derived canopy surface features for different directions

Direction	Parameter	Nugget 7		Nugget 0		
		Average	Std. de.	Parameter	Average	Std. de.
N-S	λ	0.098	0.014	λ	0.136	0.020
	h (m)	20.860	0.440	h (m)	20.890	0.620
E-W	λ	0.096	0.028	λ	0.136	0.036
	h (m)	21.100	0.410	h (m)	21.280	0.420

The individual profile details revealed that the roughness density and the average height estimates vary slightly between the extracted profiles. The spatial average values of Table 2-3 (i.e. TLS data and ALS data with nugget zero) were used for the roughness parameter calculations as described in the following section. The difference in average canopy height of the two CHMs shows that the canopy height has increased by about 5m in the period from 2000 to 2006.

Table 2-3: Summary of results for spatially average canopy height and obstacle density.

Method	h_{avg} (m)	λ (at n=7)
TLS	25.81	0.2106
ALS nugget 7	20.98	0.0969
ALS nugget 0	21.09	0.1361

2.4 Determination of aerodynamic parameters

The aerodynamic roughness parameters estimated using the spatial averages of λ and h for each CHM are listed against the adopted method in Table 2-4. The computed ratios z_0/h and d_0/h are also listed in the table. The results show that the selected methods produce widely differing estimates. The figures of Table 4 were compared with published mean values of z_0/h and d_0/h obtained from different studies. Since the published z_0 and d_0 values fall into a wide range of canopy heights, it is sensible to compare the normalized height values. The published mean values of z_0/h and d_0/h are respectively 0.076 and 0.78 (Garratt, 1992) and therefore, the results of Grant and Mason (1990) model are in good agreement with these values for the TLS data. Similarly, Kutzbach (1961) and Raupach (1992) have produced d_0/h estimates fairly consistent with the corresponding mean value. However, the z_0/h and d_0/h values predicted by the Raupach (1994) model are further away from the published mean values of Garratt (1992).

Table 2-4: Estimated roughness parameters using original model parameters

Model	Average from TLS		Average from ALS	
	z_0 (m)	z_0/h	z_0 (m)	z_0/h
Grant & Mason (1990)	1.44	0.056	0.74	0.060
Raupach (1992)	0.75	0.029	0.55	0.030
Raupach (1994)	2.97	0.115	1.92	0.120
<hr/>				
	d_0 (m)	d_0/h	d_0 (m)	d_0/h
Kutzbach(1961)	17.91	0.694	12.89	0.611
Raupach (1992)	21.60	0.837	16.81	0.797
Raupach (1994)	13.74	0.532	9.87	0.468

In the present analysis we assumed parameter values $z_{01} = 0.01\text{m}$ and $c_{d0} = 0.3$ in the Grant and Mason (1990) model to estimate z_0 of the canopy surface. It is reported that previous studies have used the model with slightly different values; $c_{d0} = 0.4$ (Menenti and Ritchie, 1994) and c_{d0} around 0.75 - 1.0 (Hiyama et al., 1996) to calculate z_0 in different landscapes. The estimated z_0 value is rather sensitive to the choice of c_{d0} . For instance, changing c_{d0} from 0.3 to 0.5 would increase z_0 from 1.6m to 2.6m. Nevertheless, a value between 0.3 and 0.4 for c_{d0} yields z_0 estimates that are comparable with the published values.

Both the Raupach (1992) and Raupach (1994) models contain a number of parameters viz. C_S , C_{Rr} , c , c_w , c_{dr} and c_{d1} introduced during the formulation. The recommended values for C_{Rr} and c_w have been deduced from theory while others were determined empirically. Since the parameters have been originally calibrated using relatively closed canopies ($\lambda > 0.5$) their applicability to sparser canopies is doubtful. Verhoef et al. (1997) have evaluated Raupach's models comparing the model predictions against published values of aerodynamic roughness parameters determined from wind profile measurements. These authors have adopted a value of $C_S = 0.01$ from literature considering the type of vegetation (shrubs). They determined values for C_{Rr} , c and c_{d1} which were quite different from the original values given by Raupach (1992 and 1994). They have further emphasized that with the new optimized parameters Raupach's models perform better for a wide range of canopies varying in density from closed to sparse. The values reported by Verhoef et al. (1997) for Raupach's models are listed in Table 2-5.

Table 2-5: Comparison of model parameters in Raupach (1992) and Raupach (1994) models

Parameter	Original values	(Verhoef et al., 1997)		Proposed values	
		Raupach (1992)	(for z_0)		(for d_0)
C_R	0.300		0.42	0.47	0.42
C_S	0.003		0.01	0.01	0.01
c	0.370		-1.30	-3.80	0.37
c_d	0.600		0.20	0.20	0.60
Raupach (1994)					
C_R	0.300		0.35	0.35	0.35
C_S	0.003		0.01	0.01	0.01
c_{d1}	15.000		20.60	21.00	45.00

It was observed that both the Raupach (1992) and Raupach (1994) models perform better with the modified parameters of Verhoef et al. (1997). However the use of different values for parameters C_R (0.42 and 0.47) and c (-1.3 and -3.8) to estimate z_0 and d_0 respectively in the Raupach (1992) model (see Table 2-5) by Verhoef et al. (1997) seems to be unrealistic. In order to avoid that, we proposed a new set of parameters. We observed that much better results can then be obtained. It was also observed that parameter c_{d1} can be changed to obtain results much closer to the published mean values reported for coniferous forests (Garratt, 1992). The final proposed model parameters are listed in Table 2-5 and the estimated roughness parameters are listed in Table 2-6.

Table 2-6: Estimated roughness parameters using proposed model parameters

Model	Average from TLS		Average from ALS	
	z_0 (m)	z_0/h	z_0 (m)	z_0/h
Raupach (1992)	1.678	0.065	1.341	0.064
Raupach (1994)	1.721	0.067	1.354	0.064

	d_0 (m)	d_0/h	d_0 (m)	d_0/h
Raupach (1992)	19.56	0.758	14.64	0.694
Raupach (1994)	19.96	0.773	14.93	0.708

We carried out a sensitivity analysis to find out the impact of varying the average λ on our resulted aerodynamic parameters using adopted methods. The variation of d_0 and z_0 predicted by different models with respect to λ is illustrated in Figure 2-8. The results indicate that the estimated z_0 using the Grant and Mason (1990) model is much more sensitive to λ compared to the other two models.

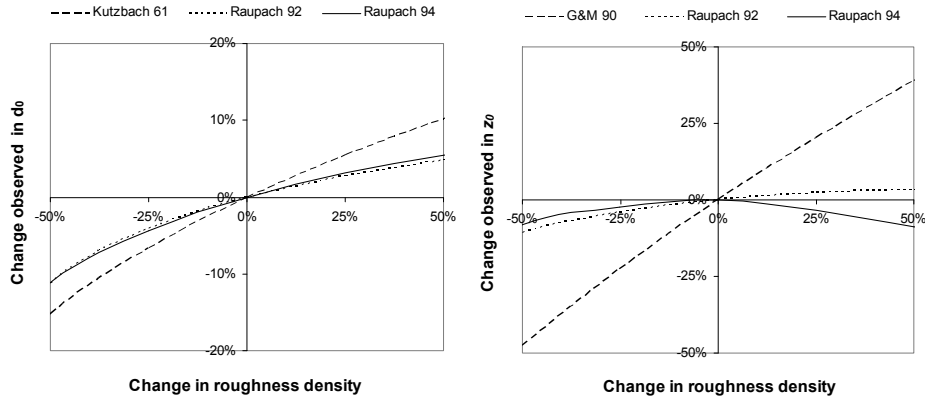


Figure 2-8: Sensitivity of d_0 and z_0 estimated from different models with respect to λ .

2.4.1 Representation of roughness elements using basic geometric shapes

Leonard and Federer (1972) estimated roughness parameters of a red pine plantation using a contour map of the upper canopy surface. They derived the surface parameters based on the assumption that the canopy can be represented by an array of uniform obstacles such as cones or paraboloids (of height h^*) having tangent bases in either square or hexagonal close packing. The fractional surface area (α) for a three dimensional object with a given packing geometry can be defined as the vertically projected surface area above a given height (z) per unit circumscribed area of the regular polygon. Accordingly α for a surface modelled by the cone is given as:

$$\alpha = \frac{\pi}{4} \left(1 - (z - d_0)/h^*\right)^2 \quad (\text{for square packing}) \quad (2-10)$$

$$\alpha = \frac{\pi}{2\sqrt{3}} \left(1 - (z - d_0)/h^*\right)^2 \quad (\text{for hexagonal packing}) \quad (2-11)$$

and for the paraboloid is given as

$$\alpha = \frac{\pi}{4} \left(1 - (z - d_0)/h^*\right) \quad (\text{for square packing}) \quad (2-12)$$

$$\alpha = \frac{\pi}{2\sqrt{3}} \left(1 - (z - d_0)/h^*\right) \quad (\text{for hexagonal packing}) \quad (2-13)$$

The above set of equations can be derived using the algebraic relations of the surface geometry of a cone or a paraboloid of height h^* in connection with the respective close packing geometry at the base, as described by Leonard and Federer (1972). Height h^* corresponds to the height of the cone or paraboloid above the displacement height d_0 . Height z is measured above the surface level. It should be noted that the maximum α for square packing is $\pi/4$ (Eqs. 2-10 and 2-12) whereas the maximum α for hexagonal packing is $\pi/(2\sqrt{3})$ (Eqs 2-11 and 2-13).

2.4.2 Determination of d_0 and h^* using cumulative area-height relationship

Using the ALS and TLS canopy height models generated previously, we obtained the cumulative area-height relationships (graph of cumulative α versus height) of the forest canopy (see Figure 2-9). With this relationship it is possible to derive values for d_0 and h^* by means of Eqs. 2-10 to 2-13. One of the options is by fitting the equations at two arbitrary points of the area-height relationship and solving for d_0 and h^* . Leonard and Federer (1972) used two fixed α values at 0.15 and 0.85 (15 and 85%) to obtain two canopy intercepts, which allowed them to solve the equations (2-10 to 2-13) for h^* and d_0 . (see Table 2-7 and Table 2-8). Alternatively solutions for d_0 can be found by considering the fact that α reaches its maximum value ($\alpha = \pi/4$ for square packing and $\alpha = \pi/(2\sqrt{3})$ for hexagonal packing) when z is equal to d_0 . In this case the value of d_0 depends only on the packing geometry and the assumed shape is irrelevant. The second point can be taken at $\alpha = 0.15$ as in the case of Leonard and Federer (1972) to solve for h^* . The resulted values for h^* and d_0 for two options are summarized in Table 2-7 and Table 2-8 and some solutions are illustrated in Figure 2-9.

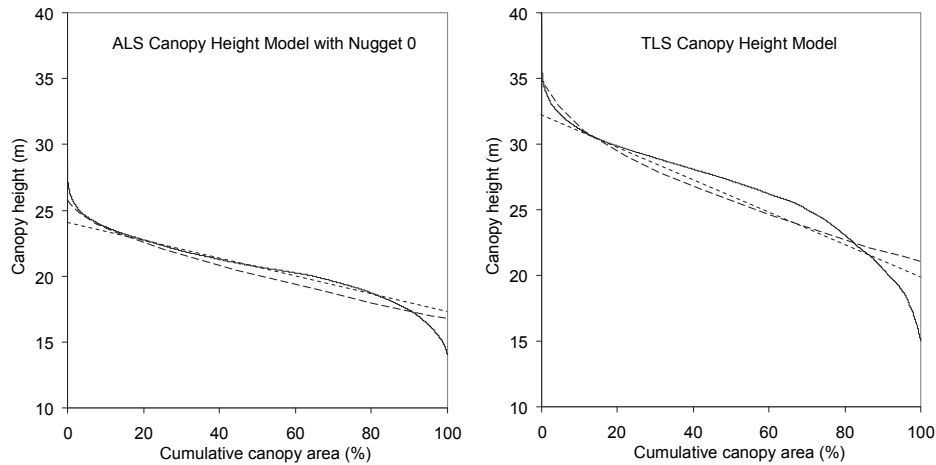


Figure 2-9: Area height relationship of the CHM showing the fitted geometrical models. The solid lines show the values obtained from the canopy height models. Short dashed lines indicate the paraboloid model. Long dashed lines indicate the conical model.

In accordance with Thom (1971) and De Bruin and Moor (1985), z_0 can be assumed proportional to h^*

$$z_0 = \mu h^* \quad (2-14)$$

where μ is an empirical coefficient around 0.2-0.3.

The observed canopy height distribution of the area represented by CHM is near normal as shown by the S-shaped curves of Figure 2-9. It is evident that neither cone nor paraboloid model perfectly matches the cumulative area height relationship of the two CHMs. Although the cone seems to be fitting the upper 10% of the canopy surface (canopy heights above 32 m for TLS and same above 24 m for ALS), overall fit is slightly better with the paraboloid shape. This is further illustrated in Figure 2-10 by comparing the modelled cone and the paraboloid shapes against TLS point data over a typical crown section. It is also evident from the comparison that the assumed shapes and packing geometry reasonably fit the TLS data.

Table 2-7: Results obtained with different geometrical models after fitting the TLS-CHM

TLS ($\mu=0.2$)				
Shape	Packing Geometry	h^* (m)	d_0 (m)	z_0 (m)
Cone	Square	13.752	22.345	2.750
Cone	Hexagonal	17.058	19.967	3.412
Cone	Hexagonal (15-85)	15.888	20.661	3.178
Paraboloid	Square	9.570	22.345	1.914
Paraboloid	Hexagonal	12.126	19.967	2.425
Paraboloid	Hexagonal (15-85)	11.557	20.443	2.311

Table 2-8: Results obtained with different geometrical models after fitting the ALS-CHM

ALS ($\mu=0.2$)				
Shape	Packing Geometry	h^* (m)	d_0 (m)	z_0 (m)
Cone	Square	5.772	19.431	1.154
Cone	Hexagonal	7.525	18.216	1.505
Cone	Hexagonal (15-85)	6.747	18.677	1.349
Paraboloid	Square	4.017	19.431	0.803
Paraboloid	Hexagonal	5.349	18.216	1.070
Paraboloid	Hexagonal (15-85)	4.908	18.584	0.982

The results obtained using the method described in paragraph 2.4.2 are listed in Table 2-7 and Table 2-8. Although the estimated values of d_0 are fairly consistent with the assumed shape and the packing geometry, the estimated h^* and thus the z_0 estimates differ depending on the assumed shape and packing. Obviously the value of z_0 depends on the choice of the μ value too. De Bruin and Moor (1985) have found $\mu = 0.22$ for a pine forest using anemometric methods. We observed that (with a value for $\mu = 0.2$) the estimated d_0 and z_0 values for the paraboloid shapes are in good agreement with the values of Table 6 for the TLS image, while agreement for the ALS image is better for the model with the conical shapes. However, the agreement between the results of two methods outlined in paragraphs 2.4

and 2.4.2 is fair, considering the large variation in z_0 values between different types of land surface and vegetation cover.

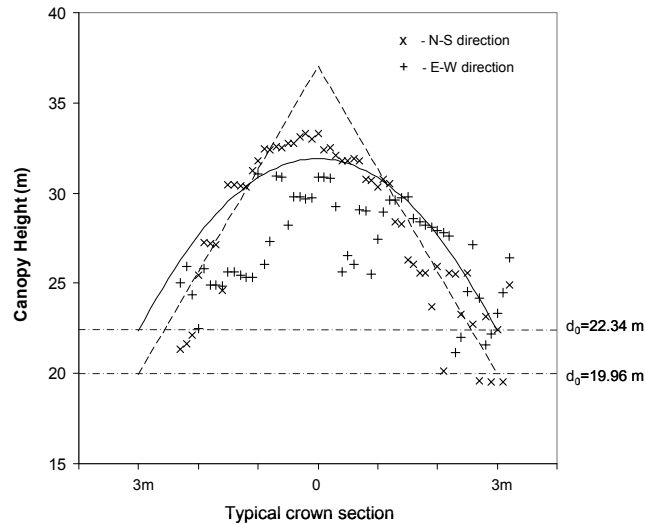


Figure 2-10: A typical crown section fitted with cone in hexagonal packing and paraboloid in square packing shapes. TLS point data for two principal directions are compared.

2.5 Conclusions

In this chapter we used high resolution laser scans to construct digital canopy height models of a coniferous forest. We explored the use of these height models to estimate aerodynamic roughness parameters of the forest stand. We tested several morphometric models, based on the theories of Kutzbach (1961), Grant and Mason (1990), Raupach (1992) and Raupach (1994). The models basically used the obstacle density as the independent variable to estimate roughness parameters.

The estimated average obstacle density was in the range of 0.14 to 0.24 in both canopy height models. The estimated average λ values depend very much on the selected moving average filter size. Nevertheless the highest estimated λ values (without applying a moving average) are within the range of values reported for similar land surfaces. For different canopy types, Verhoef et al. (1997) have reported a range of λ from 0.04 (Vineyard) to 0.6 (Savannah) citing several references. Our estimated λ values suggest that we are in the category of relatively sparse canopies ($\lambda < 0.5$). It should be noted that the results indicate that roughness density of the forest has increased in the period of six years between the ALS and TLS measurements.

The results show that z_0 and d_0 of a tall vegetation canopy can be satisfactorily determined through the laser derived surface features. The

results also show that the Raupach models perform better with the optimized parameters recommended by Verhoef et al. (1997). Although the models of Grant and Mason (1990) and Kutzbach (1961) produced reasonable estimates of z_0 and d_0 in this study, their applicability to higher roughness densities is doubtful. The Raupach models with parameters tuned to resemble the forest structure of the study area can be applied to a wide range of roughness densities.

The cumulative area-height modelling produced results which are compatible with other models. This approach is particularly useful because a smaller number of empirical constants is needed in comparison to the former models. However, knowledge of μ is important as it significantly affects the z_0 estimate. Our results have shown that, to model the upper canopy surface of the coniferous forest, both the cone and the paraboloid shapes are fairly appropriate. However with present results we are unable to clearly establish the fact that one model is favoured over the other to employ with either TLS or ALS method. Usually a scanner that is more likely to miss the tree apices (this is common with TLS due to occlusion and wind effect) may favour the use of paraboloid model. Also with ALS method, tree tops are likely to be missed as a consequence of the under-sampling and this may particularly affect coniferous trees such as fir or spruce. Therefore when extrapolating these methods to large areas with different canopy geometries one has to accommodate these limitations. Further our assumption of having an impenetrable upper canopy surface is arbitrary and unrealistic since most of the forest canopies naturally act as permeable surfaces. Many studies in the field of fluid mechanics have indicated that the velocity profiles over permeable surfaces are more turbulent than those over impermeable rough surfaces. This has been attributed to the additional energy dissipation caused by exchange of momentum across the permeable surface. In consequence of the above assumption it is more likely that we have underestimated the forest aerodynamic roughness. As a final remark we would mention that the results of the morphometric models described in this chapter can be compared with roughness parameters obtained with aerodynamic methods using on-site turbulence or wind profile measurements. This will be discussed in the next chapter.

3 Effect of Sub-layer corrections on the roughness parameterization of a Douglas fir forest*

* **This chapter is based on**

Weligepolage, K., Gieske, A.S.M., van der Tol, C., Timmermans, J. and Su, Z., 2012. Effect of sub-layer corrections on the roughness parameterization of a Douglas fir forest. *Agricultural and Forest Meteorology*, 162-163(2012), 115-126

Abstract

This chapter investigates two aerodynamic methods to estimate the momentum roughness length and displacement height (z_0 and d_0 respectively) of a 32 m-tall Douglas fir forest using simultaneous micrometeorological and flux measurements. When the flux-gradient method was used to objectively determine z_0 and d_0 , corrections for roughness sub-layer effects proved to be important. A new iterative method is employed to solve the set of equations when the corrections were made. The estimated average values of z_0 and d_0 with corrections vary from 1.2 m to 1.4 m and from 26.2 m to 28.4 m respectively depending on the correction method applied. In the absence of experimentally determined roughness sub-layer height, the corrections of Harman and Finnigan (2007) yielded the best overall estimates of aerodynamic parameters. Comparison with results of over 25 other studies has shown that the results obtained here fit the general trend rather well. The relationship between displacement height d_0 and mean tree height h_c is well described by the quadratic equation: $d_0=0.0087h_c^2+0.566h_c$. Similarly the quadratic equation: $h_a=0.006h_c^2+0.865h_c$ appears to be the best to illustrate the relation between aerodynamic canopy height h_a and h_c . These simple relationships can be easily incorporated to large scale land surface models, provided that spatially distributed canopy height information is available. Furthermore the alternative flux-variance technique cannot be objectively used to estimate z_0 and d_0 as no explicit method exists to select the exact value for coefficient C_1 , which mainly causes the variance method to compute systematically higher or lower sensible heat flux.

3.1 Introduction

Forests play an important feedback role in climate processes (see e.g. Teuling et al., 2010). In addition to the forests' contribution to carbon exchange and surface albedo alteration they efficiently couple the earth's surface and the atmosphere, and enhance the land-atmosphere interactions. These interactions can be quantified via an accurate parameterization of the exchange processes near the surface. The exchange of mass and energy between forests and atmosphere is governed by a number of parameters among which the roughness lengths for heat and momentum transport feature dominantly. In this context, determination of roughness parameters in a forest environment has become an important research topic.

The roughness length for momentum transport z_0 is defined by the logarithmic wind profile which is valid in the lower part of a neutrally stratified atmospheric boundary layer over homogeneous terrain (Brutsaert, 1982; Stull, 1988). Under neutral conditions for homogeneous surfaces, z_0 is the virtual height of the momentum sink, i.e. the height at which the logarithmic wind speed, extrapolated downward would become zero. When the wind flows above tall and dense canopies, an upward shift of the logarithmic wind profile can be observed and this vertical shift is called the zero-plane displacement height d_0 .

The conventional methods based on flux-gradient approach to determine momentum roughness parameters (z_0 and d_0) uses multiple levels of wind speed measurements observed under neutral conditions. This method requires sufficiently homogeneous surface conditions to have similar source areas for meteorological variables since data from different heights are involved. Moreover to apply the flux-gradient method, the wind speed measurements have to be made in the surface layer where the Monin-Obukhov Similarity Theory (MOST) is applicable. However, presence of the roughness sub-layer (RSL), extending from the forest canopy height to about twice that height, is a complicating factor. When the measurements are made above the forest canopy using towers, the height limitations usually only allow measurements inside the roughness sub-layer. With such measurements the classical flux-gradient approach fails, hence modifications are made to MOST by means of a correction function for RSL effect.

Research on this issue has been carried out, for example, by Garratt (1978, 1980, 1983, 1992), Raupach (1979), Raupach et al. (1980), Cellier and Brunet (1992), Physick and Garratt (1995), Mölder et al. (1999), Harman and Finnigan (2007), Nakai et al. (2008a, 2008b) and more recently by De Ridder (2010). The experimental work on the RSL effect has been conducted over various natural land surfaces ranging from tall agricultural crops to savannah

forests. The results of these investigations revealed that, within the so-called RSL, the observed vertical gradients of meteorological variables are much lower than those predicted by classical surface layer theory. Raupach et al. (1996) have pointed out that within the RSL the momentum transfer is more organized and efficient than the surface layer. Based on the observations they proposed that the vertical gradients within the RSL can be described by a modified theory (using RSL functions) analogous to MOST flux-gradient relationship. In the early forms of RSL functions proposed to modify MOST, the primary assumption was that the non-dimensional gradients depend upon an additional length scale—the RSL height, which can be related to the underlying canopy structure (Garratt, 1978).

Following this assumption and using the RSL height as a length scale, different functional forms have been proposed (Garratt, 1980, 1983, 1992; Cellier and Brunet, 1992; Physick and Garratt, 1995; Mölder et al., 1999; De Ridder, 2010). These functional forms presented in the work cited above are semi-empirical relations and do not fully account for the fundamental physical processes. Although supported by some experimental results, the above functional forms suffer from two major drawbacks. Primarily the RSL height is not a well-defined quantity and existing formulae to estimate it are mostly surface-specific. Secondly these functional forms apart from De Ridder's function have a discontinuity in vertical gradient at the top of the RSL which cannot be physically explained (Garratt, 1992). Alternatively, Harman and Finnigan (2007) presented a more physically based unified theory, which is applicable to flow within the canopy, the RSL and the inertial sub-layer above. They proposed a new length scale, 'the vorticity thickness' which arises from the mixing layer analogy for the flow at a canopy top, to formulate the new form of RSL functions.

On the backdrop of problems associated with flux-gradient technique, an alternative method has been explored to estimate turbulent fluxes with second order turbulent statistics or variance for wind, temperature and humidity measurements (see Kustas et al., 1994). Unlike the flux-gradient approach the flux-variance approach uses data from a single-level sonic anemometer. Further the technique is shown to be robust albeit the measurements are made in the RSL (Katul et al., 1996; Wesson et al., 2001). Moreover the flux-variance method has been previously adopted to estimate aerodynamic roughness parameters having measured the turbulent fluxes simultaneously (Martano, 2000; Prueger et al., 2004). Though the method is unaffected by the above stated measurement problems, a major difficulty associated with the flux-variance method is that it involves a number of empirically determined coefficients. As a result the use of this method to determine roughness parameters is somewhat subjective, unless the coefficients are determined experimentally in advance.

The general objective of the present study is to evaluate these two aerodynamic approaches within the context of estimating roughness parameters of a moderately dense forest stand. More specifically the impacts of associated roughness sub-layer problem will be investigated for flux-gradient approach while focussing on the complementary use of flux-variance method for estimating roughness parameters. To facilitate that, simultaneous observations of micrometeorological and eddy covariance data were made above the forest canopy using equipments attached to a scaffolding tower. The flux-gradient method to estimate roughness parameters, make use of data measured under near-neutral atmospheric conditions with corrections for RSL effect using three different functional forms. The variance method on the other hand employs eddy covariance data measured under unstable atmospheric conditions to validate the estimated roughness parameters of the forest stand. Based on the results of this analysis, a set of values is suggested for few empirical coefficients. Finally an extensive review of the two aerodynamic approaches used for estimating roughness parameters is presented.

3.2 *Experimental Setup*

Standard meteorological measurements were carried out using instruments on the scaffolding tower at the Speulderbos site during the period from June 7 until June 22, 2006. These included wind speed and direction (at 35 m level), air temperature, relative humidity at 4 different heights (43 m, 35 m, 27 m, 1 m) AGL using slow-response combined humidity and temperature sensors and air pressure at 1 m height. A net radiometer (CNR1) was used to measure the incoming and outgoing solar and long-wave radiation above the canopy (at 35 m). Table 3-1 gives an overview of the measurements carried out and the instruments used at different elevations/depths. A complete data set sampled at one minute interval is available from Day of Year 158 to 174 in 2006.

Table 3-1: Overview of the instrumentation at the Speulderbos location

Observation	Instrument	Height(m)
Sensible heat flux	Large Aperture Scintillometer	47
Eddy Covariance data	CSAT3 sonic anemometer (Campbell Sci. Inc.)	47
CO ₂ Fluxes	LI7500 gas analyzer (Li-cor Biosciences)	47
Temperature & Humidity	Combined temperature and humidity sensor	43
Radiation Components (4)	Net Radiometer (Kipp & Zonen- CNR1)	35
Wind speed	Switching Anemometer (Campbell Sci. Inc.)	35
Wind direction	Potentiometer Windvane	35
Temperature & Humidity	Combined temperature and humidity sensor	35, 27 and 1
Soil Moisture	3 Nos. CS616 for soil moisture (Campbell Sci. Inc.)	-0.05, -0.3, -0.55
Soil Temperature	4 Nos. Soil thermistors	-0.01,-0.03, -0.08,-0.9
Soil Heat Flux	3 Nos. Soil heat flux plates HFP01 (Hukseflux)	-0.01

An eddy covariance (EC) system consisting of a three dimensional (3-D) sonic anemometer (CSAT3, Campbell Sci. Inc., USA, 20 Hz) combined with an IR open-path gas analyzer (CS7500, Campbell Sci. Inc., USA, 20 Hz) was used to measure sensible heat, carbon dioxide and water vapor fluxes at the top of the tower (47 m). In addition, the EC system provided measurements of mean and standard deviations of 3-D wind speed, virtual air temperature of the sonic and water vapor, friction velocity and wind direction together with covariance measurements of several variables. The eddy covariance measurements were processed using the software package "ECpack" (<http://www.met.wau.nl/projects/jep/index.html>) and relevant corrections were carried out according to Van Dijk et al. (2004). Half-hourly averaged processed EC data were available for the analysis from Day of Year 164 to 191 in 2006. Figure 3-1 and Figure 3-2 show half-hourly averages of wind speed and wind directions respectively at two measurement heights.

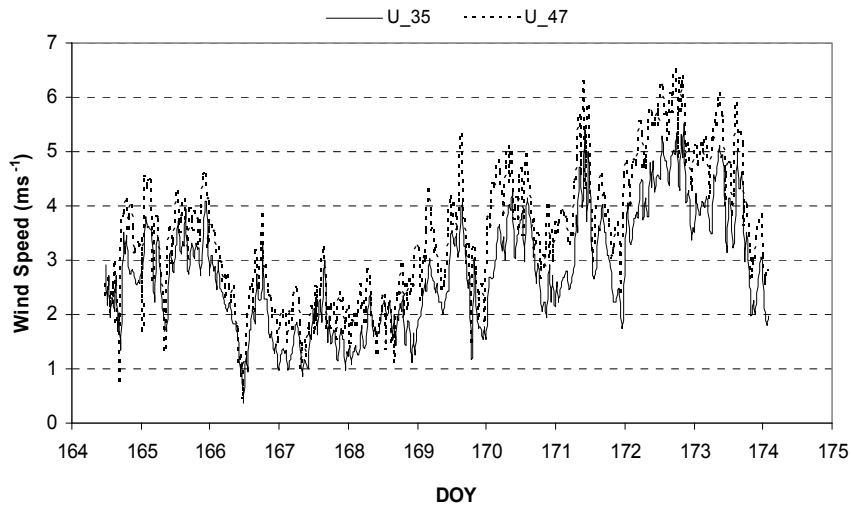


Figure 3-1: Comparison of wind speed at 35m and 47m at Speulderbos

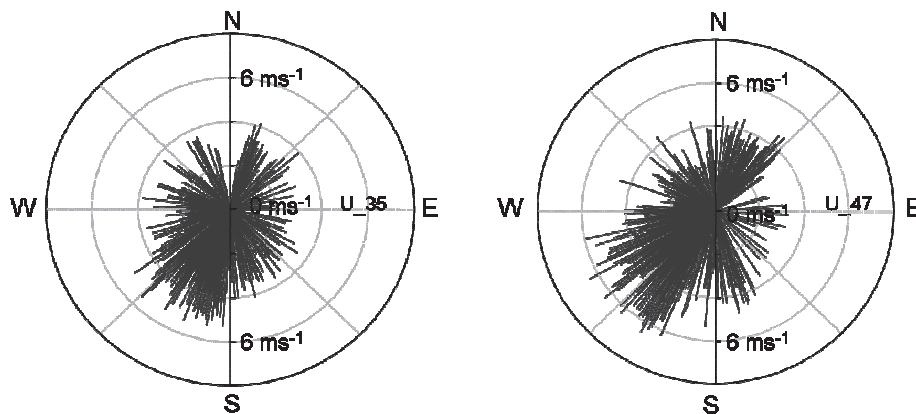


Figure 3-2: Comparison of wind direction at 35m and 47m at Speulderbos

3.3 Modified Monin-Obukhov similarity theory

Using the modifications to MOST proposed by Garratt (1978, 1980, 1992), over large-roughness surfaces (e.g. tall crops and forests) the gradient of the wind speed u with height z measured from the ground surface may be written as

$$\frac{\partial u}{\partial z} = \frac{u_*}{k(z - d_0)} \Phi_m(\zeta) \phi_m(\xi) \quad (3-1)$$

where u_* is the friction velocity, k von Karman's constant, $\zeta=(z-d_0)/L$, with L the Monin-Obukhov length, $\xi=(z-d_0)/(z_*-d_0)$ a non-dimensional height, with z_* the roughness sub-layer height for momentum. Function Φ_m relates to the atmospheric stability, while function ϕ_m determines the effect of the roughness sub-layer.

By integrating Eq. (3-1) between z_0 and z and following Physick and Garratt (1995), an expression for u valid for $z \leq z_*$ can be given as

$$u \frac{k}{u_*} = \ln\left(\frac{z-d_0}{z_0}\right) - [\psi_m(\zeta) - \psi_m(z_0/L)] + \psi_u(z) \quad (3-2)$$

where the function $\psi_u(z)$ is the integrated form of combined stability RSL influence (within the limits z to z_*) given by

$$\psi_u(z) = \int_z^{z_*} \frac{\Phi_m(\zeta)[1-\phi_m(\xi)]}{z'-d_0} dz' \quad (3-3)$$

A number of different expressions for non-dimensional stability correction or Φ_m function and its integrated form (ψ_m) are given for both unstable ($\zeta < 0$) and stable ($\zeta > 0$) atmospheres (see Prueger and Kustas (2005) for an exhaustive review).

For a neutrally stratified atmosphere the stability corrections can be ignored, hence the function $\psi_u(z)$ (Eq. (3-3)) reduces to

$$\psi_u(z) = \int_z^{z_*} \frac{[1-\phi_m(\xi)]}{z'-d_0} dz' \quad (3-4)$$

The integral $\psi_u(z)$ given by Eq. (3-4) exclusively accounts for the roughness sub-layer effect depending on the assumed RSL function.

3.3.1 Different forms of RSL profile functions

The RSL functions proposed by Garratt (1980, 1983) for observation over tall crops and trees take the following exponential form as given by Garratt (1992).

$$\phi_m(\xi) = \exp[-0.7(1-\xi)] \quad (3-5)$$

Based on the same observations a slightly different form is presented by Physick and Garratt (1995).

$$\phi_m(\xi) = 0.5 \exp(0.7\xi) \quad (3-6)$$

Using flux and profile data measured over a tall homogeneous agricultural crop a different RSL function proposed by Cellier and Brunet (1992) is of the form

$$\phi_m(\xi) = \xi^n \quad (3-7)$$

The functional form given by Cellier and Brunet (1992) has been evaluated by Mölder et al. (1999) using flux and profile measurements carried above a mixed pine-spruce forest. Using the measurements carried out both above and within the RSL, they obtained values for RSL height, $z_* = 1.85 h_c$ and n approximately equal to 0.6.

Recently De Ridder (2010) proposed the following profile function given as

$$\phi_m(\xi) = 1 - \exp(-\mu\xi) \quad (3-8)$$

By fitting the profile function to data presented in Mölder et al. (1999), they found that the empirical coefficient $\mu = 2.59$ gives the best agreement.

All the above presented functional forms are semi-empirical. They make use of the non-dimensional height ξ , hence the knowledge of RSL height is a prerequisite to apply the above functional forms. All profile functions suffer from non-physical discontinuity at the top of the RSL with the exception of De Ridder's function. Besides that, the main difficulty in applying these functional forms is the lack of a robust method to estimate the RSL height.

In the literature several empirical expressions are presented to estimate RSL height however there is no general consensus. Early work of Garratt (1980) suggested that z_* can be related to a length scale, δ , which is the average horizontal inter-element spacing. Several experimental works have investigated the relationship $z_* = d_0 + c\delta$ and have reported that value of c varies between 3 and 5. Raupach et al. (1991) expressed z_* as a multiple of canopy height with z_*/h_c in the range 2-5. Arya (2001) gives $z_*/h_c \approx 1.5-2.5$ whereas the experimental evidence of Mölder et al. (1999) suggest that $z_*/h_c \approx 2$ for a boreal forest of a height of about 25 m. Also the value of $z_*/h_c \approx 2$ is consistent with the mean value obtained with different expressions given in Verhoef et al. (1997) and Graefe (2004) for tall canopies. Considering the range of estimates found in the empirical formulae, $z_*/h_c = 2$ can be regarded as a representative value for tall canopies.

Harman and Finnigan (2007) introduced a new unified theory which can be used to describe wind speed profile within the canopy, the RSL and the inertial sub-layer over a range of canopy types and atmospheric stabilities. They formulated the modifications to the surface-layer profiles through the mixing layer analogy for the flow at a canopy top. Thereby they proposed a new length scale on which the RSL function reflects the influence of the canopy structure on the flow above. This relevant length scale for the RSL function is defined as $u/(du/dz)$ at the inflection point at canopy top. Harman and Finnigan (2007) proceeded by following Inoue (1963) proposed shape for the within canopy wind speed profile given by

$$u(z) = u_h \exp\{\beta z/l\} \quad (3-9)$$

where $u_h = u_{(z=h)}$, $\beta = u_*/u_h$ and l is the mixing length.

Eq. (3-9) gives $u/(du/dz) = l/\beta$

Using the new length scale l/β , the integrated RSL function of Eq. (3-4) can be rewritten as

$$\psi_u(z) = \int_z^\infty \frac{\left[1 - \phi_m\left(\frac{z'}{l/\beta}\right)\right]}{z' - d} dz' \quad (3-10)$$

Rather than specifying a priori RSL height, Harman and Finnigan (2007) proposed that the RSL influence decreases with increasing height (i.e. $\phi_m = 1$ when $z \rightarrow \infty$) which makes the limits of integral of Eq.(3-10) different from Eq. (3-4).

The new RSL function of Harman and Finnigan (2007) takes the form

$$\phi_m(z) = 1 - c_1 \exp[-\beta c_2 (z - d_0)/l] \quad (3-11)$$

where $c_1 = [1 - k/(2\beta)] \exp(c_2/2)$ and $c_2 = 0.5$

3.4 Estimation of roughness parameters for neutral stability.

In the neutrally stratified atmosphere ($\zeta=0$) above the RSL the logarithmic wind profile equation in its simplest form is given as

$$u = \frac{u_*}{k} \ln \left(\frac{z - d_0}{z_0} \right) \quad (3-12)$$

If u_1 and u_2 are wind speed measurements at heights z_1 and z_2 respectively and u_* is the friction velocity measured at one of these heights, using Eq. (3-12) we can algebraically express d_0 and z_0 as (Nakai et al., 2008a).

$$d_0 = \frac{z_2 \exp(ku_1/u_*) / \exp(ku_2/u_*) - z_1}{\exp(ku_1/u_*) / \exp(ku_2/u_*) - 1} \quad (3-13)$$

$$z_0 = \frac{z_1 - d_0}{\exp(ku_1/u_*)} \quad (3-14)$$

3.4.1 Selection of data for near-neutral stability

In order to obtain d_0 and z_0 we used the wind speed measured at 35 m height (U_{35}) using the switching anemometer and wind speed measured at 47 m height (U_{47}) together with friction velocity and sensible heat flux measured with the Eddy Covariance system. Temperature measurements at 35 m and 43 m (T_{35} and T_{43}), both observed with slow-response combined temperature and humidity sensors were used to calculate the temperature gradient. All the measurements were pre-processed and averaged over a period of 30 minutes for the estimation of d_0 and z_0 using Eqs. (3-13) and (3-14). We used the gradient Richardson number (Ri) criterion (see Garratt (1992) for details) in order to select measurements made under neutral conditions. Out of 460 half-hourly averaged measurements, there were 90 observations satisfying the adopted criterion ($|Ri| \leq 0.05$) for near-neutral stability.

Using the estimated results of z_0 and d_0 we examined the theoretical linear relationship suggested by Thom (1971), de Bruin and Moore (1985) and Nakai et al. (2008a):

$$z_0 = \mu(h_a - d_0) \quad (3-15)$$

where h_a is the aerodynamic canopy height and μ is a dimensionless constant specific to a stand. De Bruin and Moore (1985) found $\mu = 0.22$. We determined the parameters μ and h_a using a Geometric Mean Regression (GMR) model (Zobitz et al., 2006) which minimizes both vertical and horizontal residuals of the regression of 90 half-hourly observations.

3.4.2 Correction for roughness sub-layer effect

Assuming that our measurements were carried out within the RSL, the logarithmic wind profile equation for neutral conditions can be modified as

$$u \frac{k}{u_*} = \ln\left(\frac{z - d_0}{z_0}\right) + \psi_u(z) \quad (3-16)$$

where $\psi_u(z)$ is given by either Eq. (3-4) or Eq. (3-10)

Following Nakai et al. (2008a) d_0 and z_0 with RSL corrections can be expressed as

$$d_0 = \frac{z_2 \exp(ku_1/u_* - \psi_u(z_1)) / \exp(ku_2/u_* - \psi_u(z_2)) - z_1}{\exp(ku_1/u_* - \psi_u(z_1)) / \exp(ku_2/u_* - \psi_u(z_2)) - 1} \quad (3-17)$$

$$z_0 = \frac{z_1 - d_0}{\exp(ku_1/u_* - \psi_u(z_1))} \quad (3-18)$$

In order to compare the results of d_0 and z_0 obtained using different RSL functional forms, $\psi_u(z)$ were evaluated with ϕ_m functions given in Eq. (3-7), Eq. (3-8) and Eq. (3-11) above.

The solution for $\psi_u(z)$ with ϕ_m given by Eq. (3-7) is as follows.

$$\psi_u(z) = -\ln(\xi) + \frac{1}{n} [\xi^n - 1] \quad (3-19)$$

where the value of n is equal to 0.6 and z_* is estimated to be $1.85h_c$ based on experimental results of Mölder et al. (1999).

The approximated expression for $\psi_u(z)$ using ϕ_m function of Eq. (3-8) is given as

$$\psi_u(z) = \frac{1}{\lambda} \ln\left(1 + \frac{\lambda}{v\xi}\right) e^{-v\xi} \quad (3-20)$$

with $v=2.59$, $\lambda \approx 1.5$ and ξ as described earlier.

Since no simple analytic form can be found for $\psi_u(z)$ of Eq. (3-10) with ϕ_m function given in Eq. (3-11), the solution was obtained by numerical integration. Given that only the canopy height and the cumulative leaf area

index (LAI) were known, the procedure outlined by Harman and Finnigan (2007) for implementation with limited information was followed. It was assumed that $c_d = 0.25$, $l = 2\beta^3/(ac_d)$ and $a = LAI/h_c$ for the forest stand investigated here. The parameter β was determined iteratively so that it satisfies the relationship $4\beta^2 h_c/LAI = h_c - d_0$ of Harman and Finnigan (2007).

When solving Eqs. (3-16) and (3-17) with ψ_u as given above, an initial estimate for d_0 is needed. Nakai et al. (2008a) method has omitted the iterative procedure and used the average d_0 obtained from Eq. (3-13) to evaluate ψ_u . However, this is only allowed if the ψ_u values are sufficiently small. In this study we used a variable d_0 value obtained with Eq. (3-13), strictly as a starting point to achieve the full iterative solution of the system of equations.

3.5 Estimation of roughness parameters using EC measurements.

z_0 and d_0 can also be determined from eddy covariance measurements of sensible heat flux H , standard deviations of vertical wind velocity and air temperature (σ_w and σ_T respectively) and mean wind speed u (Kustas et al., 1994; Prueger et al., 2004). The wind speed in non-neutral atmospheric conditions is generally determined by the three terms on the right-hand side of Eq. (3-2), i.e. the logarithmic term, the stability correction function and the term that accounts for the roughness sub-layer effect. Kustas et al. (1994) and Prueger et al. (2004) only retain the following terms in their analysis

$$u \frac{k}{u_*} = \ln\left(\frac{z - d_0}{z_0}\right) - \psi_m(\zeta) \quad (3-21)$$

where $\psi_m(\zeta)$ is the integrated stability correction function. Neglecting the roughness sub-layer in a forest environment seems only allowed when z is close to z^* or higher. The term $\psi_m(z_0/L)$ in Eq. (3-2) is much smaller than $\psi_m(\zeta)$ and has also been left out.

The Monin-Obukhov length L (Monin and Obukhov, 1954) is taken as

$$L = \frac{\rho C_p u_*^3 T_a}{kg(H + 0.61T_a C_p E)} \quad (3-22)$$

where T_a is the air temperature (K), g the acceleration of gravity (ms^{-2}), ρ the air density (kgm^{-3}), C_p the specific heat of air ($\text{Jkg}^{-1}\text{K}^{-1}$), H is the sensible

heat flux (Wm^{-2}), E is the rate of surface evaporation ($\text{kgm}^{-2}\text{s}^{-1}$) and where all the other parameters have been defined earlier.

The sensible heat flux (H) under unstable conditions can be estimated using the standard deviation in air temperature (σ_T) and the standard deviation in the vertical component of wind velocity (σ_w). The following relation was derived by Tillman (1972)

$$H = -\rho C_p u_* (\sigma_T / C_1) [C_2 - \zeta]^{1/3} \quad (3-23)$$

where C_1 and C_2 are determined experimentally.

If estimates of u_* are available, sensible heat fluxes can be calculated using Eq. (3-23) for unstable atmospheric conditions. The following relationship between u_* and σ_w (for unstable conditions) was derived by Panofsky and Dutton (1984)

$$u_* = \frac{\sigma_w}{a(1 - b\zeta)^{1/3}} \quad (3-24)$$

where a and b are surface-specific constants need to be calibrated experimentally (Hicks, 1981; Wesely, 1988; De Bruin et al., 1993; Kustas et al., 1994). Provided that all other parameters are known, one can estimate u_* either using σ_w measurements with Eq. (3-24) or using wind speed measurements with stability corrections using Eq. (3-21).

3.5.1 Selection of data for unstable conditions

In this method we utilized the eddy covariance data observed under unstable atmospheric conditions. All the variables used in the analysis were measured at an elevation of 47 m using the 3-D sonic anemometer. Data under unstable condition were selected so that the estimated $\zeta < -0.08$. In general the Equations (3-21) to (3-24) are used to estimate H , having measured the variables u , σ_w and σ_T at a known height above a particular surface. In such a situation, the aerodynamic roughness parameters and the locally evaluated coefficients have been used in the determination of H . However, if measurements of H and u_* are available too, the method can be applied in the inverse mode to determine aerodynamic roughness parameters z_0 and d_0 .

3.5.2 Estimation of sensible heat flux

The sensible heat flux H is determined iteratively (Kustas et al. 1994). A large negative value is assigned to L (e.g. -1×10^6 m) which is used to compute u_* either by using Eq. (3-21) employing u measurements (*option A*)

or else using Eq. (3-24) with σ_w measurements (*option B*). With the estimates of u_* and L , Eq. (3-23) was used to compute H employing the σ_T measurements. After that L is recalculated with Eq. (3-22) using the H value obtained in the previous step. The procedure is repeated until convergence is achieved, i.e. when the absolute difference between subsequent L values becomes less than 0.001 m.

3.5.3 Evaluation of coefficients

Several studies indicate that the coefficients used in the above formulation differ with surface type and condition (De Bruin et al., 1991; Padro, 1993). Preferably the coefficients should be evaluated using the measured fluxes from the eddy covariance system. Data from previous studies mention that C_1 is of order 1, though it appears to vary from 0.95 to 1.25 (Wyngaard et al., 1971; Tillman, 1972; Hicks, 1981; Wesely, 1988; Kader and Yaglom, 1990; De Bruin et al., 1993; Kustas et al., 1994). The coefficient C_1 is more critical because the H values determined with Eq. (3-23) are sensitive to changes in its value. In the analysis we evaluated the impact of coefficients C_1 within the range from 0.9 to 1.2. The variation in the value of C_2 had little effect on the computed fluxes. Thus we computed $C_2 = (C_1/2.5)^3$ as reported by past experimentation (Wesely, 1988; Kader and Yaglom, 1990). We also allowed the coefficient a and b to vary and derived best values through an optimization technique.

3.5.4 Estimation of d_0 and z_0

The iteration procedure to estimate H and u_* via *option A* in 3.3.2 uses both d_0 and z_0 whereas *option B* needs only d_0 , in addition to the coefficients and observed variables. We assumed that the best agreement between the estimated and measured H and u_* should produce the correct values for d_0 and z_0 . To obtain the best agreement between the estimated and measured fluxes, we used the coefficient of determination, r^2 as the indicator. For the best agreement the r^2 should be close to 1. Having observed the fluxes of H and u_* we were able to calculate indicators r^2_H and $r^2_{u^*}$ for H and u_* respectively in a single run. In order to obtain a set of best performing d_0 and z_0 , we maximized the average indicator $[0.5 r^2_H + 0.5 r^2_{u^*}]$ for the best agreement between estimated and measured fluxes of H and u_* . We also used the loop iteration *option B* of 3.3.2 to derive values for d_0 and coefficients a and b . We used the same optimization technique as in *option A* to derive the best performing values for d_0 and coefficients a and b . We repeated the procedure for both options while varying the coefficient C_1 from 0.9 to 1.2 in steps of 0.05.

3.6 Results and Discussion

The difficulties associated with determining d_0 and z_0 with the methods outlined in sections 3.1 and 3.2 can best be illustrated with an example (see Figure 3-3). Suppose that we have a forest with $d_0 = 20$ m, $z_0 = 1.25$ m, $u_* = 0.5$ ms⁻¹, $z_* = 50$ m, then the vertical wind speed profile can be calculated according to the methods of Nakai et al. (2008a, 2008b). We calculated the wind speed profiles using the simple exponential function (Eq. (3-12)) and also using (Eq. (3-16)) with the RSL corrections of Mölder et al. (1999), De Ridder (2010) and Harman and Finnigan (2007). Figure 3-3(a) shows the four profiles, where the different line types are explained in the figure caption. Also shown are two points corresponding to the measuring heights used in the field campaign. The solutions according to De Ridder (2010) are $u_1 = 3.78$ ms⁻¹ for $z_1 = 47$ m and $u_2 = 3.20$ ms⁻¹ for $z_2 = 35$ m. There is not much difference with the solutions by Mölder et al. (1999) and Harman and Finnigan (2007) as shown in Figure 3-3(a). The problem now is to use the solution points (u_1, z_1) and (u_2, z_2) to inversely estimate d_0 and z_0 , which should of course yield the starting values 20 m and 1.25 m.

The results of various methods are shown in Figure 3-3(b). The simple exponential solution by Nakai et al. (2008a) using Eqs. (3-13) and (3-14), yields values $d_0 = 15.5$ m and $z_0 = 1.41$ m. It is clear that this procedure may lead to severe underestimation of d_0 when the second measuring point is low above the canopy. The improved method by Nakai et al. (2008a) (Eqs. (3-17) and (3-18)) uses the roughness sub-layer functions ψ_u . However, as mentioned before, the authors use the average d_0 obtained through the simple exponential method. The solution of this second method is also illustrated in Figure 3-3(b) with a dotted line. The results for this example are $d_0 = 18.9$ m and $z_0 = 1.30$ m. Again the value of d_0 is lower than the starting value. When the Eqs. (3-17) and (3-18) are solved iteratively, the correct starting values are retrieved ($d_0 = 20$ m and $z_0 = 1.25$ m) as shown by the line with long dashes. This example illustrates that even the improved method by Nakai et al. (2008a) may slightly underestimate the forest displacement height when the wind velocity observation points are low in the roughness sub-layer. The iterative solution method is recommended in any case.

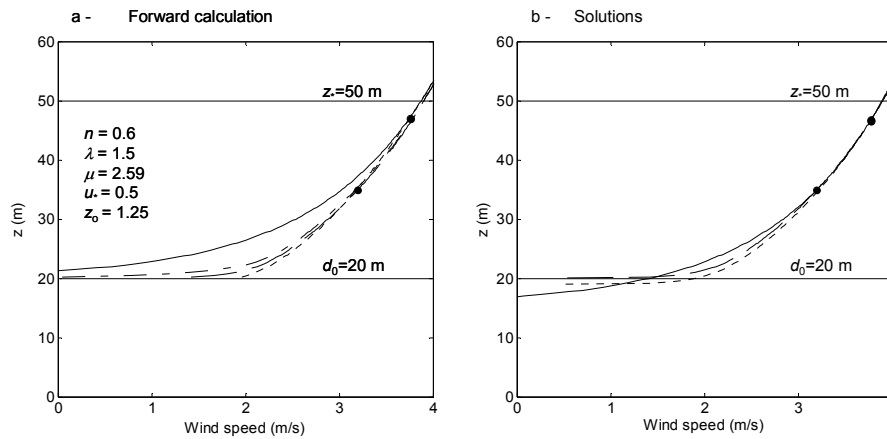


Figure 3-3: Predicted wind profiles for neutral conditions. (a) Forward calculations with different $\psi_u(z)$. Dotted line: Mölder et al. (1999); dashed line: De Ridder (2010); dash-dotted line: Harman and Finnigan (2007); solid line: the simple logarithmic profile. (b) Different solutions. Solid line: the simple exponential solution; dotted line: non-iterative solution by Nakai et al. (2008a); dashed line: fully iterative solution (proposed here). Two filled circles indicate the wind speed corresponding to measuring heights.

The results obtained for d_0 and z_0 using the wind profile method with and without the roughness sub-layer correction are listed in Table 3-2. The first row of the table gives the average values obtained for simple exponential solution using Eqs. (3-13) and (3-14). Also listed are the average values obtained for d_0 and z_0 with RSL corrections using Eqs. (3-17) and (3-18). The corrected values were obtained by the full iterative method with $\psi_u(z)$ evaluated using the three functional forms discussed above. The linear relationship of Eq. (3-15) is illustrated in Figure 3-4 for the four cases given in Table 3-2. The GMR model (Zobitz et al., 2006) yields values of aerodynamic canopy height (h_a) and μ also listed in Table 3.2 against each method. The values in Table 3-2 clearly indicate the large differences between the simple exponential solution and the iterative solutions proposed here in combination with RSL corrections. An increase of 6 to 8 m is evident from the RSL effect corrected d_0 values compared to the non-corrected value whereas the comparable z_0 values show a decrease of 0.15 to 0.40 m. Further it can be seen that the h_a and μ values obtained with corrections of Mölder et al. (1999) and De Ridder (2010) correspond closely while these values are notably different from the equivalent estimates yielded with Harman and Finnigan (2007).

Table 3-2: Comparison of roughness sub-layer effect on aerodynamic parameters using different RSL corrections.

Method	z_0 (m)	d_0 (m)	h_a (m)	μ
Simple exponential solution with no correction	1.55	19.94	31.30	0.131
Correction with iteration (Mölder et al., 1999)	1.16	28.37	37.94	0.121
Correction with iteration (Harman and Finnigan, 2007)	1.41	26.20	30.83	0.305
Correction with iteration (De Ridder, 2010)	1.27	26.97	37.26	0.123

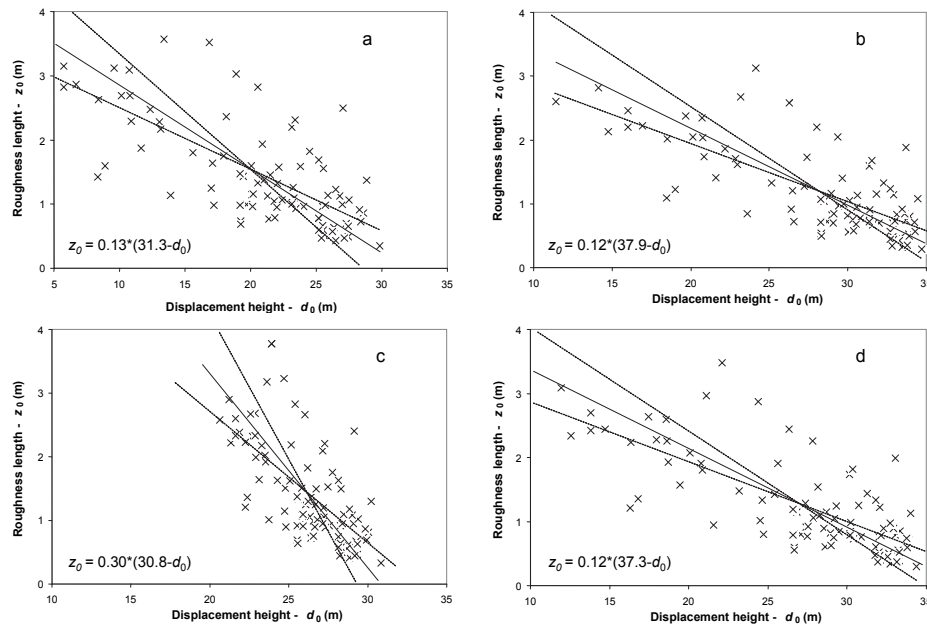


Figure 3-4: The observed linear relationship between d_0 and z_0 estimated for neutral stability. (a) No RSL corrections; (b) With RSL corrections- $\psi_u(z)$ of Mölder et al. (1999); (c) With RSL corrections - $\psi_u(z)$ of Harman and Finnigan (2007); (d) With RSL corrections - $\psi_u(z)$ of De Ridder (2010). Dashed lines: regression by ordinary least square technique. Solid line: described linear equation obtained with geometric mean regression technique.

In order to assess the validity of our results we compared them to previously reported values. Use is made here of data compiled by Garratt (1992), Nakai et al. (2008a), Mölder et al. (1999) which in turn quote many older findings. The displacement height is plotted in Figure 3-5(a) as a function of tree top

height h_c . The figure shows the results of over 25 studies. Our results are indicated in the graph using the cross symbol. The results compiled by Nakai et al. (2008a) are shown as small diamonds, while the results collected by Garratt (1992) are represented by solid triangles. The open triangle shows the results obtained by Mölder et al. (1999). The circles indicate the results obtained in the Douglas fir forest, i.e. the value from Bosveld (1997) dating from 1989 when the trees were 18m tall, and the present results from 2006 when the trees had grown to 32 m (Weligepolage et al., 2012).

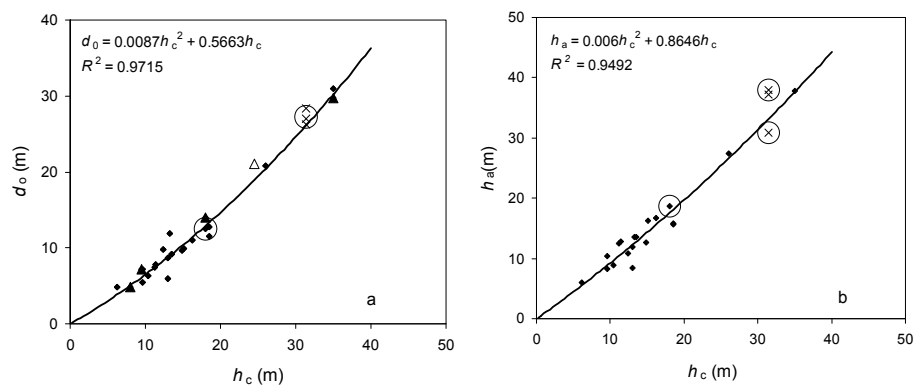


Figure 3-5: Displacement height d_o (in panel a) and Aerodynamic canopy height h_a (in panel b) as a function of h_c for selected forest studies. Solid lines show the described quadratic equations. Crosses show the result of the present study. The results in the same study area: the 1989 study by Bosveld (1997) and the present study carried out in 2006 are enclosed with circles.

Although it is possible to fit a linear relationship through the points of Figure 3-5(a), the quadratic relationship: $d_o = 0.0087h_c^2 + 0.566h_c$ fits the data with slightly better $R^2 = 0.97$. It is important to pay attention to the units (here in meters) of the proposed quadratic equation since it is not dimensionally homogeneous. This relation leads to higher d_o/h_c values for taller tree canopies, as has also been reported in the studies cited above. The values shown in the figure are derived from many different deciduous and coniferous tree types in climates ranging from tropical to semi-arid and boreal. The figure also shows that the results presented here, fit the relationship well. It is also clear that the figures reported by Bosveld (1999) of the same forest 15 years earlier fit the relation well, despite the fact that the forest was thinned out several times from 780 trees/ha in 1989 to 375 trees/ha in 2006. The aerodynamic height h_a is shown in Figure 3-5(b) as a function of tree top height h_c where use is made of the values reported by Nakai et al. (2008a). Again a quadratic relationship: $h_a = 0.006h_c^2 + 0.865h_c$ (units meters) with $R^2 = 0.95$ is proposed. The h_a values found in this study (indicated by crosses) are in reasonable agreement with the general trend. Especially the h_a value

derived using the RSL corrections of Harman and Finnigan (2007) fits the predicted relationship of Figure 3-5(b) rather well.

We compared vertical profiles of the wind speed, predicted using surface-layer theory and modified theory with different RSL corrections to the average observations in near-neutral conditions. As stated above, the unified theory of Harman and Finnigan (2007) is capable of predicting the complete wind speed profile within and above the canopy. Since the vertical profiles are coupled at the canopy top, the authors have used the observed within-canopy profiles in the upper half of the canopy to determine β and l by a least squares estimate using Eq. (3-9). Since we did not have wind speed profile measurements within the canopy, this was not possible. Consequently our comparison is limited to the above canopy vertical profiles. Figure 3-6 shows the predicted wind speed profile using the ψ_u given by Harman and Finnigan (2007), the corresponding prediction using the ψ_u given by De Ridder (2010) and the extrapolated surface-layer profile with different line types. The corresponding prediction using the ψ_u given by Mölder et al. (1999) is rather similar to that of De Ridder (2010) hence not shown here. Also shown in Figure 3-6 are the average observed values at 35 m and 47 m above the ground where the error bars denote the standard deviation. The averages shown here are based on 90 near-neutral observations. The three profiles shown in Figure 3-6 were predicted using constant values of d_0 and z_0 selected in such a way that, the profile of Harman and Finnigan (2007) passes through the average observations. Figure 3-6 clearly shows the deviation of surface layer profile from the observations and the relative importance of RSL corrections with increasing height. When the observation level is closer to the canopy top, the differences between the two RSL corrected profiles are substantial compared to the upper observation level (which is 15 m above the canopy) and beyond that level the two profiles are indistinguishable. Also the profile predicted with the Harman and Finnigan (2007) approach deviates from the surface layer profile up to a height of 30 m above the canopy level, indicating that the influence of RSL is nearly two times the h_c .

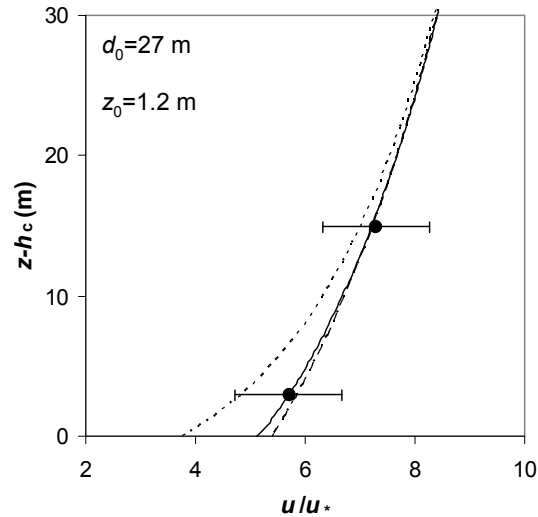


Figure 3-6: Comparison of vertical profiles of mean wind speed above the canopy to average observations in neutral conditions. Solid line: predicted profile using the $\psi_u(z)$ given by Harman and Finnigan (2007); dashed line: predicted profile using the $\psi_u(z)$ given by De Ridder (2010); dotted line: the extrapolated surface layer profile. Filled circles denote the average observed values at 35 m and 47 m above the ground where the error bars denote the standard deviation.

In section 3.5 a framework was described to use second order turbulent statistics with the variance technique for determination of aerodynamic roughness under unstable atmospheric conditions. The results obtained for d_0 and z_0 using option A described in section 3.5.2 are listed in Table 3-3 for different values of coefficients C_1 . The variation in d_0 and z_0 with respect to the value of C_1 suggests that both are quite sensitive to the coefficient C_1 . The inverse relationship between C_1 and d_0 is clearly evident as d_0 decreases by nearly 60% when the value of C_1 is increased from 0.9 to 1.2. The same increment of C_1 yields nearly 75% rise in z_0 from 0.95m to 1.75m. In view of d_0 and z_0 values estimated for near-neutral conditions, it appears that the value of C_1 could be between 1.0 and 1.1 where the upper value was reported by Kustas et al. (1994). However the mean bias estimate (MBE) (the statistical formulae are defined in Kustas et al. Table 3) in H (roughly about $+5 \text{ Wm}^{-2}$) indicates that the estimated sensible heat fluxes using the optimized parameters are systematically higher than the observed values.

Table 3-3: The best performing values of d_0 and z_0 estimated by varying the coefficient C_1

C_1	0.90	0.95	1.00	1.05	1.10	1.15	1.20
d_0	32.32	29.87	27.18	24.24	21.03	17.55	13.79
z_0	0.95	1.07	1.20	1.33	1.46	1.60	1.75
r^2_H	0.8857	0.8860	0.8864	0.8867	0.8870	0.8872	0.8874
$r^2_{U^*}$	0.6860	0.6922	0.6975	0.7020	0.7057	0.7088	0.7113
MBE_H	5.27	4.92	4.58	4.23	3.89	3.55	3.23
MBE_{U^*}	-0.01	-0.01	-0.01	-0.01	0.00	0.00	0.00

The results obtained for d_0 and coefficients a and b using option B described in 3.5.2 for different values of coefficients C_1 are presented in Table 3-4. Results show that the estimated d_0 values are systematically higher than the corresponding option A values in Table 3-3. However the same inverse relationship between C_1 and d_0 is evident here. Furthermore we observed that the derived value of coefficient a (1.3) matches with the previously reported experimental value and is totally insensitive to the value of coefficient C_1 . Nevertheless, the average value of coefficient $b = 0.40$ is rather low compared to the previously suggested value of 2. With C_1 between 1.0 and 1.1 both the options A and B yielded z_0 and d_0 reasonably matching the equivalent estimates of near-neutral conditions. However a comparatively low mean bias estimate in H (-0.11 Wm^{-2}) was noted with option B . If the mid value of the plausible range is assigned to C_1 (i.e. 1.05), the value of C_2 becomes 0.07. We opted for the d_0 corresponding to $C_1 = 1.05$ from option B because the statistical indicators (MBE , r^2_H and $r^2_{U^*}$) are marginally better compared to those of option A . These values for C_1 and C_2 were adopted to derive the remaining parameters through the optimization procedure. The results for options A and B are presented in Table 3-5 which indicates that the mean bias estimate in H has improved in option A for the adopted value of d_0 .

Table 3-4: The best performing values of d_0 , a and b estimated by varying the coefficient C_1

C_1	0.90	0.95	1.00	1.05	1.10	1.15	1.20
d_0	34.01	31.72	29.18	26.37	23.28	19.90	16.21
a	1.30	1.30	1.30	1.30	1.30	1.30	1.30
b	0.60	0.51	0.44	0.38	0.33	0.29	0.25
r^2_H	0.9176	0.9176	0.9176	0.9176	0.9176	0.9176	0.9176
$r^2_{U^*}$	0.7385	0.7385	0.7385	0.7385	0.7385	0.7385	0.7385
MBE_H	-0.11	-0.11	-0.11	-0.11	-0.11	-0.11	-0.11
MBE_{U^*}	0.00	0.00	0.00	0.00	0.00	0.00	0.00

Figure 3-7 and Figure 3-8 illustrate the comparison of H values estimated in options A and B respectively with the eddy covariance measurements. The scatter plots show that, overall agreement is strong with points falling along the 1:1 line without obvious bias. However, there is considerably more scatter present for higher values of the sensible heat fluxes. A comparison of estimated H from option A against option B is shown in Figure 3-9. It is evident from the scatter plot that points are strictly following the 1:1 line with a very high correlation coefficient almost equal to 1. The close agreement between the two sets of estimated fluxes lends support to the validity of the present analysis. The method seems to be quite useful as an alternative to the wind profile technique as the latter method is affected by practical and theoretical limitations. Also unlike the traditional flux-gradient method, the variance method option B appears to be less affected by position within the roughness sub-layer and measurements are not constrained by flow distortion or wind direction (Kustas et al., 1994; Prueger et al., 2004). When using option A it is important that wind measurements are taken high above the canopy closer to z^* to minimize roughness sub-layer effects in relation (3-21).

Table 3-5: Model results for recommend coefficients and best performing values of roughness parameters.

Opt.	C_1	a	b	d_0	z_0	$RMSE H$	$MBE H$	$RMSE U^*$	$MBE U^*$	r^2_H	$r^2_{U^*}$
				(m)	(m)	(Wm^{-2})	(Wm^{-2})	(ms^{-1})	(ms^{-1})		
A	1.05	-	-	26.37	1.25	32.58	-0.68	0.09	-0.01	0.89	0.70
B	1.05	1.3	0.38	26.37	-	27.78	-0.11	0.09	0.00	0.92	0.74

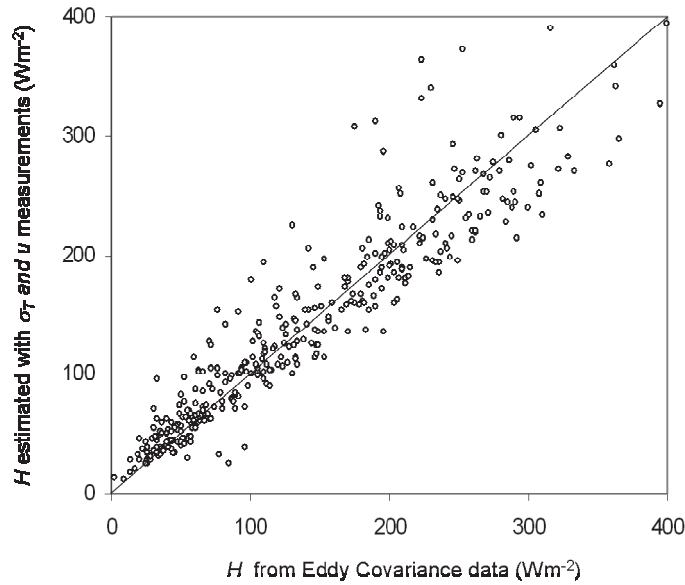


Figure 3-7: Comparison of eddy covariance H vs. estimated H using σ_T and u measurements as in option A.

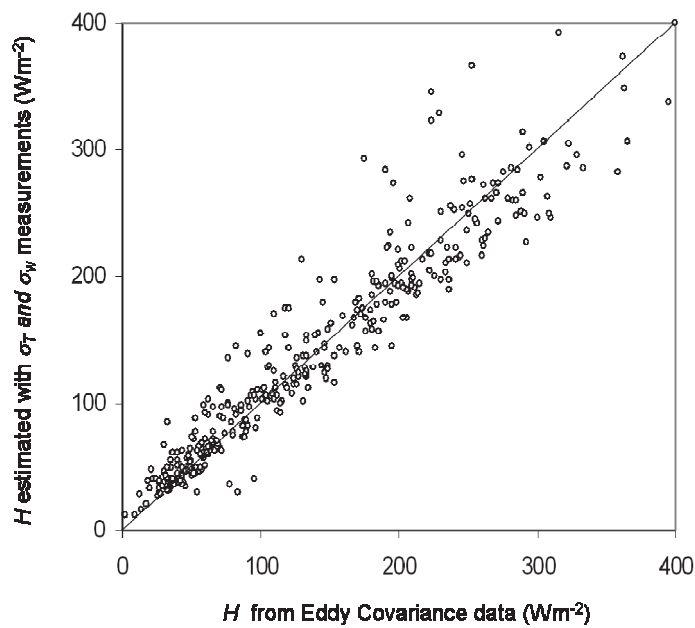


Figure 3-8: Comparison of eddy covariance H vs. estimated H using σ_T and σ_w measurements as in option B.

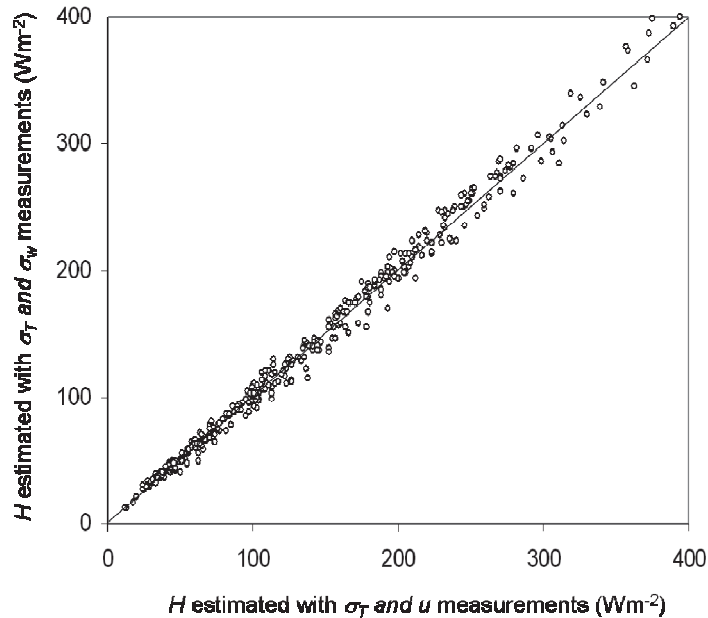


Figure 3-9: Comparison of H estimated from options A (horizontal) and B (vertical).

3.7 Conclusions

The study investigated two methods that use micrometeorological variables in combination with second order turbulent statistics to estimate aerodynamic roughness parameters of a tall conifer forest. When the method based on the flux gradient relationship with wind speed and momentum flux measurements was used, modifications to surface layer theory proved to be important because of the low height of measurements above the canopy. The method that used modified surface layer theory by integrating three different RSL functional forms, yielded compatible estimates of average z_0 and d_0 while the values substantially differ from equivalent estimates obtained with classical surface layer theory. Nevertheless the non-iterative method proposed by Nakai et al. (2008a) should be modified into a fully iterative solution in order to avoid potential underestimation of the displacement height.

The RSL corrected average estimates of d_0 vary between 26.2 m to 28.4 m. This gives the average quotient $d_0/h_c \approx 0.85$ which is in very good agreement with the value found by Mölder et al. (1999) for a mixed pine-spruce forest. As already stated, when RSL corrections were implemented following Mölder et al. (1999) and De Ridder (2010), values for n and z_* had to be specified. Ideally these values should have been determined with profile measurements

carried out both in and above the roughness sub-layer as performed by Mölder et al. (1999). Since we adopted n ($=0.6$) and z^* ($=1.85 h_c$) following Mölder et al. (1999), naturally the results of the current study would be inclined towards their results. In the absence of predetermined values for n and z^* for the studied forest, we found that the RSL corrections of Harman and Finnigan (2007) yielded the best overall estimate of three aerodynamic parameters.

By analyzing our results together with many other previous findings, it was shown that both d_0 and h_a can be modelled as quadratic functions of h_c . Furthermore, given that z_0 and d_0 are coupled through the Eq. (3-15), it is evident that the z_0 is a quadratic function of h_c as well. However these non-linear relationships appear to be incompatible with conventional wisdom on roughness parameterization where z_0 and d_0 are more often than not estimated as simple quotients of h_c for relatively short vegetation. Nevertheless this implies that the momentum absorption characteristics of tall forest canopies are intrinsically more complex than those of more typical agricultural canopies. Further this raises the question, whether the morphometric models thus far used to estimate normalized displacement height and roughness length, based on roughness element density should be modified to include the canopy height information as well.

The variance technique is an operational method for estimating H under unstable conditions using the measurements of standard deviation in air temperature (σ_T) and the standard deviation in the vertical component of wind velocity (σ_w). The method is shown to be robust even when the measurements are made in the roughness sub-layer. In this study we demonstrated how this technique can be used to estimate z_0 and d_0 when simultaneous measurements of eddy covariance fluxes (H and u^*) are also available. When using the variance method the estimated roughness parameters are very much sensitive to the chosen value of coefficient C_1 . Selection of proper value for C_1 is crucial as it mainly causes variance method to compute systematically higher or lower H . Hence the operational use of the variance method is constrained due to the non-availability of locally tuned C_1 values.

Finally it is important to mention that apart from the RSL effect discussed here, there are other limitations coupled with the flux-gradient approach due to various assumptions associated with MOST. Especially the key assumption that the measurements were conducted under steady state conditions in the fully adjusted layer above the RSL (requiring a sufficiently large homogeneous area to develop and maintain equilibrium) have been hardly fulfilled during the data collection. Hence the methods used here are strictly applicable to areas where the surface conditions are more homogeneous. Furthermore the true neutral conditions rarely occur and consequently those

observations represent only a minor fraction of the day. Nevertheless, these limitations can be combated to some extent by employing a data set which runs through a longer observation period with several levels of wind speed and temperature measurements.

4 Effect of spatial resolution on estimating surface albedo *

* **This chapter is based on**

Weligepolage, K., Gieske, A.S.M. and Su, Z., 2013. Effect of spatial resolution on estimating surface albedo: A case study in Speulderbos forest in The Netherlands. *Int. J. Appl. Earth Observation and Geoinformation*, 23, 18-28

Abstract

Land surface albedo is one of the most important parameters accountable for the planetary radiative energy budget. It is known that albedo varies in both space and time as a result of various natural processes and human interventions. Especially in forest ecosystems these variations are much more intense due to inherent canopy structural differences and anticipated seasonal changes. In such environments, estimation of spatially distributed surface albedo poses challenges in terms of capturing the spatial variability using a remotely sensed sensor with a finite field of view. This study investigated the stand level surface albedo variability of a patchwork forest in the central part of The Netherlands. The data used for the study included airborne and satellite imageries and tower-based solar radiation measurements acquired through a dedicated field campaign. The imageries were pre-processed and atmospherically corrected to obtain top of the canopy (TOC) reflectance. The TOC reflectance bands in the visible and near-infrared domain were integrated to estimate spatially distributed surface albedo while the tower-based radiation measurements in the solar-reflective region were used to obtain the temporal variation of surface albedo over a needleleaf forest canopy. The diurnal variation of surface albedo is consistent with the previous findings for needleleaf forest canopies. The spatial mean surface albedo values estimated from remote sensing data for needleleaf (pure Douglas fir), broadleaf (pure Beech) and mixed forest classes are 0.09, 0.13 and 0.11 respectively. Both visual characteristics and descriptive statistics indicate that with increased pixel size, the spatial variability of albedo progressively decreases. The semivariogram analysis was more insightful to perceive the nature and causes of albedo spatial variability in different forest classes in relation to sensor spatial resolution.

4.1 Introduction

Land surface albedo is defined as the reflected fraction of solar radiation to the down-welling irradiance incident upon Earth's surface. This spatially distributed surface variable mainly governs the radiative energy budget of the Earth's surface. Albedo mainly affects the solar energy absorption by the Earth's surface and consequently the fraction of available energy for various biophysical processes such as evapotranspiration and photosynthesis. The remaining fraction controls evaporation, snow melt and temperature related processes at the soil surface (Pinty et al., 2008). These processes eventually determine the partitioning of available energy to the fluxes of latent energy and sensible heat at the top of the vegetation canopy and the ground heat flux. Thus, land surface albedo is a key variable, fundamental to characterize the surface energy budget of the lower atmosphere which is an integral part of different land surface models operating at various spatial and temporal scales.

It is well-known that land surface albedo varies both spatially and temporally due to various natural events and anthropogenic activities. Especially in forest ecosystems these variations are much more prominent due to ecological and seasonal changes. For example the observed albedo values of snow-covered needleleaf forest are almost double the corresponding snow-free estimates (Davidson & Wang, 2004). Also the diurnal pattern of surface albedo of boreal conifer forests differs from snow-covered to snow-free period (Ni and Woodcock, 2000). Some other factors affecting the surface albedo of vegetative surfaces are listed as the surface anisotropy which is connected with the canopy structure and the atmospheric condition (Schaaf *et al.*, 2008). Therefore comprehensive information on spatial and temporal albedo variability is essential to understand the global energy budget and its implications on climate and vegetation dynamics (Davidson & Wang, 2004). While ground-based tower measurements support local and regional estimation of surface albedo at high temporal resolution, remote sensing is the only practical means of capturing the global heterogeneity of albedo and reflectance anisotropy (Liang, 2008).

At present, albedo and reflectance anisotropy products are available globally on regular basis from moderate spatial resolution sensors with spatial resolution from few hundred meters (e.g. TERRA/MODIS, ENVISAT/ MERIS) to few kilometers (e.g. PARASOL/POLDER and MSG/SEVIRI) and temporal frequencies of daily to hourly. Since at coarse spatial resolution the sensors average the radiometric signal over the pixels, much of the information is lost. However most of the natural surfaces are spatially heterogeneous at much lower scales than the spatial resolution of these sensors. Thus the currently available albedo products from moderate resolution sensors may

not be able to capture the inherent surface heterogeneity exhibited by these natural surfaces. While the point based albedo measurements can be used to capture the temporal variation of a homogeneous surface, but in order to characterize the spatial variability in heterogeneous surfaces the use of high spatial resolution remote sensing data is indispensable. In this context the complementary use of in-situ measurements and high spatial resolution remote sensing data will lead to accurate characterization of the spatial and temporal variability of surface albedo.

The temporal variation of forest surface albedo has been an extensively studied research topic focusing on different forest ecosystems (Ni and Woodcock, 2000). However the characterization of spatial variability of forest surface albedo has not been addressed adequately. Specially the influence of forest canopy structure and stand characteristics on the spatial variability of albedo is yet to be understood. On the other hand, with the advent of high spatial, spectral, and radiometric resolution sensors in satellite orbits, there is much scope for investigating the variability of the albedo of the earth's surface using remotely sensed data in the optical domain. Exploitation of such data from a variety of sensors and multiple platform heights is vital to improve the knowledge of spatial variability of albedo of various surface types in connection with sensor characteristics and pixel resolution.

The main question that prompted this study was: how do the spatial resolution and variation in stand structure affect the estimation of albedo by remote sensing in forest ecosystems? We investigated the canopy level surface albedo variability of a patchwork forest using very high and high spatial resolution remote sensing data in combination with tower-based solar radiation measurements. The specific objectives of the study are to (a) examine the diurnal variation of surface albedo of a needleleaf conifer forest stand using in-situ solar radiation measurements, (b) estimate spatially distributed surface albedo using atmospherically corrected multi-scale remote sensing data in visible and near-infrared domains, and (c) examine the effect of spatial resolution in discriminating albedo characteristics of three distinct forest classes by quantifying the spatial structure of forest classes using a variogram analysis.

4.2 Data

4.2.1 Imagery dataset

Airborne Hyperspectral Scanner (AHS)

AHS is an airborne imaging radiometer, developed by ArgonST (USA) and operated by the Spanish Institute for Aerospace Technology (INTA). It has 80 bands out of which 63 bands are in the solar-reflective region (0.4 to 2.5

microns), 7 bands in the mid infra red range (3 to 5 microns) and 10 bands in the thermal infra red region (8 to 13 microns) of the electromagnetic spectrum. The telescope design includes a so-called pfund assembly, defining a 2.5 milli-radian instantaneous field of view (IFOV) acting as a field stop, which is therefore unique for all bands, and redirects the radiation to a spectrometer placed above the telescope (Fernández-Renau, et al., 2005). Table 4-1 summarizes the AHS spectral configuration under different ports.

Table 4-1: AHS spectral information for Port 1 (0.43 – 1.03 μm) and the corresponding E_{SUN} values and weighting coefficients.

AHS Band No.	Central λ (μm)	E_{SUN} ($\text{W m}^{-2}\mu\text{m}^{-1}$)	w_b
1	0.455	1923.1	0.073
2	0.484	1886.8	0.072
3	0.513	1829.1	0.070
4	0.542	1774.3	0.068
5	0.571	1740.5	0.067
6	0.601	1689.2	0.065
7	0.630	1602.5	0.061
8	0.659	1510.0	0.058
9	0.689	1403.9	0.054
10	0.718	1324.1	0.051
11	0.746	1240.6	0.047
12	0.774	1152.4	0.044
13	0.804	1089.5	0.042
14	0.833	1014.9	0.039
15	0.862	952.5	0.036
16	0.891	894.5	0.034
17	0.918	842.9	0.032
18	0.948	806.4	0.031
19	0.975	767.2	0.029
20	1.004	726.0	0.028

For this analysis two nadir looking AHS images acquired on the 13th of June 2006 (DOY-164) at two different altitudes have been selected. These airborne images were acquired by the INTA airplane over Speulderbos area in parallel to the ground measurements of EAGLE 2006 field campaign. The nominal ground resolution of the image acquired by the low-altitude flight (975 m AGL) is 2.4 m whereas the ground sample distance of the image acquired by the high-altitude flight (2743 m AGL) is 6.9 m. The observation conditions of the two AHS images are summarized in Table 4-3. INTA has delivered, images pre-processed to Level 1b data, i.e. at-sensor radiance (units in $\text{Wcm}^{-2}\text{sr}^{-1}\text{nm}^{-1}$) together with Image Geometry Model (IGM) files

geo-referenced to UTM 31-WGS84) and scanning zenith and azimuth angles (SCA files) computed by PARGE for each scene.

ASTER image

The Advanced Space-borne Thermal Emission and Reflection Radiometer (ASTER) is an advanced multispectral imager that covers a wide spectral region with 14 bands from the visible to the thermal infrared with high spatial, spectral and radiometric resolution (Abrams, 2000). The images are acquired by 3 different telescopes with 3 different spatial resolutions 15 m in the visible and near-infrared (VNIR), 30 m in the shortwave infrared (SWIR) and 90 m in the thermal infrared (TIR). Table 4-2 summarizes the ASTER spectral band configuration in VNIR region of the spectrum. A Single ASTER image (Level-1B) acquired during the field campaign period on 8th of June 2006 (DOY-159) is selected for the study. The observation conditions of the ASTER image are summarized in Table 4-3.

Table 4-2: ASTER spectral information for Visible and Near-Infrared group (0.52 – 0.86 μm) and the corresponding E_{SUN} values and weighting coefficients.

ASTER Band No	Spectral range (μm)	E_{SUN} (W m ⁻² μm ⁻¹)	W_b
1	0.52 - 0.60	1846	0.408
2	0.63 - 0.69	1555	0.344
3	0.78 - 0.86	1120	0.248

Table 4-3: The observation conditions of air-borne and satellite imageries.

Image file No	Day of year	Time of acquisition (UTC)	Altitude A.M.S.L. (km)	True heading	Solar azimuth/elevation
AHS-P05BD	164	12:24	1.021	68°	201°/60°
AHS-P01AD	164	11:50	2.789	239°	185°/61°
ASTER-L1B	159	10:44	700 .000	-	203°/59°

4.2.2 Tower-based surface radiation measurements

Radiation measurements were made at the Speulderbos tower site using the CNR1 Net Radiometer (Kipp & Zonen) mounted at 35 m above the ground level. The instrument is a combination of 2 pyranometers (CM3) for measuring incoming (S_{\downarrow}) and reflected (S_{\uparrow}) Solar Radiation (0.3 - 3 μm) and, 2 pyrgeometers (CG3) for measuring incoming and outgoing Far Infrared radiation (5 - 50 μm). The instantaneous radiation measurements collected at two second intervals were stored as one minute averages using the CR23X data logger. The temporal coverage of radiation measurements is from DOY 158 to 174 in year 2006. As the instrument was mounted about 3 m above

the canopy surface the input to the downward-facing sensor is the spatial average of an area of 30 m radius below the sensor.

4.3 Theory and Methods

4.3.1 Tower-based surface albedo estimation

In order to determine albedo, the incoming (S_{\downarrow}) and reflected (S_{\uparrow}) solar radiation measured with two CM3s were used. Usually measurement pairs with very low S_{\downarrow} ($<15 \text{ Wm}^{-2}$) were excluded as those values produce unrealistic albedo estimates. Also the measurements made at low solar elevations (lower than 10 degrees above the horizon) were excluded since those measurements yield unreliable results due to deviations in the directional response of the CM3s.

4.3.2 Image pre-processing

Geometric and radiometric calibrations

AHS L1b data delivered by INTA team consist of at-sensor radiance ($\text{nWcm}^{-2}\text{sr}^{-1}\text{nm}^{-1}$) for the VIS/NIR/SWIR bands converted to Band Sequential (BSQ) format after laboratory calibrations. For the present analysis we selected a spectral subset covering visible and near-infrared regions of the spectrum (0.43 – 1.03 μm) where AHS bands 1 to 20 were included. The images were georeferenced using ENVI georeference from input geometry (georeference from IGM) functionality. For geocoding the AHS image acquired by the low-altitude flight (GSD -2.4 m), the pixel size was selected as 2.5 m. Similarly the AHS image from the high-altitude flight (GSD - 6.9 m) was geocoded with a pixel size of 7.5 m. The importation of ASTER Level 1B data using the import functionality of ILWIS resulted an object collection containing 14 bands in 3 sensor groups (VNIR, SWIR and TIR) with 3 separate georeference files (single georeference for each sensor group) to the geometry of the UTM projection (zone 31) and WGS 1984 Datum. Also during the importation the sensor calibrated DN values are converted to at-sensor radiance ($\text{Wm}^{-2}\text{sr}^{-1}\mu\text{m}^{-1}$) using the unit conversion coefficients of the HDF file. Once the above calibrations were completed the resultant images with at-sensor radiance values were further processed to retrieve top of the canopy surface reflectance. The procedure used in this study to convert at-sensor radiance to top of the canopy reflectance is described next.

Atmospheric corrections and estimation of surface reflectance

In this step planetary reflectance (r_p) was determined using the following expression.

$$r_p = \frac{L_0 \pi d^2}{E_{SUN} \cos \theta_s} \quad (4-1)$$

where L_0 is the at-sensor radiance ($\text{Wm}^{-2}\text{sr}^{-1}\mu\text{m}^{-1}$), d is the Earth-Sun distance (AU), E_{SUN} is the band-dependent mean solar exo-atmospheric irradiance ($\text{Wm}^{-2}\mu\text{m}^{-1}$), and θ_s is the solar zenith angle. The value of d and θ_s were computed using the date and time of the acquisition of the image and the latitude and longitude of the location.

Using the four-stream land-atmosphere radiative transfer theory (Verhoef, 1985, 1998), for a homogeneous Lambertian surface, the surface reflectance (r_0) is expressed as:

$$r_0 = \frac{r_p - \rho_{so}}{(\tau_{ss} + \tau_{sd})(\tau_{do} + \tau_{oo}) + \rho_{dd}(r_p - \rho_{so})} \quad (4-2)$$

where ρ_{so} = atmospheric bidirectional reflectance, ρ_{dd} = spherical albedo of the atmosphere, τ_{ss} = direct atmospheric transmittance in the direction of the sun, τ_{oo} = direct atmospheric transmittance in the direction of viewing, τ_{sd} = diffuse atmospheric transmittance for solar incidence, τ_{do} = directional atmospheric transmittance for diffuse incidence.

The above described six parameters are termed as effective atmospheric parameters and in order to convert planetary reflectance to surface reflectance, these six parameters have to be determined in advance. The effective atmospheric parameters are constant for a given combination of geometric configuration and atmospheric state. However these are wavelength dependent hence needs to be determined at each wavelength. This can be accomplished using a suitable atmospheric radiative transfer model in the solar-reflective region (400 – 2500 nm). In this study we used MODTRAN4 (Berk et al., 2000) atmospheric radiative transfer code to determine the six spectra of effective atmospheric parameters. The approach used here is the MODTRAN Interrogation Technique (MIT) developed by Verhoef and Bach (2003) based on MODTRAN4 model. The technique requires three steps to be carried out. First the input file (tape 5) for model simulation was prepared for the selected Sun- satellite geometric configuration and atmospheric state. Table 4-4 describes the main input parameters used in preparing the tape 5 for selected sensors. Using each input file, model simulations were carried out for three spectrally flat surface albedo values of 0%, 50% and 100%. Finally the main outputs obtained from MODTRAN4 simulations, viz., PATH (total path radiance), GSUN (radiance

contribution due to ground reflected sunlight), GTOT (total ground-reflected radiance contribution) and the extraterrestrial solar spectral irradiance were used to determine the six spectra of effective atmospheric parameters. Once the six spectra of atmospheric parameters were determined, the corresponding band averaged values were estimated using Eq. (4-3), where spectral values were integrated and normalized over the wavelength interval using the spectral response function of each sensor band.

$$\bar{X} = \frac{\int X(\lambda)f(\lambda)d\lambda}{\int f(\lambda)d\lambda} \quad (4-3)$$

Here $X(\lambda)$ represents any spectral parameter, $f(\lambda)$ is the sensor response function and \bar{X} is the corresponding band averaged value.

Using the following expression (Eq. (4-4)) which is specifically valid for a finite banded sensor, band by band corrections were applied to convert planetary reflectance to narrowband surface reflectance values.

$$r_0 = \frac{r_p - \bar{\rho}_{so}}{(\bar{\tau}_{ss} + \bar{\tau}_{sd})(\bar{\tau}_{do} + \bar{\tau}_{oo}) + \bar{\rho}_{dd}(r_p - \bar{\rho}_{so})} \quad (4-4)$$

Here the over bar terms represent the corresponding band specific values of the effective atmospheric parameters.

Table 4-4: Main input parameters used for MODTRAN4 - tape 5 card

Parameter/Option	AHS-P05BD	AHS-P01AD	ASTER
Atmospheric profile	Mid-lat. summer	Mid-lat. summer	Mid-lat summer
Aerosol extinction	Rural	Rural	Rural
Visibility	23 km	23 km	23 km
Sensor altitude	1.021 km	2.789 km	700 km
Solar zenith angle	30.45 deg.	29.01 deg.	31.1 deg.
Sun-sensor azimuth	133 deg.	54 deg.	23 deg.
Water vapor scaling	1.8	1.8	1.0
Ozone scaling	1.2	1.2	1.1

4.3.3 Estimation of broadband surface albedo

In this step, broadband surface albedo (α) is calculated from multiband satellite data by integrating band reflectance across the visible and near-infrared spectrum. The weighted relationship given in Eq. (4-5) is used here for the integration of surface reflectance values.

$$\alpha = \sum_{b=1}^n w_b \cdot r_{0,b} \quad (4-5)$$

where w_b is the weighting coefficient for the particular band and is estimated from the band-dependent E_{SUN}

$$w_b = \frac{E_{SUN,b}}{\sum_{b=1}^n E_{SUN,b}} \quad (4-6)$$

The E_{SUN} values given in Sobrino et al. (2008) were used for AHS bands 1 to 20 (see Table 4-1) and corresponding E_{SUN} values used for ASTER visible and near infrared bands are listed in Table 4-2.

4.3.4 Forest species classification using AHS image

We performed a multi-spectral supervised image classification using the Gaussian Maximum Likelihood classification method. Three atmospherically corrected spectral bands from AHS low-altitude image were employed for feature class transformation. During the training phase three 'generic' forest classes were defined viz. needleleaf forest (pure Douglas fir stands), broadleaf forest (pure Beech stands) and mixed forest (Pine, Oak and Hemlock) accommodating different species in the study area. The non-vegetated patches were assigned the Bare-soil class. The required knowledge on the 'ground truth' was acquired by conducting a GPS survey in the study area with the assistance of 1:25,000 topographical maps. For the classification of above chosen forest types, we found that the Gaussian Maximum Likelihood classifier worked best. The final classification output was improved by applying a majority filter. As a result of the supervised classification each pixel of the image was ascribed to one of 4 classes as shown in Figure 4-1.

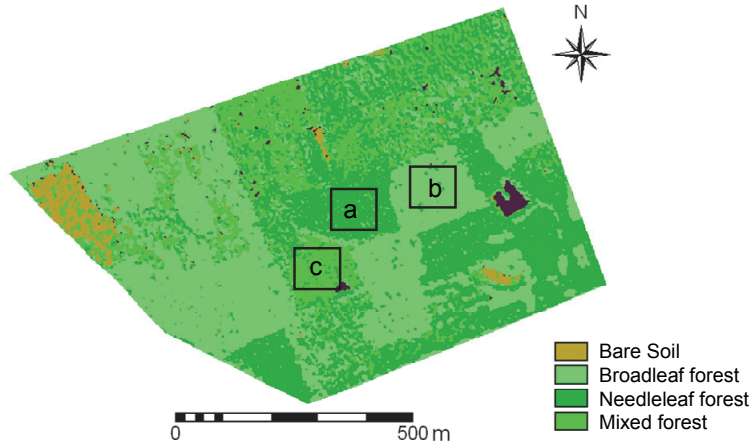


Figure 4-1: Land cover distribution of the study area obtained by the supervised classification using AHS low-altitude image data. The areas denoted by (a), (b) and (c) were used to calculate experimental semivariograms for needleleaf, broadleaf and mixed forest classes respectively.

4.3.5 Semivariograms

Remotely sensed surface albedo is a continuous variable in the space domain, which depends on the spatial resolution of the particular sensor. In spatial statistics, such a spatially continuous variable is termed as a regionalized variable (Van der Meer, 2012). The spatial variability of a given data set can be graphically represented by a semivariogram. The semi-variance $\gamma(h)$ is defined as half the normalized squared difference in spatial variable between all observations at a given lag h from a central point (Eq. (4-7)):

$$\gamma(h) = \frac{1}{2N(h)} \sum_{i=1}^{N(h)} [Z(x_i) - Z(x_i + h)]^2 \quad (4-7)$$

where $N(h)$ the number of point pairs with lag h , $Z(x_i)$ is the value of the variable at position x_i and $Z(x_i + h)$ is the value of the variable at distance h from x_i . Since the number of point pairs available for computing $\gamma(h)$ goes down with increasing h , the reliability of $\gamma(h)$ drops for large lag distance. The usual rule of thumb is to limit the maximum lag distance used to estimate $\gamma(h)$ to a value between one-third and one-fifth of the total distance.

A plot of semi-variance versus lag distance can be fitted with a theoretical model describing the semi-variance characteristics of the images with a

unique set of parameters. The parameters to describe a semivariogram model are the range (a), sill (c) and nugget variance (c_0). The nugget is the positive intercept of the semivariogram and represents the discontinuity at the origin due to small scale variation. The range is the lag distance at which the semivariogram reaches the sill value. The range indicates the maximum lag distance to which the spatial correlation exists. The value ($c_0 + c$) indicates the total sill or the maximum variance. For a particular spatial phenomenon, the range of the semivariogram is a measure of spatial dependency whilst the sill reflects the amount of variability (Cohen et al., 1990).

In this study we used the spherical and exponential models as since those are the most commonly used theoretical semivariogram models for natural system studies (McBratney & Webster, 1981; Webster & Nortcliff, 1984).

The spherical model with above notations is expressed as:

$$\gamma(h) = c_0 + c \left(\frac{3h}{2a} - \frac{h^3}{2a^3} \right) \quad \text{when } h \leq a \quad (4-8)$$

$$\gamma(h) = c_0 + c \quad \text{when } h > a \quad (4-9)$$

The exponential model using the same notations is given as:

$$\gamma(h) = c_0 + c \left[1 - \exp\left(\frac{-3h}{a}\right) \right] \quad (4-10)$$

4.3.6 Characterizing forests spatial structure

In section 4.3.4 we defined three different forest classes in the study area. We investigated the spatial structure of each forest class using a semivariogram analysis. The state-variable used for the semivariogram analysis is the surface albedo as calculated with Eq. (4-5). We used the albedo estimates of AHS low-altitude image since this has the finest spatial resolution of 2.5 m. We selected three image subsets, one for each forest class (see Figure 4-1) to calculate experimental semivariograms. Here we used the matrix method to generate the experimental semivariogram where a single semivariogram is calculated for all rows (horizontal semivariogram) and a single semivariogram is calculated for all columns (vertical semivariogram) of the image subset. Then the experimental semivariogram was calculated by averaging the two unidirectional semivariograms. Finally the generated experimental semivariograms were fitted using the spherical and exponential models described in Eqs. (4-8), (4-9) and (4-10). The

values for nugget, range and sill were input to the models and interactively modified to achieve a 'best-fit' to the observations.

4.4 Results

4.4.1 Outputs of MODTRAN interrogation technique

The result of the MODTRAN interrogation technique illustrating the spectra of six effective atmospheric parameters for the wavelength range from 400nm to 2500nm is shown in Figure 4-2. The main input parameters used for the MODTRAN4 simulations are listed in Table 4-4. A comparison is made using Figure 4-2 (a) and (b) to differentiate the six spectra for the respective Sun-sensor geometries of AHS low-altitude flight and the ASTER sensor. In both charts, clear difference can be observed between the spectra of direct transmittance (τ_{ss} and τ_{oo}) and the diffuse transmittance (τ_{sd} and τ_{do}). Also the increased scattering at short wavelengths and the absorption bands in the near and mid infrared regions is clearly evident from both the panels. However a clear difference in magnitude is observable in upper and lower panels for spectra of τ_{ss} , τ_{oo} and τ_{sd} between the wavelengths 400 to 700nm. Furthermore Figure 4-3 illustrates the band averaged values of six effective atmospheric parameters for AHS band 1 to 20 and ASTER band 1 to 9 in (a) and (b) respectively.

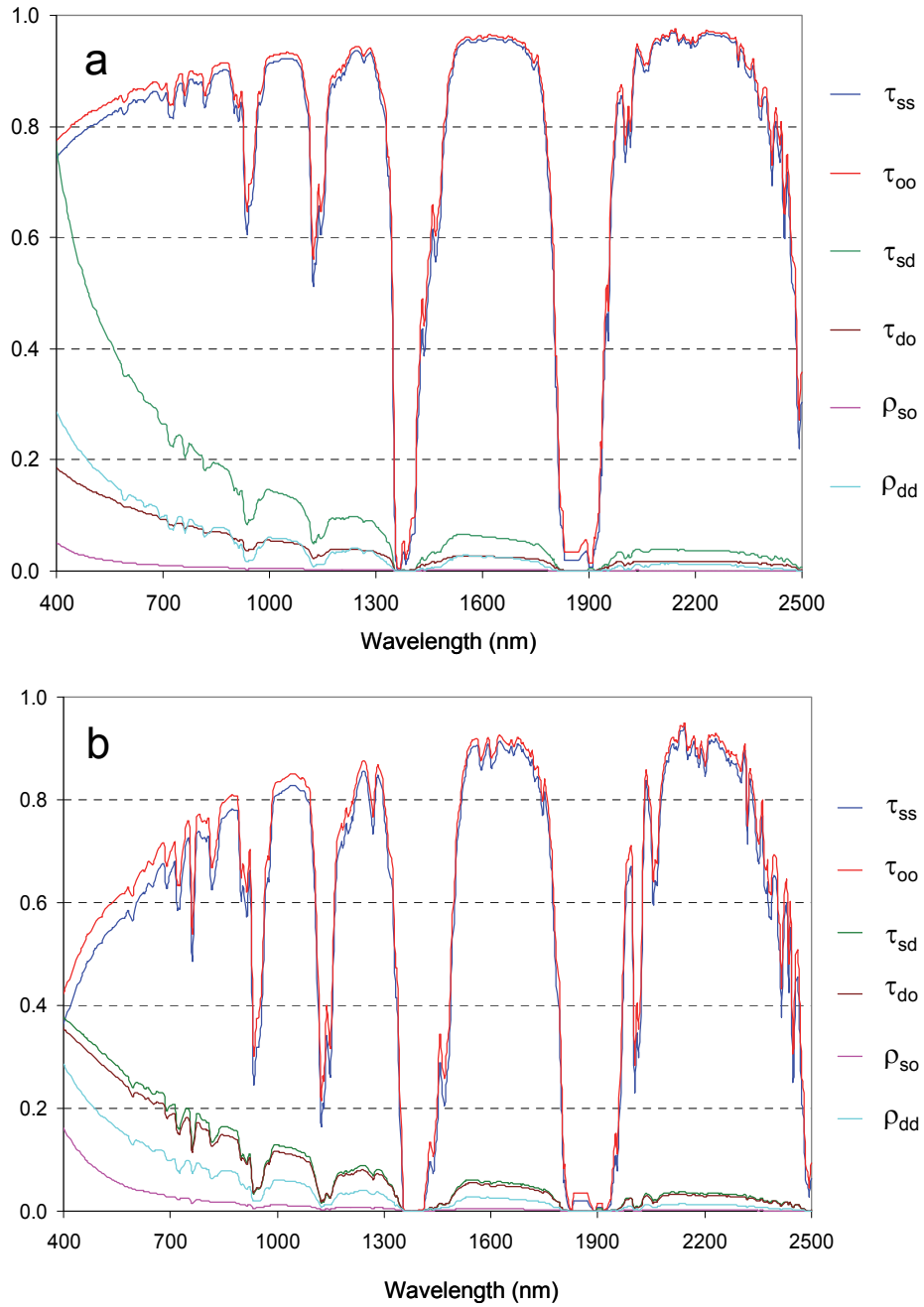


Figure 4-2: Spectra of six effective atmospheric parameters derived using MIT for different Sun-sensor geometries for (a) AHS low-altitude flight and (b) ASTER image.

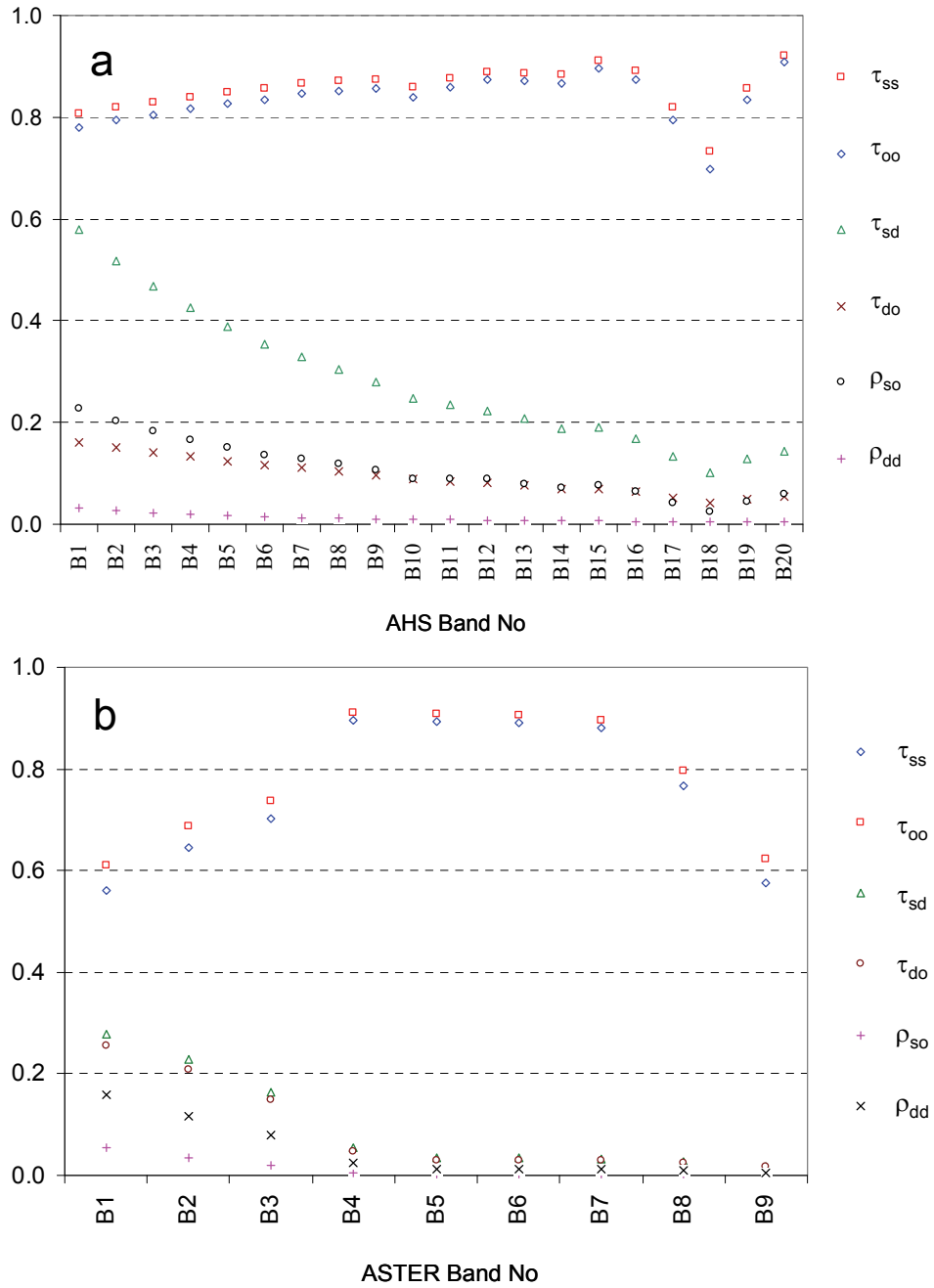


Figure 4-3: Band averaged values of six effective atmospheric parameters for (a) AHS band 1 to 20 and (b) ASTER band 1 to 9

4.4.2 Tower-based surface albedo results

Figure 4-4-a shows the temporal variation of surface albedo estimated from radiation measurements at the Douglas fir stand from the DOY 159 to 164. The diurnal pattern (Figure 4-4-b) exhibits nearly a 'bowl' shape with the highest albedo values occurring early in the morning and late in the afternoon. Also a strong asymmetry in half-hourly mean albedo values around the local solar noon is evident from the diurnal pattern. It further shows that the minimum albedo value is occurring before the solar noon (around 10:00 hrs. local time) for most of the days. Moreover the daily mean albedo estimated by integrating the one minute averages of tower-based albedo values between 6.00 and 18.00 hours indicates that, the daily mean albedo value exceeds the instantaneous albedo value observed around local solar noon by about 10 to 15 percent.

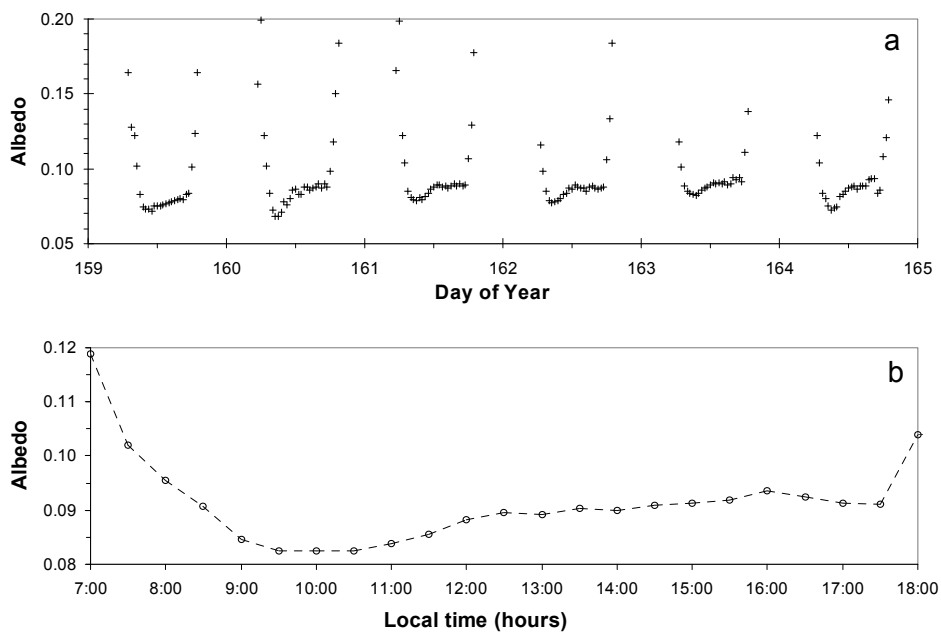


Figure 4-4: (a) Temporal distribution of surface albedo estimated with tower-based measurements over the needleleaf forest from DOY-159 to 165. (b) Diurnal variation of half hourly mean albedo estimated for the same period.

4.4.3 Spatial variability in canopy surface albedo estimated with image data

Figure 4-5 shows the spatially distributed albedo estimated using AHS low-altitude, AHS high-altitude and ASTER images respectively. Also shown in the figures are the corresponding histograms against each albedo image. Visual

characteristics of albedo maps show that, with the increased pixel size, the spatial variability of the albedo progressively decreases from AHS low-altitude image to ASTER image. This effect could be quantitatively analyzed by comparing the histograms of albedo distribution for three sensors. The histograms indicate that both the low and high-altitude AHS sensors have detected much lower albedo values (0.05 - 0.075) whereas with the ASTER sensor the lowest albedo values detected were above 0.075. However the histograms indicate that the disparity among the three sensors is relatively minor in detecting higher albedo values. Moreover the spatial distribution of AHS low-altitude image exhibits a near-normal (Gaussian) shape while the equivalents with AHS high-altitude and ASTER images show a clear bi-modal pattern.

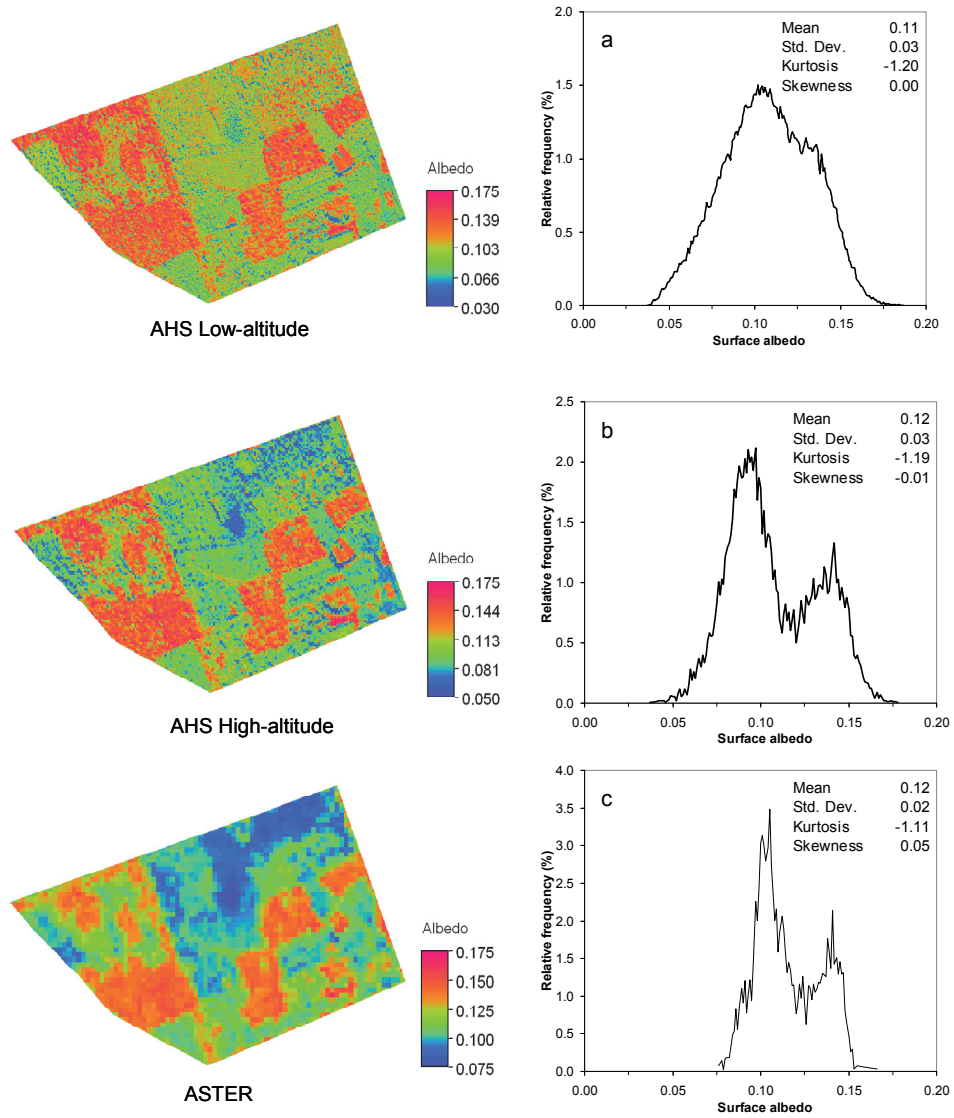


Figure 4-5: Albedo spatial variability of the study area estimated with image data. Histograms and descriptive statistics for albedo distribution at different spatial resolutions. (a) 2.5 m AHS low-altitude; (b) 7.5 m AHS high-altitude (c) 15m ASTER

4.5 Discussion

4.5.1 Analyses of temporal variability of tower-based albedo

The increased albedo values observed during the early morning hours and late in the afternoon are predominantly due to the volume scattering. During these hours the low solar elevation angles give rise to increased path-length through the canopy, which in turn increases the multiple scattering particularly in the near-infrared region. The asymmetry in the diurnal pattern of albedo has been investigated by Minnis et al., (1997) and they have shown that wind speed, dew and frost may influence the observed morning /afternoon albedo differences. Furthermore, technical faults during measurements for instance small tilt in the sensor or measurement area interfered by the tower shadow during low solar elevations can cause such diurnal variations.

4.5.2 Analysis of forest class-sensor dependency

To analyze the forest class-sensor dependency of albedo we computed the within-class albedo variations of each image for the forest classes defined above. The histograms in Figure 4-6 a, b and c illustrate the within-class spatial distribution of albedo obtained with AHS low-altitude, AHS high-altitude and ASTER images respectively. Also in Figure 4-6 the dotted line represent the histograms of needleleaf forest while the thin and thick solid lines represent histograms of mixed and broadleaf forest respectively. Several observations can be made from the histograms in Figure 4-6. In general the albedo range progressively narrows from Figure 4-6-a to Figure 4-6-c. In Figure 4-6-a the albedo histograms corresponding to different classes indicate unique spatial distributions with distinctive peaks. However in both Figure 4-6-b and Figure 4-6-c the histograms corresponding to needleleaf and mixed forest are not clearly distinguishable from each other. In all three cases clear distinction can be made between the albedo distribution of broadleaf forest and other two categories. Furthermore the near-normal distribution observed in Figure 4-6-a for all three histograms changes to right-skewed shape for needleleaf and mixed forest and to a left-skewed distribution for broadleaf forest in Figure 4-6-c.

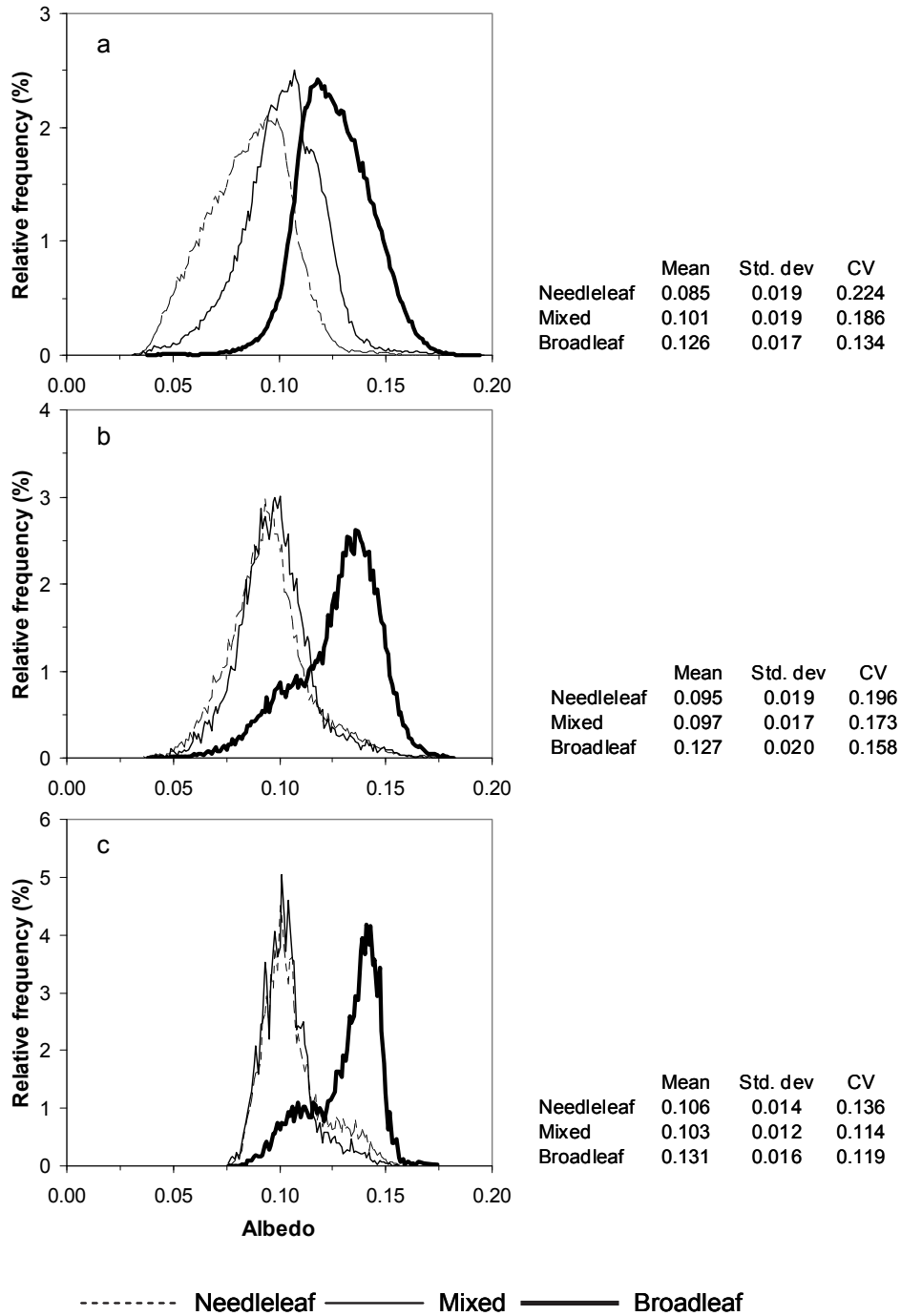


Figure 4-6: Albedo spatial distribution of different forest classes obtained using (a) AHS low-altitude image; (b) AHS high-altitude image; (c) ASTER image.

4.5.3 Analysis of spatial structure and effect of pixel size

To comprehend the observed albedo spatial variability in different images, we further investigated the spatial structure and within-class spatial variability by a semivariogram analysis. Figure 4-7 a, b and c show the experimental semivariograms obtained for three forest classes fitted with a spherical and exponential models. Also Figure 4-7 lists the semivariogram model parameters of three forest classes. The characteristics of these semivariogram models provide an insight to the spatial structures within the forest class. The nugget values show that needleleaf forest has the highest random variability whereas the sill values indicate that the observed spatial variability in broadleaf class is much higher compared to needleleaf and mixed classes which show much similar spatial variability. However the most important information with respect to spatial resolution can be obtained from the range values. The mean ranges derived from the two semivariogram models indicate that needleleaf and mixed forest classes have smaller ranges (6.25 m and 6.75 m respectively) than the broadleaf class (15.25 m) (see Figure 4-7).

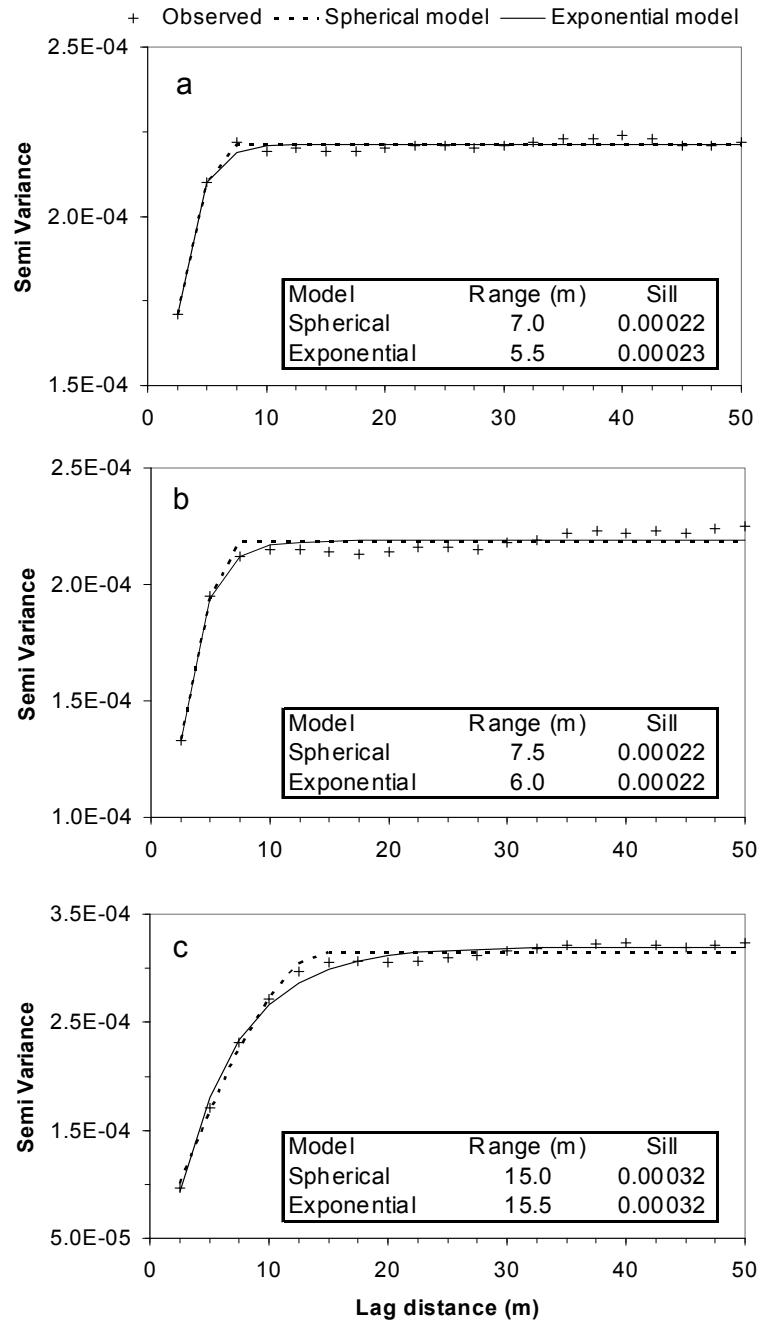


Figure 4-7: Experimental semivariograms obtained for (a) needleleaf forest; (b) Mixed forest; (c) broadleaf forest classes fitted with spherical and exponential models. The range and sill values of semivariogram models are listed for each forest class.

According to sampling theorem (McGrew & Monroe, 2000), generally a pixel size larger than half of the range may lose spatial information due to averaging. This implies that the spatial variability of all three classes can be best captured by a sensor with a spatial resolution about 3 m. In this case only the AHS low-altitude sensor was capable of differentiating the spatial heterogeneity of all three forest classes while the AHS high-altitude sensor probably would detect the spatial variability of broadleaf class to some extent. As also evident from the histograms (Figure 4-6) out of the three sensors, ASTER being the one with the largest pixel size suppresses spatial variability in all three forest classes due to averaging. Given the spatial resolution of different sensors used in this analysis and the range values derived for different forest classes, the largest discrepancy in surface albedo variability would occur in the ASTER estimates of needleleaf forest class.

In Figure 4-8 we graphically compared the spatially averaged albedo of needleleaf forest, estimated with different images at sensor overpass times against the diurnal variation of tower-based albedo. Also the statistics computed for albedo spatial distribution at sensor overpass time are presented in Table 4-5. Figure 4-8 shows a large discrepancy between the tower observations and the average albedo of needleleaf forest estimated by ASTER image. However the estimated spatial averages of both AHS low and high-altitude images are in agreement with tower-based albedo estimates as observed from Figure 4-8. The statistics given in Table 4-5 reveal that the difference between the average albedo of AHS low-altitude image and the parallel tower-based value is 0.003 whereas the corresponding discrepancy for AHS high-altitude image is 0.008. These absolute differences in albedo estimates indicate that based on the tower estimated albedo values, the relative error in remotely sensed albedo estimates are about 3% and 9% for AHS low-altitude and AHS high-altitude images respectively. Nevertheless the observed absolute difference (0.03) between the tower-based albedo and the average estimate of ASTER image indicates the relative error is almost 40%.

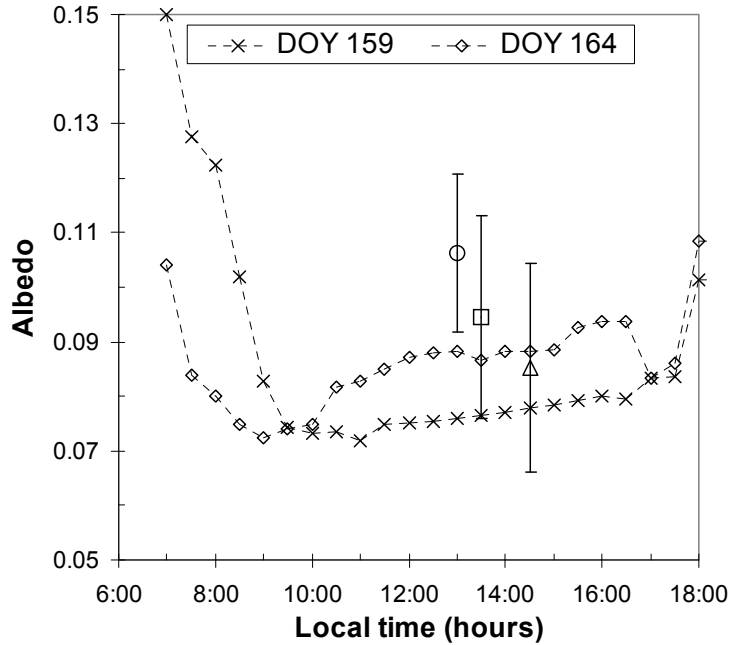


Figure 4-8: Comparison of spatially averaged albedo of needleleaf forest, estimated with different images against the half hourly averages of tower-based albedo estimated for sensor overpass days. The symbols open circle, square and the triangle denote ASTER, AHS high-altitude and AHS low-altitude based spatial averages respectively. The error bars denote the standard deviations.

Table 4-5: Comparison of spatially average albedo in needleleaf forest versus tower-derived albedo estimates

	Image Albedo Average	Std. dev.	Tower albedo at over- pass	Difference	% Difference.
AHS Low-altitude	0.085	0.019	0.088	-0.003	-3.4%
AHS High-altitude	0.095	0.019	0.087	0.008	9.2%
ASTER	0.106	0.014	0.076	0.030	39.5%

4.6 Conclusions

In this chapter we investigate the canopy level surface albedo variability of a patchwork forest using a combination of very high to high spatial resolution remote sensing imageries and tower-based solar radiation measurements. The diurnal variation of surface albedo is consistent with the previous findings for needleleaf forest canopies. However the asymmetric diurnal pattern around solar noon observed in this study is not the typical form reported in

previous work on similar landscapes. The observed local minimum in the diurnal albedo variation (between 9 and 11 hrs local time) is more likely caused by the shadow of the measurement tower when the sun is in the east at a relatively low elevation. However our explanation is not conclusive since the local time of occurrence of this depression differs noticeably between two consecutive days. On the other hand this artifact appears to be camouflaged on a cloudy day (e.g. DOY 159) when the observed diurnal pattern is rather flat due to the increasing ratio of diffuse to direct solar radiation.

The spatial mean surface albedo values estimated from remote sensing data for needleleaf (pure Douglas fir), broadleaf (pure Beech) and mixed forest classes are 0.09, 0.13 and 0.11 respectively. These values are consistent with prescribed albedo values for similar forest types. Histograms of surface albedo distributions and descriptive statistics indicate that with increasing pixel size, the spatial variability of the albedo progressively decreases from AHS low-altitude image to ASTER image. Furthermore it is evident from the albedo histograms that the spatial distribution changes from a near-normal pattern to a bi-modal shape when the pixel size increases. An analysis of forest class dependent albedo spatial variability revealed that with increased pixel size, the spatial variability of individual forest classes decreases however in a dissimilar fashion. It appears that, the albedo histograms (in all three forest classes) transform from near-normal distribution to either right-skewed or left-skewed pattern as a result of pixel size degradation. At a pixel size of 2.5 m the AHS low-altitude image discriminates the albedo spatial variability between needleleaf class and mixed forest class whereas the other two images fail to distinguish between them. The degradation of spatial resolution has multiple effects on the total scene albedo variability which eventually modifies the observed spatial distribution from near-normal to bi-modal character.

The above results are consistent with conventional wisdom on the effects of spatial resolution on surface albedo. However the semivariogram analysis was more insightful to reveal the nature and causes of spatial variability observed in remotely sensed data of different forest classes as they relate to sensor characteristics. The parameters of fitted semivariogram models provide indicators to quantify the spatial structure within the forest ecosystems classes. The range estimates differ between different forest classes (particularly between the needleleaf and broadleaf forest) and appear to be related to the dominant object in the pixel. In the needleleaf forest class the range is roughly equal to the tree crown diameter as also verified from field observations. However for the remaining forest classes, such a relationship is not obvious and there appears to be a different spatial structure observed with the selected spatial resolution. More importantly the

range values corresponding to each forest class indicate the upper limit of the pixel size to capture the albedo spatial variability.

In this analysis when estimating top of the canopy reflectance from remote sensing data, we made necessary corrections for atmospheric effects. However due to the lack of consideration of bidirectional reflectance distribution function (BRDF) and the adjacency effects, the estimation accuracy of top of the canopy reflectance might have degraded. The advantage of using the present data set is that the images are near-nadir (the maximum view zenith angle for AHS low-altitude image is 15 deg.) hence the effect of BRDF corrections would be minor. Albeit the increased multiple scattering in the near-infrared bands suggest that adjacency effects may be significant, the very good agreement between the tower-based albedo estimates and the spatial mean albedo values estimated from airborne imageries for the needleleaf forest class is noticeable.

Finally it is worthwhile to highlight few implications of this study in the application of remote sensing based surface energy balance algorithms to estimate daily actual evapotranspiration. More often than not, remote sensing based surface energy balance algorithms utilize land surface albedo estimate made at one solar zenith angle from a polar-orbiting satellite to estimate net radiation. Furthermore such schemes deduce daily mean surface albedo using estimated instantaneous surface albedo in order to estimate daily net radiation. Therefore the procedure used by the energy balance algorithms to estimate daily net radiation is susceptible to errors introduced in retrieving instantaneous albedo from satellite images as well as in converting instantaneous albedo to the daily mean albedo. Based on the tower-based albedo measurements we have shown that the error in estimating surface albedo using airborne imageries is within $\pm 10\%$ whereas the corresponding error for satellite images is around $\pm 40\%$. Since the albedo measurements in this location are around 0.09, the corresponding errors in daily net radiation estimate are about 3 Wm^{-2} and 12 Wm^{-2} for airborne and space-borne imageries respectively. These results suggest that the slight difference in remotely sensed surface albedo estimates do not translate into significantly high errors in latent heat fluxes or daily evapotranspiration. Furthermore our computations show that often the daily mean albedo exceeds the instantaneous albedo observed around local solar noon by about 15%. This result is fairly consistent with the rule of thumb quite often used by the remote sensing energy balance models to estimate daily mean albedo by multiplying the instantaneous albedo value with a constant around 1.1.

5 Retrieving directional temperature using multiplatform thermal data

Abstract

In this chapter theoretical basis for directional LST estimation from top of the atmosphere radiance measurements is presented along with a spatio-temporal analysis of remotely sensed LST and concurrently carried out ground-based radiation as well as contact temperature measurements in a Douglas fir forest. For the analysis we used remotely sensed TIR data from Airborne Hyperspectral Scanner to estimate spatially distributed LST of forested area. The AHS sensor, with 10 thermal bands covering the range between 8 and 13 μ m of the electromagnetic spectrum is an example of the new generation of airborne sensors with multispectral thermal infrared capabilities. The data acquired from the AHS sensors provided the opportunity to retrieve the directional LST of the forest canopy with a very high spatial resolution for both nadir and oblique view angles. Also the concurrent tower-based temperature measurements provided limited ground truth for a spatio-temporal analysis of surface temperature in an area covered with Douglas fir trees. The method adopted here for concurrent determination of LST and LSE is the widely-used TES algorithm together with the MODTRAN4 preprocessor for calculating the required atmospheric contributions. The AHS derived LST values show that the difference between the spatially averaged temperature of the AOI from Nadir image and off-nadir image is subtle. Furthermore the AHS derived average temperature values are generally in good agreement with the tower based component temperature measured at 24 m level whereas the component temperatures (trunk) measured at 17 m are consistently higher. It may be noted that in comparison with off-nadir radiometric temperature the TES method provides average LST with RMSE around 1.9K while the corresponding value with respect to component temperature measured at 24 m is around 1.4 K.

5.1 Introduction

Land Surface Temperature (LST) is a key parameter which plays an important role in the land-atmosphere interaction process. The LST retrieved from thermal infrared (TIR) data has many applications in studying surface energy and water balance modeling as required by climate variability and weather prediction models. Also LST can be used to quantify actual evapotranspiration which is an important component of the hydrological cycle. Furthermore, various applications for instance mineral mapping, resource exploration, coal-fire detection, vegetation monitoring etc. rely on the knowledge of LST. Acquisition of TIR data in order to estimate LST at regional to global scale is only feasible using remote sensing techniques. Consequently the Earth observing remote sensing community has shown a keen interest in developing various algorithms to retrieve LST from remote sensing data targeting regional to global scale applications. Besides with the considerable progress made in developing technologically advanced sensor/platforms in the TIR domain (8-14 μm) during the past few decades, an array of EO data is available to retrieve LST on regional to global scale.

When LST is measured using a TIR radiometer at the Earth's surface the corresponding temperature is considered as Earth's skin temperature. Nevertheless defining the the skin temperature of land surface is a bit complicated because it is hard to define the surface unambiguously. In order to define LST explicitly the surface needs to be homogeneous and isothermal. Since, natural land surfaces consist of various materials with different geometries and surface properties these are neither homogenous nor isothermal. In this situation surface temperature cannot be unambiguously defined. Consequently estimation of LST is not a straightforward procedure (Qin and Karnieli 1999). In TIR remote sensing, the surface heterogeneity problem with regard to LST is circumvented by defining a 'surface radiometric temperature' related to the instantaneous field-of-view of the TIR sensor (Prata et al., 1995; Dash et al., 2002).

A space-borne radiometer measures the at-sensor radiance (land-leaving radiance modified by the atmospheric effects) in different TIR channels. The at-sensor brightness temperature for the TIR channels can be computed without much difficulty using at-sensor radiance by inverting the Planck's function. However if one needs to compute the LST from at-sensor radiance the atmospheric effects have to be removed first to obtain at-surface radiance. Further the knowledge of surface emissivity is required to separate the reflected long wave component. For accurate estimation of LST for a surface without a-priori knowledge of emissivity a radiometer with multispectral thermal bands and simultaneously observed atmospheric data are needed.

The angular dependence of emitted radiance as observed from a thermal radiometer mounted over a vegetative canopy has been investigated by various scientists using directional TIR measurements (Kimes et al., 1980; Balick and Hutchinson, 1986). It has been observed that the remotely sensed temperature of a plant canopy depends on the viewing perspective. This anisotropy of LST can be partly ascribed to the differential illumination/heating of canopy components (leaves, branches, stem, undergrowth, soil) causing surface temperature variations among the component. Also LST differences could be observed in the TIR radiometer if the sensor view direction changes from nadir to off-nadir. Usually, the nadir view radiometer may see more of the bottom layers of the canopy including the ground. With an off-nadir view the same radiometer sees only the illuminated upper canopy. Even at night, a vegetation canopy may show evidence of some anisotropy of LST because of differential cooling rates between the less exposed bottom layers of the canopy surface and the thoroughly ventilated upper canopy surface.

In this chapter we present a theoretical basis of LST estimation from at-sensor or top of the atmosphere radiance measurements along with a spatio-temporal analysis of remotely sensed LST and concurrently carried out ground-based radiation as well as contact temperature measurements in a Douglas fir forest. The image data for the analysis come from the EAGLE2006 field campaign where airborne images acquired at two different altitudes having both nadir and oblique view angles were collected over the forest. The ground-based data consist of radiative temperature measurements carried out from top of the tower using various instrumentation and surface contact temperature measurements of different canopy components using the negative temperature coefficient (NTC) sensors attached to them at different levels. The atmospheric correction procedure adopted to extract atmospheric parameters, the temperature emissivity separation (TES) algorithm employed to retrieve LST and Land Surface Emissivity (LSE), are also presented in the next section. An analysis is presented by comparing and contrasting the LST results as obtained from airborne thermal remote sensing images and tower-based directional radiometric temperature observations. Also the directional effect of LST is explored using the temperature differences of nadir view and off-nadir view images with respect to vegetation density.

5.2 Extraction of atmospheric parameters

Using the four-stream land-atmosphere radiative transfer theory (Verhoef, 1985, 1998), for a homogeneous Lambertian surface of emissivity ε , the top of the atmosphere (TOA) radiance in the thermal domain (8000- 12000 nm) can be given by the following simplified expression as

$$L_0(t) = L_a(t) + [(1 - \varepsilon)L_a(b) + \varepsilon L_s] \tau_{oo} \quad (5-1)$$

where L_a is the thermal self-emitted path radiance of the atmosphere and (b) and (t) indicate the bottom and the top of the atmosphere respectively, L_s is the black body radiance of the surface and τ_{oo} is the atmospheric transmittance. It can be seen from equation (5-1) that L_s and ε can be determined from the TOA radiance, provided that the atmospheric components are known.

It is customary to use a suitable radiative transfer model to estimate $L_a(t)$, $L_a(b)$ and τ_{oo} and in this case MODTRAN 4 was used. To run the MODTRAN code one needs to input the sun satellite geometry and the atmospheric conditions during the satellite overpass. The required atmospheric input parameters to run MODTRAN include the aerosol amount, the temperature and water vapour profiles and the amount of ozone or other gases. Unless specifically observed, atmospheric profiles are not known during the satellite overpass time; hence standard atmospheres will have to be used in the software with modifications. This is usually done by scaling the standard atmospheric profiles of water vapour and ozone to match the total estimated values. If the integrated value of the scaled profile matches the total value that atmospheric profiles is used in MODTRAN code.

In the thermal domain a single run of MODTRAN4 with 95% emissivity and air temperature about 300K would be used to obtain the necessary outputs to determine three atmospheric parameters $L_a(t)$, $L_a(b)$ and τ_{oo} . The main outputs obtained from MODTRAN4 run at each wavelength are PTEM (path-thermally emitted radiance), GRFL (total ground-reflected radiance), SFEM (the surface-emitted radiance) and the TRAN (atmospheric transmittance).

$$L_{PTEM} = L_a(t) \quad (5-2)$$

$$L_{GRFL} = (1 - \varepsilon)L_a(b)\tau_{oo} \quad (5-3)$$

$$TRAN = \tau_{oo} \quad (5-4)$$

Using (5-2) to (5-4), three spectra of atmospheric parameters in the thermal domain can be determined from the MODTRAN4 output.

5.2.1 Inversion of Land Surface Temperature

In principle equation (5-1) is strictly valid for the radiance observed at a single wavelength emanating from homogeneous isothermal surfaces. However in practice, the radiance is measured over a band of wavelengths;

thus with little error introduced due to integration, for a certain sensor band “ i ” we can rewrite (5-1) as

$$L_i(T_i) = L_i^\uparrow + \tau_i[\varepsilon_i B_i(T_s) + (1 - \varepsilon_i)L_i^\downarrow] \quad (5-5)$$

where $L_i(T_i)$ is the at-sensor radiance (T_i is the brightness temperature), τ_i , L_i^\uparrow and L_i^\downarrow are the band specific values of atmospheric transmissivity, up-welling path radiance and the down-welling atmospheric radiance respectively (obtained using the MODTRAN4 outputs and the sensor response functions), ε_i is the band specific surface emissivity and $B_i(T_s)$ is the Planck radiance at surface temperature T_s .

Provided that ε_i is known a priori, T_s can be easily retrieved by inversion of the Planck’s Law as

$$T_s = \frac{c_2}{\lambda_i} \left[\ln \left(\frac{c_1}{\lambda_i^5 B_i} + 1 \right) \right]^{-1} \quad (5-6)$$

where $c_1 = 1.19104 \times 10^8 \text{ Wm}^{-2} \mu\text{m}^4 \text{sr}^{-1}$ and $c_2 = 1.438769 \times 10^4 \text{ } \mu\text{mK}$ are the constants from the Planck’s Law, B_i is the radiance emitted by a black body and λ_i is the effective wave length of the band.

The above deterministic approach to retrieve LST is applicable for surfaces such as water and closed canopy forests for which ε is not in question. However for most terrestrial surfaces ε varies between 0.7 and 1.0, therefore the value has to be determined along with the temperature.

With the advent of sensors with multispectral capabilities in the thermal infrared region, methods have been developed to retrieve LST using several thermal bands. However as (5-5) indicates, if the radiance is measured in n spectral bands, always there will be $n+1$ unknowns (n emissivities and the surface temperature) hence the separation of T_s and ε data from the measured radiance alone is unfeasible. Different techniques have been developed to address the problem by making use of additional information determined independently. One such method is the temperature and emissivity separation (TES) method, developed by Gillespie et al. (1998).

5.2.2 Temperature and Emissivity Separation algorithm

TES method originally developed for the ASTER sensor having five bands in the thermal infrared region is capable of providing LST and surface emissivities simultaneously. With recent improvements the TES algorithm is

capable of concurrently producing accurate estimates of emissivities and surface temperatures for the land surface. (Gillespie et al., 1998). The algorithm combines three modules viz. Normalized Emissivity Method (NEM), Ratio, and Maximum–Minimum Difference (MMD) as described in ATBD by Gillespie et al. (1998). TES algorithm is primarily based on the radiative transfer equation applied to each thermal band. The NEM module employs land-leaving TIR radiance data that have been previously corrected for τ_i and L_i^\uparrow (Gillespie et al., 1998). However in order to remove the reflected component of L_i^\downarrow , TES algorithm uses an iterative approach.

The iteration begins with an assumed ε_{max} value around 0.98 which is within ± 0.015 for most of the terrestrial surfaces. The NEM module starts with estimating ground emitted radiance of band i as

$$R_i = L_i' - (1 - \varepsilon_{max})L_i^\downarrow \quad (5-7)$$

where L_i' is the land-leaving radiance

Next the NEM temperature T_{NEM} is taken to be the maximum temperature T_i estimated from the R_i for the different bands.

$$T_i = \frac{c_2}{\lambda_i} \left[\ln \left(\frac{c_1 \varepsilon_{max}}{\lambda_i^5 R_i} + 1 \right) \right]^{-1} \quad (5-8)$$

$$T_{NEM} = \max(T_i)$$

In the next step T_{NEM} will be used to calculate black body radiance $B_i(T_{NEM})$ which in turn is used to estimate NEM emissivities ε_i as follows.

$$\varepsilon_i = \frac{R_i}{B_i(T_{NEM})} \quad (5-9)$$

The ratio module computes the relative emissivities (β_i) by taking the ratios of the NEM emissivities to their average as follows.

$$\beta_i = \frac{\varepsilon_i}{\left[\sum \varepsilon_i \right] / 5} \quad (5-10)$$

In the MMD module the β spectrum is scaled to actual emissivities using an empirically determined relationship between MMD and ε_{min} where MMD is

firstly estimated as the maximum minimum difference of the β spectrum (spectral contrast).

$$MMD = \max(\beta_i) - \min(\beta_i)$$

From the ASTER spectral libraries following simple power law relationship between ε_{min} and MMD can be obtained.

$$\varepsilon_{min} = a - b \times MMD^c \quad (5-11)$$

where the coefficient a , b and c depends on the particular band combination and the selected emissivity spectra for the analysis. The formula originally calculated for the ASTER sensor using 86 laboratory spectra found the coefficients $a= 0.994$, $b=0.687$ and $c=0.737$ (Gillespie et al. 1998). The empirical relationship (5-11) has been recalculated for AHS sensor using the bands 72 to 79 excluding 75 (config2) by Sobrino et al. (2008). They have proposed the following relationship to be used with the above AHS band combination.

$$\varepsilon_{min} = 0.999 - 0.777 \times MMD^{0.815} \quad (5-12)$$

In the present work the new coefficients proposed by Sobrino et al. (2008) are adopted with a similar AHS band combination.

Finally the emissivities are calculated from the β spectrum as

$$\varepsilon_i = \beta_i \left(\frac{\varepsilon_{min}}{\min(\beta_i)} \right) \quad (5-13)$$

Using the calculated emissivities a refined ε_{max} value can be obtained as $\varepsilon_{max} = \max(\varepsilon_i)$.

The process is repeated until the results converge and usually occurs after two or three iterations. Eventually the land surface temperature is estimated with equations (5-7) and (5-8), using the atmospherically corrected radiance of the band in which the emissivity is maximum.

5.3 Measurements

5.3.1 Tower-based radiometric measurements

A set of thermal radiometric measurements were carried out by the Global Change Unit of the University of Valencia in the framework of the EAGLE2006 experimental field campaign for the retrieval of bio-geophysical parameters

such as land surface emissivity and temperature as the primary objective of the aforesaid measurements. The radiometric measurements were carried out in the thermal infrared region using various instruments that include fixed field-of-view (FOV) and single band or multi bands radiometers. Moreover the experimental work of the Global Change Unit of the University of Valencia extended to the measurement of atmospheric radiances, air temperature, temperature transects and angular measurements within the site area as described in detail in EAGLE 2006 Final report (Timmermans et al., 2008).

In the Speulderbos site various instruments were used to measure in the thermal infrared domain that includes multiband and single band radiometers with fixed FOV. The CIMEL model CE-312-1 is a radiance-based thermal-infrared radiometer composed of an optical head and a data storage unit. The CE312-1 detector includes one broad-band filter (8-13 μm), and three narrower filters, (8.2–9.2 μm , 10.5–11.5 μm and 11.5–12.5 μm). Temperature of an external blackbody can be measured with a temperature probe, especially for the estimation of absolute emissivity. Different fixed scenarios were selected to collect data in the thermal infrared domain. Three Raytek MID radiometers with FOV of 30°, 30° and 6° respectively were used. They have an infrared sensor with a single band 8–14 μm . They range from -40° up to 600°C with a sensitivity of 0.5 K and an accuracy of 1K. Three different Licor LI-1000 data loggers have been used to store data from the radiometers set up on the masts. The tower-based radiometers directly measure the land leaving radiance (LLR) and the temperature that is obtained by inverting the Planck's law using the LLR is defined as the radiometric temperature.

Table 5-1: Various thermal instruments and their measurement frequency

Date	Local time	Instrument	Measurement
13/06/06	11 hrs - 17 hrs	CIMEL CE312-1 measuring canopy	Temporal series/ Nadir view. Interval =3 Sec.
		RAYTEK MID 1 measuring canopy	Temporal series/Nadir view. Interval =1 Sec.
		RAYTEK MID 3 measuring canopy	Temporal series/ 55° off Nadir view. Interval =1 Sec.
		RAYTEK MID 2 measuring ground	Temporal series Interval =1 Sec.

Table 5-2: Main technical specifications of field radiometers

Instrument	Spectral Range (μm)	Temp. Range ($^{\circ}\text{C}$)	Accuracy	Res.	FOV
CIMEL	8.0 – 13.0	-80 to 50	0.1	8 mK	10 $^{\circ}$
CE312-1	11.5 – 12.5			50 mK	
	10.5 – 11.5			50 mK	
	8.2 – 9.2			50 mK	
RAYTEK MID	8 – 14	-40 to 600	1	0.5	30 $^{\circ}$ /6 $^{\circ}$

5.3.2 Contact temperature measurements

Under the micrometeorological measurements (already described in chapter 3) surface contact temperatures were also measured with Negative Temperature Coefficient (NTC) sensors on needles, mosses and trunks at ground level, and on needles, branches and trunks in the canopy between 17 and 24 m height.

The raw signal (resistance) measured by the thermistors was initially recorded in ohms and later converted to Contact temperature ($^{\circ}\text{C}$) using the following relationship between the resistance (R) and the contact temperature (T_c) of the sensors:

$$T_c = -1.77 \times 10^{-6} R^3 + 1.7 \times 10^{-3} R^2 - 0.55R + 62.03 \quad (5-14)$$

Table 5-3: Description of NTC sensors attached to different parts of the canopy

Number	Location (between 17-24 m height)
1	Needle on branch pointing north, shadow (24 m)
2	Needle on south pointing branch, sunlit (24 m)
3	Trunk, sunlit (24 m)
4	Sunlit branch (24 m)
5	Shadow branch (17 m)
6	Trunk (17 m)

5.3.3 Airborne data acquisition

For retrieving LST from remote sensing data, six AHS images acquired by the INTA airplane over Speulderbos area on the 13th of June 2006 (DOY-164) at two different altitudes have been selected. These images had been acquired in parallel to the ground based radiometric measurements carried out from the top of the Speulderbos tower by the Global change unit of the University of Valencia in the framework of the EAGLE 2006 field campaign. With respect to the location of the Speulderbos tower and the AOI of surrounding forest, four of the selected images are nadir-looking whereas other two would be considered as off-nadir images with an approximate view zenith angle of 40 $^{\circ}$.

The nominal ground resolution of the images acquired by the low-altitude flight (975 m AGL) is about 2.4 m, whereas the ground sample distance of the images acquired by the high-altitude flight (2743 m AGL) is 6.9 m. The observation details of the AHS images are summarized in Table 5-4.

Table 5-4: Observation details of AHS images acquired over Speulderbos area

Image file No	Day of year	Time of acquisition (UTC)	Altitude a.m.s.l. (km)	True heading	Solar azimuth/elevation
AHS-PA3BD	164	10:51	1.021	158°	157°/61°
AHS-P02AD	164	11:34	2.789	161°	177°/61°
AHS-P01AD	164	11:50	2.789	239°	185°/61°
AHS-P05BD	164	12:24	1.021	68°	201°/60°
AHS-P04BD*	164	12:32	1.021	248°	203°/60°
AHS-P06BD*	164	12:41	1.021	68°	207°/59°

* Off-nadir view

Table 5-5: Spectral characteristics of AHS thermal bands

Band	FWHM (μm)	Effective wavelength (μm)
71	7.95–8.42	8.18
72	8.45–8.84	8.66
73	8.94–9.35	9.15
74	9.38–9.81	9.60
75	9.85–10.27	10.07
76	10.31–10.86	10.59
77	10.89–11.45	11.18
78	11.49–12.05	11.78
79	12.09–12.57	12.35
80	12.65–13.14	12.93

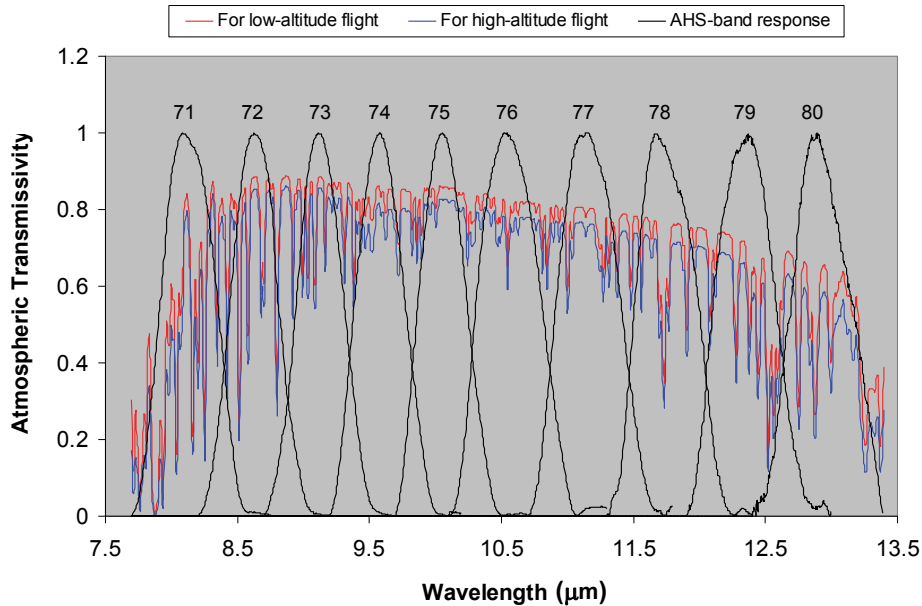


Figure 5-1: Spectral response functions of AHS thermal bands 71 to 80 with atmospheric transmissivity for different flight altitudes.

5.4 Results

5.4.1 Output of MODTRAN4

The main outputs obtained from MODTRAN4 run at each wavelength PTEM (path-thermally emitted radiance), GRFL (total ground-reflected radiance), SFEM (the surface-emitted radiance) and the TRAN (atmospheric transmittance) are shown in Figure 5-2. Also shown in Figure 5-3: Atmospheric parameters from MODTRAN 4 outputs

are the three atmospheric parameters $L_a(t)$, $L_a(b)$ and τ_{oo} estimated using the MODTRAN4 outputs and the relationships described in equations (5-2) to (5-3). The band specific values of atmospheric transmissivity, up-welling path radiance and the down-welling atmospheric radiance (τ_i , L_i^\uparrow and L_i^\downarrow respectively for $i=71$ to 80) estimated using the spectral values of $L_a(t)$, $L_a(b)$ and τ_{oo} and the sensor response functions of corresponding AHS band are shown in Figure 5-4.

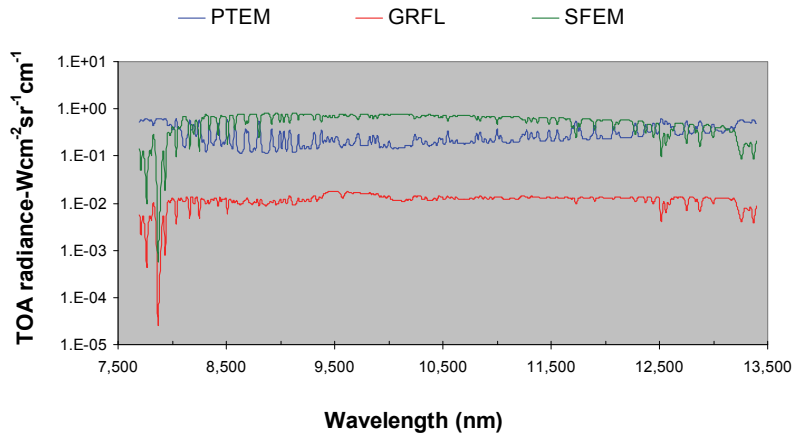


Figure 5-2: Basic output parameters of MODTRAN 4 run

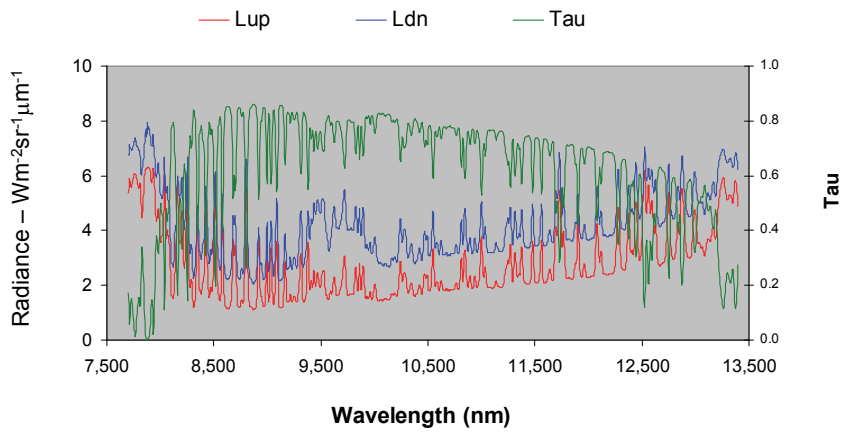


Figure 5-3: Atmospheric parameters from MODTRAN 4 outputs

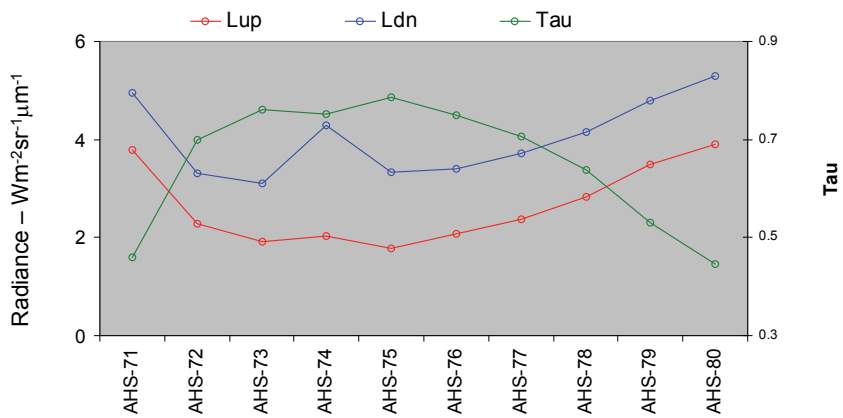


Figure 5-4: AHS Band specific atmospheric parameters

5.4.2 Tower-based temperature measurements

Figure 5-5 shows the temporal variation of radiometric temperature of the Douglas fir canopy observed with Raytek MID instruments at two different view angles in the after-noon hours of the DOY 164. The temporal pattern exhibits a temperature difference around five degrees centigrade between the nadir view observation and the 55° off nadir observation. Also shown in Figure 5-6 are the contact temperature measurements made using negative temperature coefficient (NTC) sensors at 24 m level attached to needles, branches and the trunk of the Douglas fir canopy during the same period. According to Figure 5-6 the temperature values of NTC sensors attached to branches show the highest temporal variability with values varying between 31°C and 37°C during the illustrated period. However the trunk temperatures and needle temperatures show comparatively less variability as the values fluctuate between 32°C and 36°C and 31°C and 35°C respectively. By comparing different temperature charts shown in Figure 5-5 and Figure 5-6 it can be seen that the canopy component temperature values in general exceed the observed off-nadir view radiometric temperatures. Conversely the nadir view radiometric temperature observations show consistently higher values with respect to three component temperature measurements as evident from Figure 5-5 and Figure 5-6.

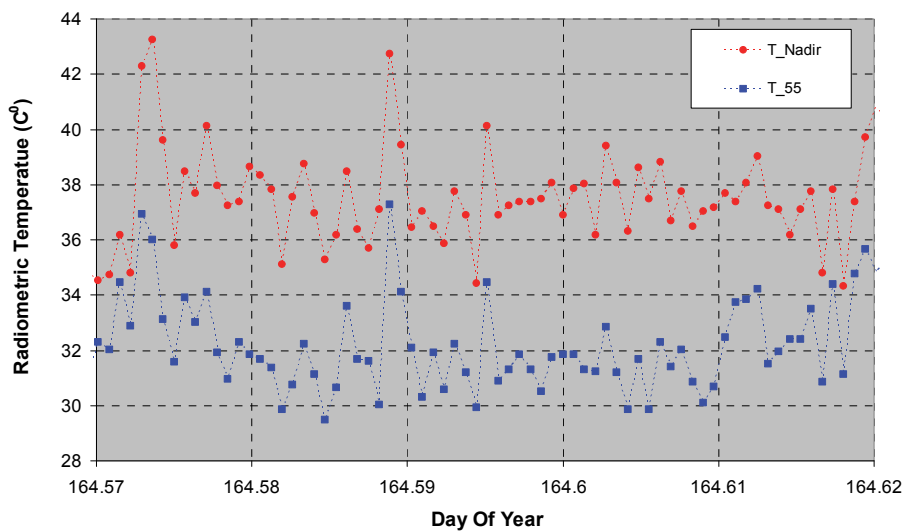


Figure 5-5: Tower-based radiometric temperature at two different view directions

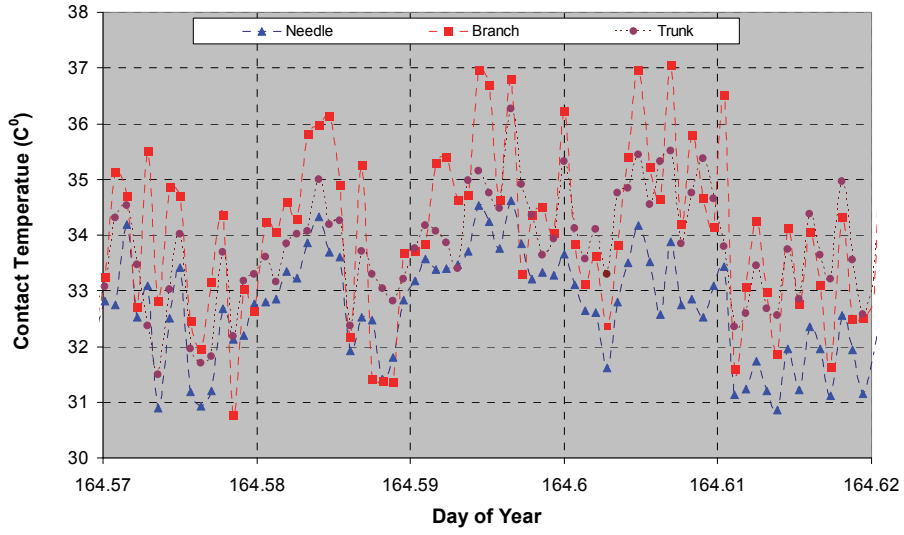


Figure 5-6: Contact temperature measurements of canopy components all at 24 m level

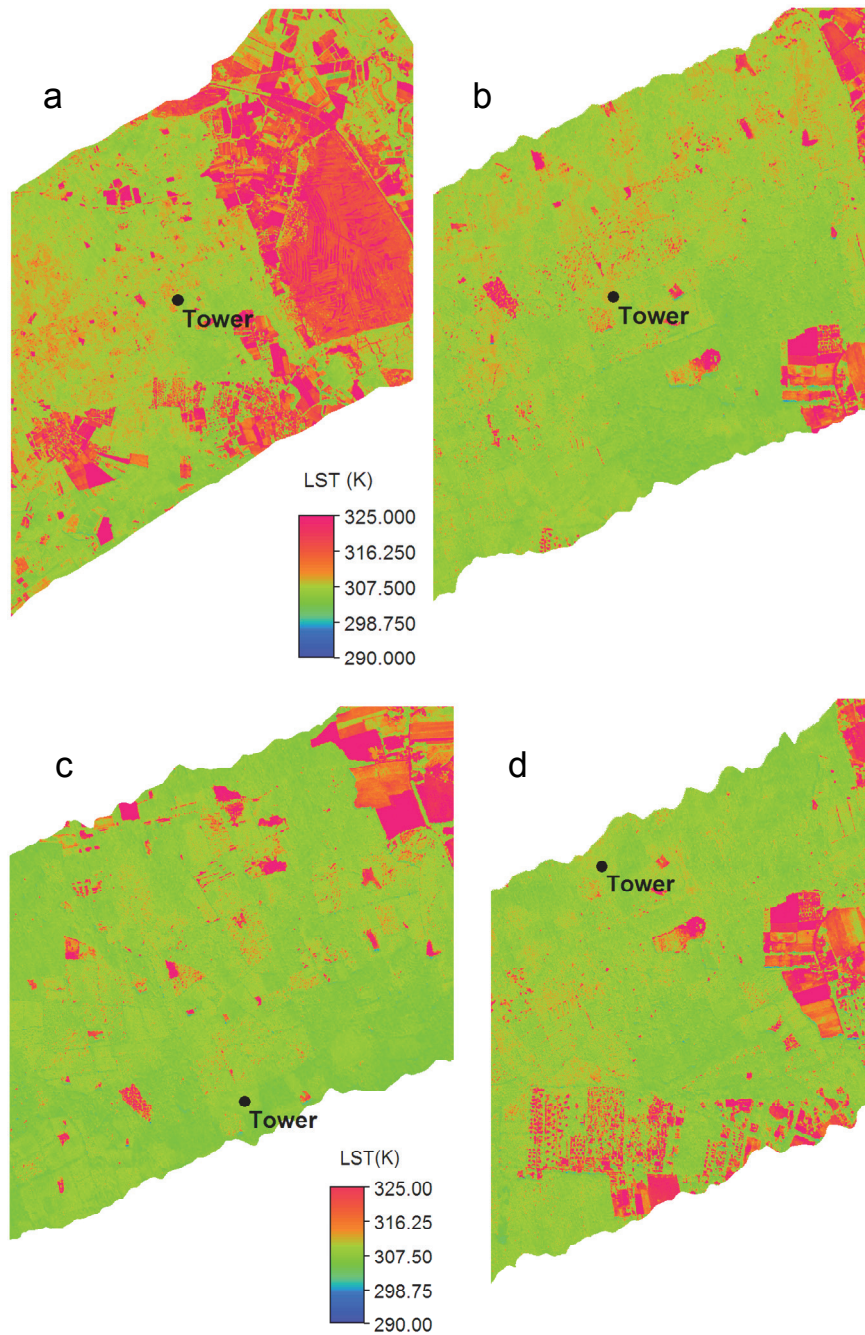


Figure 5-7: LST distribution from AHS images; (a) & (b) show the nadir view of the tower location acquired by high-altitude and low-altitude flights respectively. (c) & (d) show the off-nadir view of the same acquired by low-altitude flights.

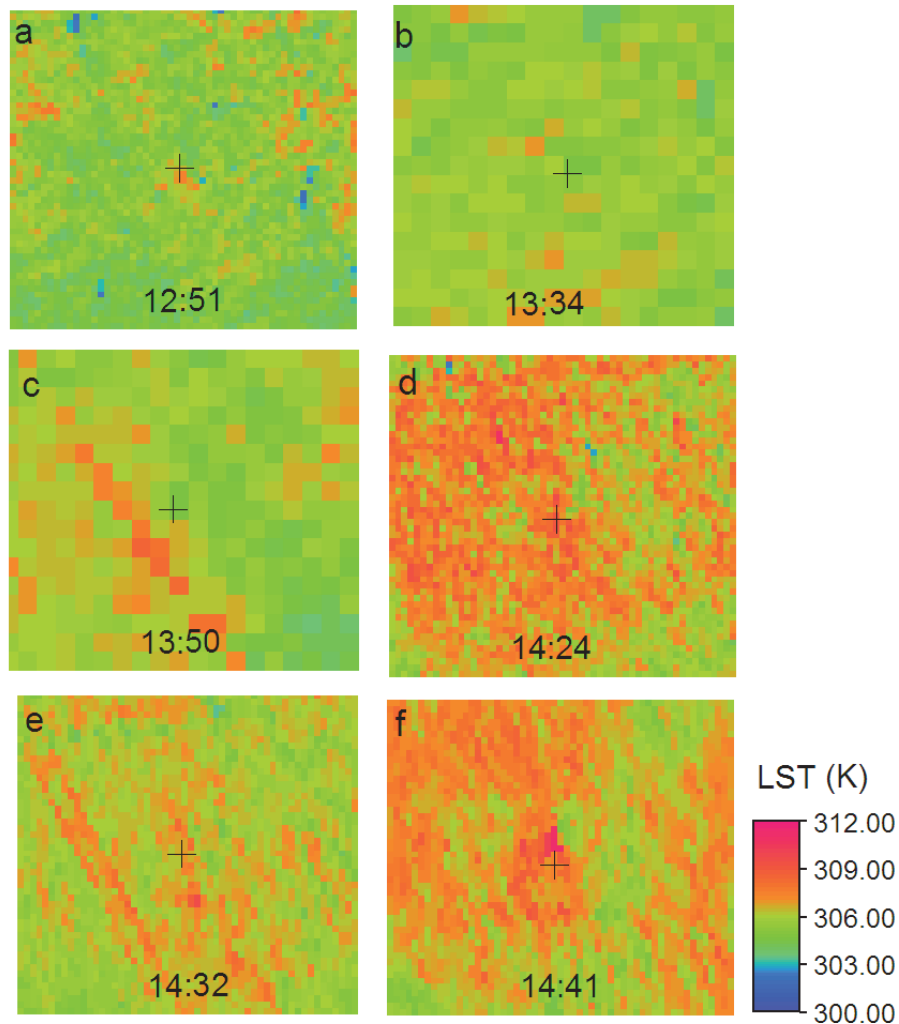


Figure 5-8: Spatial and temporal distribution of LST of the Douglas fir forest (shown here is an area of approximately 100 m X 100 m enclosing the tower) Panels (a) to (f) indicate the local time of image acquisition. The cross in the middle denotes the location of the Speulderbos tower.

5.4.3 Comparison of tower measurements vs. LST

LST maps derived from four different AHS images are shown in Figure 5-7(a) to (d). Images shown in (a) and (b) are nadir-looking (with respect to the tower location) and acquired by high-altitude & low-altitude flights respectively. In Figure 5-7(c) and (d) are the LST images with an off-nadir view both having acquired at the same elevation by the low-altitude flights. In Figure 5-8(a) to (f) show the expanded view of LST maps for a 100 m X 100 m area encircling the Speulderbos Tower. The nadir view LST images (a)

to (d) show evidence of progressively warming canopy surface between 12:51 and 14:24 hrs. (local time). By visual inspection the off-nadir image (e) shows low LST regions (this is also visible in (f) to a lesser extent) compared to nadir image (d). This reduction in temperature is further evident from the descriptive statistics given in Table 5-6 as the average LST has subtly decreased from the nadir image (P05BD) to off-nadir images despite the fact that gradual warming of the surface has taken place with time.

Table 5-6: Spatial statistics of AHS derived LST estimates for the area of interest

Image File No	View Geometry	Average LST (C ⁰)	Std. Dev. LST (C ⁰)	Minimum LST (C ⁰)	Maximum LST (C ⁰)
AHS-PA3BD	Nadir	32.02	0.83	29.01	35.00
AHS-P02AD	Nadir	32.39	0.58	30.64	33.83
AHS-P01AD	Nadir	32.62	0.82	30.45	35.46
AHS-P05BD	Nadir	33.71	0.99	29.14	37.74
AHS-P04BD	Off-nadir	32.98	0.68	30.10	36.50
AHS-P06BD	Off-nadir	33.55	0.86	31.30	38.07

The charts of Figure 5-9 and Figure 5-10 illustrate a comparison of tower-based temperature versus remotely sensed LST. In Figure 5-9 the needle temperature (NTC) measured at 24 m level and tower-based radiometric temperature measured with the off-nadir view are compared against the remotely sensed LST values estimated for the area of interest around the measurement tower. In Figure 5-10 similar comparison is made using trunk temperature (NTC) measured at 17 m level and radiometric temperature measured with the nadir view radiometer. As can be seen from Figure 5-9, the image based average LST values are in good agreement with the needle temperature measured using NTC sensors at 24 m level, although the off-nadir view radiometric temperature values are generally lower. Nevertheless both the NTC measured trunk temperature at 17 m and nadir view radiometric temperature measurements are systematically higher than average LST values of AOI as depicted in Figure 5-10.

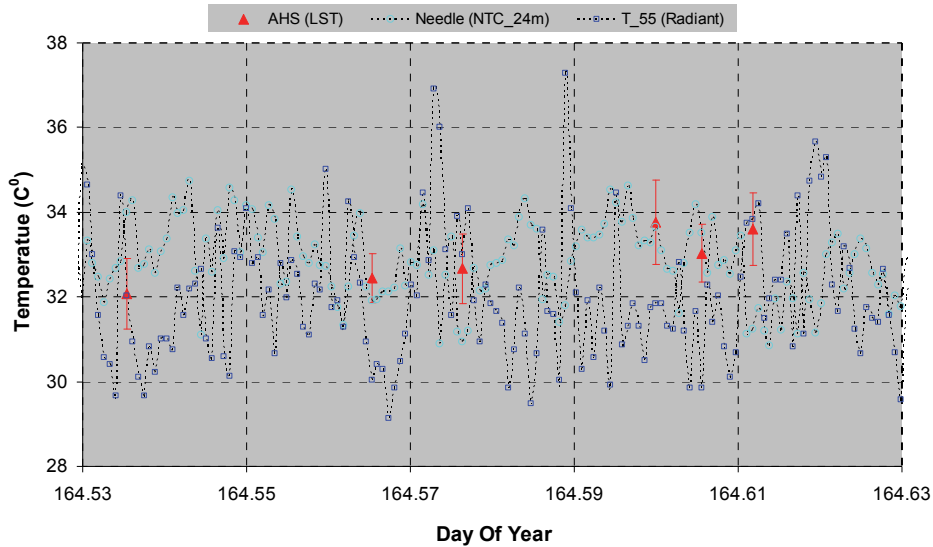


Figure 5-9 : Comparison of tower-based vs. remotely sensed temperature of Douglas fir forest. The tower-based observations are one minute averages of observations are one minute averages of observations of needle temperature at 24 m and radiometric temperature with off-nadir view. The LST from AHS images (red triangles) are the spatial averages of the area of interest. The error bars indicate the standard deviation of temperature for same.

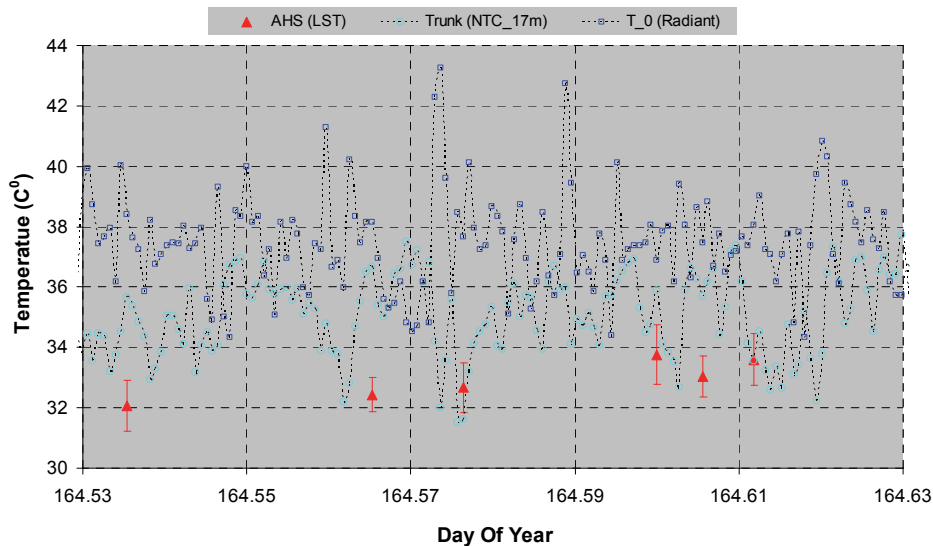


Figure 5-10 : Comparison of tower-based vs. remotely sensed temperature of Douglas fir forest. The tower-based observations are one minute averages of observations of trunk temperature at 17 m and radiometric temperature with nadir view. The LST from AHS images (red triangles) are the spatial averages of the area of interest. The error bars indicate the standard deviation of temperature for same.

5.5 Summary and Conclusions

Land surface temperature is a key input variable for wide range of applications for example hydro-meteorology, numerical weather prediction, vegetation monitoring etc. LST for large areas can only be retrieved from surface-leaving radiation measured by EO satellite sensors. These radiation measurements represent the integrated effect of the surface air continuum hence, superior to point based measurements for discriminating the spatially distributed surface characteristics. While LST can be successfully retrieved from remotely sensed TIR measurements, for the better accuracy of the resulted temperature, three atmospheric interferences viz. atmospheric transmittance, self-emitted path radiance of atmosphere at top and the bottom have to be accounted for. Furthermore the knowledge of land surface emissivity is required in order to decouple the contributions of LST and LSE (reflected down-welling radiance) to the land-leaving radiance. In the absence of a priori knowledge of LSE, a methodology which can determine both LST and LSE simultaneously can be adopted, as long as multispectral TIR data is available.

In this chapter we used remotely sensed TIR data from Airborne Hyperspectral Scanner to estimate spatially distributed LST of a forested area. AHS is a new generation airborne sensor possessing multispectral thermal infrared capability, with 10 thermal bands covering the range between 8 and 13 μm of the electromagnetic spectrum. The data acquired from the AHS sensors provided the opportunity to retrieve the LST of the forest canopy with a very high spatial resolution. Also the concurrent tower-based temperature measurements provided limited ground truth for a spatio-temporal analysis of surface temperature in an area covered with Douglas fir trees. The method adopted here for concurrent determination of LST and LSE is the widely-used TES algorithm together with the MODTRAN4 preprocessor for calculating the required atmospheric contributions.

The tower based radiometric temperature measurements of canopy surface show that there is a marked difference between the values observed by the Nadir held and off-nadir instruments where the observed nadir temperature is consistently higher than the off-nadir temperature. Further the comparison of contact temperature measurements (Needle) at 24m level against radiometric temperature shows that canopy component temperature variation is more or less equal to the magnitude and pattern of off-nadir radiometric temperature. However the AHS derived LST values show that the difference between the spatially averaged temperature of the AOI from Nadir image and off- nadir image is subtle. Furthermore the AHS derived average temperature values are generally in good agreement with the tower based component temperature measured at 24 m level whereas the component

temperatures (trunk) measured at 17 m are consistently higher. It is further observed that the AHS derived average LST values are much lower than the tower-based nadir view radiometric temperature values. It may be noted that in comparison with off-nadir radiometric temperature the TES method provides LST with RMSE around 1.9K while the corresponding value with respect to component temperature measured at 24 m is around 1.4 K.

The above results clearly show the anisotropic behavior of the forest canopy surface where a noticeable difference is observed between the nadir view and off-nadir view radiometric temperature. However compared to the angular variations observed with tower-based radiometric temperatures the image based average LST shows subtle differences where the maximum is around 0.8K between AHS-P05BD and P04BD. Such difference observed with tower-based and remotely sensed temperature can be partly attributed to the narrow field of view of the instrument. Usually a nadir view radiometer sees shaded part of the canopy hence the average nadir view temperature should be lower than that of off-nadir observation. However in this case the temperature of mid layers of the canopy appears to be warmer than the upper layer as also evident from the contact temperatures at 17 m and the 24 m. Hence the nadir view radiometer with a limited field of view sees comparatively warmer branches and trunk space of the canopy whereas the off-nadir view radiometer sees only the upper canopy surface which is well-ventilated. However airborne sensor which has a comparatively larger field of view does not show a big temperature difference between the nadir and off-nadir view images due to the effect of spatial resolution.

Although the effects of atmospheric factors and surface emissivity have been duly accounted during the estimation process, there can be considerable uncertainty in the LST retrievals due to the view angle effects. Hence it is worth evaluating how the LST uncertainty translates in to errors in estimates of surface fluxes especially by remote sensing techniques. A recent inter-comparison study by Timmermans et al. (2007) using two surface energy balance models the TSM (Norman et al., 1995) and the SEBAL (Bastiaanssen et al., 1998) has revealed that uncertainty in LST estimates had a major impact on estimates of sensible heat. They have quantitatively shown that a difference of 3 K in LST produces a 75 % deviation in sensible heat flux estimated with TSM whereas the SEBAL derived sensible heat flux deviates up to 45% for similar LST deviations. Results of this study show that, the use of Airborne multispectral thermal data lead to much smaller LST deviations from the tower measured temperature with off-nadir view. This in turn should increase the accuracy of estimated Heat fluxes based on the LST. Also the adopted TES method solves the problem of the emissivity uncertainty to a great extent. However, in order to obtain better results adopting an accurate atmospheric correction procedure is essential.

6 Conclusions and Recommendations

6.1 Conclusions

The aim of this thesis is to integrate tower-based measurements with EO data for estimating spatially and temporally distributed surface variables of a forest canopy for improved quantification of surface-atmosphere interactions. This study mainly focuses on three of the most important surface variables for estimating surface fluxes, namely the aerodynamic roughness, land surface albedo and land surface temperature.

In this study we presented a methodology using high resolution Terrestrial Laser Scanning data together with Airborne Laser Scanning data to digitally map the upper canopy surface of a Douglas fir forest. Also a framework was presented to extract canopy morphometric details using the digital canopy height model (CHM) with the aim of estimating aerodynamic roughness of a region covered by the forest. We also evaluated two aerodynamic approaches within the context of estimating roughness parameters of the same forest using turbulent flux measurements made in the roughness sub-layer. We further examined the spatial and temporal variability of canopy surface albedo of the Douglas fir forest stand using atmospherically corrected multi-scale remote sensing data and in-situ solar radiation measurements. This analysis was extended to examine the effect of spatial resolution in discriminating albedo characteristics of three distinct forest classes by quantifying the spatial structure using a variogram analysis. Finally we demonstrated the retrieval process of directional land surface temperature from Airborne Hyperspectral Scanner (AHS) data and validated against the in-situ temperature measurements collected during the airborne image acquisition.

In chapter 2 we concluded that it is feasible to extract surface geometric parameters of a forest canopy from a digital canopy height model constructed using laser scanning technique. However it is imperative that one should be aware of the inherent strengths & weaknesses of the adopted techniques (ALS and TLS) for regional scale applications. Obviously for mapping large areas ALS technique is more efficient compared to TLS. Yet to maintain the accuracy within the permissible limits with ALS, proper sampling is important. Applying the TLS for a test plot representing a large area will be useful to make a judgement on the sampling distance to be adopted with ALS. Erroneous sampling with ALS technique is most likely to under estimate the roughness density due to surface smoothing. For example with ALS method, tree tops are likely to be missed as a consequence of the under-sampling and this may particularly affect coniferous trees such as fir or spruce. A technique which is regularly liable to miss the tree apexes (this could occur to a lesser extent with TLS due to occlusion and wind effect) may favour the use of paraboloid model. Therefore when applying ALS techniques to large areas

with different canopy geometries one has to take care of these limitations particularly to select the correct sampling distance as well as the appropriate geometric model.

In chapter 3 it was shown that both d_0 and h_a can be modelled as quadratic functions of h_c . Furthermore, given that z_0 and d_0 are coupled through h_a , z_0 also can be expressed as a quadratic function of h_c . However for relatively short vegetation more often than not z_0 and d_0 are estimated as simple quotients of h_c hence these non-linear relationships appear to be incompatible with conventional wisdom. This implies that the momentum absorption characteristics of tall forest canopies are intrinsically more complex than those of more typical agricultural canopies. Therefore when applying the morphometric models discussed in chapter 2 for tall canopies to estimate normalized displacement height and roughness length, modifications should be made to include roughness element density as well as the canopy height information. In chapter 3 it was also shown that when using the variance method, the estimated roughness parameters are very much sensitive to the chosen value of coefficient C_1 . Selection of proper value for C_1 is crucial as the coefficient mainly causes variance method to compute systematically higher or lower H . Hence the operational use of the variance method is constrained unless otherwise the coefficient C_1 is locally calibrated.

In chapter 4 based on the variogram analysis it was shown that the pixel size required to capture the albedo spatial variability of three forest classes should be less than 3 m. This implies that the AHS low-altitude image was capable of differentiating the spatial heterogeneity of three selected forest classes whereas the AHS high-altitude image probably would detect the spatial variability of broadleaf class to some extent. As also evident from the albedo histograms, out of the three sensors, ASTER being the one with the largest pixel size represses spatial variability in all three forest classes due to averaging. Given the spatial resolution of different sensors used in this study and the range values derived using the variogram analysis for different forest classes, the hypothesis that largest discrepancy in surface albedo variability would occur with ASTER estimates in needleleaf forest class was quantitatively confirmed and the results have shown that with respect to tower-based albedo measurements the error in estimated surface albedo using airborne imageries is within $\pm 10\%$ whereas the corresponding error for satellite images is around $\pm 40\%$. Since the albedo measurements in this location are around 0.09, the corresponding errors in daily net radiation estimate are about 3 Wm^{-2} and 12 Wm^{-2} for airborne and space-borne imageries respectively. The slight differences in remotely sensed surface albedo estimates at this location do not translate into significantly high errors in heat fluxes. Furthermore the computations show that often the daily mean

albedo exceeds the instantaneous albedo observed around local solar noon by about 15%.

In chapter 5 the use of Airborne multispectral thermal data in this study leads to a more accurate values of surface temperatures, albeit slightly, and the adopted TES method solves the problem of the emissivity uncertainty. However, in order to obtain the good results adopting an accurate atmospheric correction procedure is essential. The results clearly show the anisotropic behavior of the forest canopy surface where a noticeable difference (about 5 K) is observed between the tower-based nadir view and off-nadir view radiometric temperature. However compared to the angular variations observed with tower-based radiometric temperatures the image based average LST shows subtle differences where the maximum is around 0.8 K between nadir and off-nadir images. This inconsistency observed with tower-based and remotely sensed temperature can be partly attributed to the disparity in sensor field of view. Particularly a nadir view radiometer with a limited field of view sees relatively warmer trunk-space of the tall canopy whereas the off-nadir view radiometer sees only the upper canopy surface which is well-ventilated. Nevertheless airborne sensor which has a comparatively larger field of view does not show a big temperature difference between the nadir and off-nadir view images due to the aggregation effect. Also the effect of different atmospheric contributions to the at-sensor radiance due to different path lengths for two sensor view geometries cannot be completely evaded during the LST inversion process.

6.2 Suggestions for further research

Earth Observation data has a major contribution towards understanding the spatial variability in land surface characteristics and in arriving at representative areal values. In this study we successfully demonstrated the ability of EO data acquired using novel instruments such as LiDAR and AHS imager to accurately map spatially distributed surface variables of a tall vegetative canopy surfaces. We primarily confined the analysis to investigate three important surface variables of a relatively homogeneous forest canopy for modelling land-surface interactions viz. momentum roughness, surface albedo and directional land surface temperature. Despite the revelations of this study, tremendous amount of work is still required particularly for the better understanding of surface parameterization schemes for applying energy based land-surface models. Some of the possible future work can be listed under the following groups.

The simple quadratic relationships proposed in this study to estimate aerodynamic roughness parameters, z_0 and d_0 using the tree height information can be easily extended to different forest canopies provided that

spatially distributed canopy height information is available. With recent advancements in estimating canopy height using space-borne RS techniques, spatially distributed canopy height information will be available at regional scale. However for validation of proposed relationships for different forest canopies supplementary tower-based profile and flux measurements are required. These measurements should be extended to altitudes at least more than twice the height of the canopy for estimating roughness sub-layer height.

The ground-based in-situ radiation measurements are essential to validate the remotely sensed surface albedo estimates of different forest classes identified in this work. Since we had the in-situ measurements only for the Douglas fir area more radiation measurements should be made over the other two forest classes as well in future, enabling the validation of remotely sensed albedo estimates. This will be eventually used for estimating the spatially distributed net radiation as well as the ground heat flux components of the energy balance equation.

The spatio-temporal directional surface temperature estimates of the forest canopy can be utilized to parameterize the aerodynamic thermal roughness for sensible heat transfer. This is one of the topics for which additional research is required to broaden the existing knowledge particularly using EO data for energy balance modelling. Also the surface temperature estimates of this analysis together with measured turbulent fluxes can be used to evaluate the current operational method of substituting the hypothetical aerodynamic temperature by remotely sensed surface radiative temperature in bulk surface parameterization. Some studies have proposed modifications to the aerodynamic thermal roughness if the aerodynamic temperature is replaced by the directional TIR surface temperature which is not measured in the optimum view angle. However present work has been performed with a limited data set under a particular set of environmental conditions. Further work should include radiometric temperature measurements covering several view directions in order to extend this approach to a broader set of environmental conditions.

Finally the independent estimates of aerodynamic roughness and the thermodynamic roughness can be combined for evaluating the well-known " kb^{-1} " parameter which is being widely used in surface energy balance modelling. Although several models have been formulated in past few decades for estimating kb^{-1} parameter hardly any model can be used to accurately predict the parameter for tall forest canopies. Therefore future studies could concentrate on this important research topic of estimating kb^{-1} parameter particularly focussing tall vegetative canopies.

Conclusions and recommendations

Bibliography

- Arya, S.P., 2001. Introduction to micrometeorology, 2nd edition. Academic Press, San Diego, 420 pp.
- Balick, L.K., Boyd, A., & Hutchison, B.A. 1986. Directional thermal infrared exitance distributions from a leafless deciduous forest. IEEE Transactions on Geoscience and Remote Sensing, GE-24(5), 693–698.
- Bastiaanssen, W.G.M., Menenti, M., Feddes, R.A., and Holtslag, A.A.M., 1998. "A remote sensing surface energy balance algorithm for land (SEBAL). 1. Formulation." Journal of Hydrology, 212-213(1-4), 198-212.
- Berk, A., Anderson, G.P., Acharya, P.K., Chetwynd, J.H., Bernstein, L.S., Shettle, E.P., Matthew, M.W., & Adler-Golden, S.M. (2000). MODTRAN4 user's manual. Hanscom AFB: Air Force Research Laboratory, Space Vehicles Directorate, Air Force Materiel Command, MA 01731-3010, 97 pp.
- Bonan, G.B., Pollard, D., Thompson, S.L., 1993. Influence of Subgrid-scale heterogeneity in leaf-area index, stomatal-resistance, and soil moisture on grid-scale land-atmosphere interactions, J. Clin., 6, 1882-1897.
- Bosveld, F.C., 1997. Derivation of fluxes from profiles over moderately homogeneous forest. Boundary-Layer Meteorol. 84, 289–327.
- Bosveld, F.C., 1999. Exchange Processes between a Coniferous Forest and the Atmosphere. PhD Thesis, Wageningen University, The Netherlands, pp 181.
- Brutsaert, W., 1982. Evaporation into the Atmosphere. Reidel Publishing Co, Dordrecht, Holland, 299 pp.
- Burden, R.L., Faires, J.D., 2010. Numerical Analysis (9th ed.), PWS Publishers, 872 pp.
- Cellier, P. and Brunet, Y., 1992. Flux-gradient relationships above tall plant canopies. Agric. For. Meteorol. 58, 93-117.
- Cohen, W.B., Spies, T.A., Bradshaw, G.A., (1990). Semivariograms of digital imagery for analysis of conifer canopy structure. Remote Sensing of Environment, 34, 167–178.
- Colin, J., Faivre, R., 2010. Aerodynamic roughness length estimation from very high-resolution imaging LIDAR observations over the Heihe basin in China. Hydrol. Earth Syst. Sci., 7, 3397-3421.
- Curran, P.J., (1988). The semivariogram in remote sensing: an introduction. Remote Sensing of Environment 24, 493–507.
- Dash, P., Göttsche, F. -M., Olesen, F.-S. and Fischer, H., 2002. Land surface temperature and emissivity estimation from passive sensor data: theory and practice-current trends, International Journal of Remote Sensing, 23: 13, 2563 -2594.
- Davidson, A., Wang, S., (2004). The effect of sampling resolution on the surface albedos of dominant land cover types in the North American boreal region. Remote Sensing of Environment, 93, 211–224

- De Bruin H.A.R., Moore, C.J., 1985. Zero-plane displacement and roughness length for tall vegetation, derived from a simple mass conservation hypothesis. *Boundary-Layer Meteorol.* 31, 39–49.
- De Bruin, H.A.R., Bink, N.I., Kroon, L.J.M., 1991. Fluxes in the surface layer under advective conditions. In: Schmugge, T.J., Andre, J.C. (Eds.), *Workshop on Land Surface Evaporation Measurement and Parameterization*. Springer, New York, pp. 157–169.
- De Bruin, H.A.R., Kohsiek, W., van den Hurk, B.J.J.M., 1993. A verification of some methods to determine the fluxes of momentum, sensible heat and water vapor using standard deviation and structure parameter of scalar meteorological quantities. *Boundary-Layer Meteorol.* 63, 231–257.
- De Ridder, K., 2010. Bulk Transfer Relations for the Roughness Sub-layer. *Boundary-Layer Meteorol.* 134, 257–267.
- De Vries, A.C., Kustas, W.P., Ritchie, J.C., Klaassen, W., Menenti, M., Rango, A., and Prueger, J.H., 2003. Effective aerodynamic roughness estimated from airborne laser altimeter measurements of surface features, *Int. J. Remote Sens.* Vol. 24, No. 7, 1545–1558.
- Dolman, A.J., Moors, E.J., and Elbers, J.A., 2002. Characteristics of the carbon uptake of a mid-latitude pine forest on sandy soil, *Agric. For. Meteorol.*, 111, 157–170.
- Dolman, A.J., Maximov, T.C., Moors, E.J., Maximov, A.P., Elbers, J.A., Kononov, A.V., Waterloo, M.J., van der Molen, M.K., 2004. Net ecosystem exchange of carbon dioxide and water of far eastern Siberian Larch (*Larix cajanderii*) on permafrost, *Biogeosciences*, 1, 133–146.
- Dorsey, J.R., Duyzer, J.H., Gallagher, M.W., Coe, H., Pilegaard, K., Weststrate, J. H, Jensen, N.O., Walton, S., 2004. Oxidized nitrogen and ozone interaction with forests. I: Experimental observations and analysis of exchange with Douglas fir. *Quart. J. Roy. Meteorol. Soc.* 130, 1941–1955
- EEA, 1992. *CORINE Land Cover*, A European Community Project, European Environment Agency Task-Force, Directorate General for the Environment, Nuclear Safety and Civil Protection. Commission of the European Communities.
- FAO & JRC, 2012. *Global forest land-use change 1990–2005*, E.J. Lindquist, R. D’Annunzio, A. Gerrand, K. MacDicken, F. Achard, R. Beuchle, A. Brink, H.D. Eva, P. Mayaux, J. San-Miguel-Ayanz & H-J. Stibig. *FAO Forestry Paper No. 169*. Food and Agriculture Organization of the United Nations and European Commission Joint Research Centre. Rome, FAO.
- Fernandez-Prieto, D., Kesselmeier, J., Ellis, M., Marconcini, M., Reissell, A., Suni, T., 2013. Earth observation for land–atmosphere interaction science, *Biogeosciences*, 10, 261–266.

- Garratt, J.R., 1978. Flux profile relations above tall vegetation. *Quart. J. Roy. Meteorol. Soc.* 104, 199-211.
- Garratt, J.R., 1980. Surface influence upon vertical profiles in the atmospheric near-surface layer. *Quart. J. Roy. Meteorol. Soc.* 106, 803-819.
- Garratt, J.R., 1983. Surface influence upon vertical profiles in the nocturnal boundary layer. *Boundary-Layer Meteorol.* 26, 69-80.
- Garratt, J.R., 1992. *The Atmospheric Boundary Layer*. Cambridge University Press, 316pp.
- Gillespie, A., Rokugawa, S., Matsunaga, T., Cothorn, J.S., Hook, S., & Kahle, A.B., 1998. A temperature and emissivity separation algorithm for advanced spaceborne thermal emission and reflection radiometer (ASTER) images. *IEEE Transactions on Geoscience and Remote Sensing*, 36, 1113–1126.
- Graefe, J., 2004. Roughness layer corrections with emphasis on SVAT model applications. *Agric. For. Meteorol.* 124, 237–251.
- Grant, A.L.M., Mason, P.J., 1990. Observations of boundary-layer structure over complex terrain. *Quart. J. Roy. Meteorol. Soc.*, 116, 159–186.
- Grimmond, C.S.B., Oke, T.R., 1999. Aerodynamic properties of urban areas derived from analysis of surface form. *J. Appl. Meteorol.* 38, 1262-1292.
- Harman, I.N., Finnigan, J.J., 2007. A simple unified theory for flow in the canopy and roughness sub-layer. *Boundary-Layer Meteorol.* 123, 339-363.
- Hasager, C.B., Nielsen, N.W., Jensen N.O., Boegh, E., Christensen, J.H., Dellwik, E., and Soegaard, H., 2003. Effective roughness calculated from satellite-derived land cover maps and hedge-information used in a weather forecasting model. *Boundary-Layer Meteorol.*, 109, 227-254.
- Hicks, B.B., 1981. An examination of turbulent statistics in the surface layer. *Boundary-Layer Meteorol.* 21, 389–402.
- Hiyama, T., Sugita, M., and Kotoda, K., 1996. Regional roughness parameters and momentum fluxes over a complex area. *J. Appl. Meteorol.* 35, 2179-2190.
- Hollaus, M., Wagner, W., Eberhofer, C., and Karel, W., 2006. Accuracy of large-scale canopy heights derived from LiDAR data under operational constraints in a complex alpine environment. *J. Photogramm. Remote Sens.*, 60, 323-338
- Inoue, E., 1963. On the turbulent structure of airflow within crop canopies. *J. Meteorol. Soc. Japan*, 41, 317-326.
- Jasinski M.F., Crago, R.D., 1999. Estimation of vegetation aerodynamic roughness of natural regions using frontal area density determined from satellite imagery. *Agric. For. Meteorol.*, 94, 65-77.

- Kader, B.A., and Yaglom, A. M., 1990. Mean fields and fluctuation moments in unstably stratified turbulent boundary layers. *J. Fluid Mech.* 212, 637-662.
- Katul, G., Hsieh, C., Oren, R., Ellsworth, D., Phillips, N., 1996. Latent and sensible heat flux predictions from a uniform pine forest using surface renewal and flux variance methods. *Boundary-Layer Meteorol.* 80, 249-282.
- Kimes, D.S., Idso, S.B., Pinter, P.J., Reginato, R.J., and Jackson, R.D., 1980. View angle effects in the radiometric measurement of plant canopy temperature. *Remote Sensing of Environment*, 10, 273-284.
- Kustas W.P., Choudhury B.J., Moran M.S., Reginato R.J., Jackson R.D., Gay L.W., Weaver H.L., 1989. Determination of sensible heat flux over sparse canopy using thermal infrared data. *Agric For Meteorol.* 44, 197-216.
- Kustas, W.P., Blanford, J.H., Stannard, D.I., Daughtry, C.S.T., Nichols, W.D., Weltz, M.A., 1994. Local energy flux estimates for unstable conditions using variance data in semi-arid rangelands. *Water Resour. Res.* 30 (5), 1351-1361.
- Kutzbach, J., 1961, Investigations of the modification of wind profiles by artificially controlled surface roughness. Annual Report, Department of Meteorology, University of Wisconsin-Madison.
- Leonard, R.E., Federer, C.A., 1972. Estimated and measured roughness parameters for a pine forest. *J. Appl. Meteorol.* 12, 302-307.
- Liang, S., 2008. Recent advances in land remote sensing: an overview. In Liang, S., editor, *Advances in Land Remote Sensing: System, Modeling, Inversion and applications*: Springer, pp. 1-6.
- Mason, P.J., 1985. On the parameterization of orographic drag. In *physical parameterization for numerical models of the atmosphere*, E.C.M.W.F., reading seminar, 9-13 September 1985, pp. 139-167.
- Martano, P., 2000. Estimation of surface roughness length and displacement height from single-level sonic anemometer data. *J. Appl. Meteorol.* 39, 708 -715.
- McBratney, A.B., Webster, W., 1981. Spatial dependence and classification of the soil along a transect in north-east Scotland. *Geoderma*, 26, 63-82.
- McGrew, J.C., Monroe, C.B. 2000. An introduction to statistical problem solving in geography (2nd ed.) (p. 110). Boston: McGraw-Hill.
- Menenti, M.; Bastiaanssen, W.G.M.; Hefny, K.; El Karim, M.H.A. 1991. Mapping of groundwater losses by evaporation in the Western Desert of Egypt. Wageningen, Netherlands: Winand Staring Centre. 116 pp.
- Menenti, M. and Choudhury, B.J., 1993. Parametrization of land surface evapotranspiration using a location-dependent potential evapotranspiration and surface temperature range. In: *Exchange processes at the land surface for a range of space and time scales*, Bolle, H.J. et al. (Eds.). I AHS Publ. no. 212 : 561-568.

- Menenti, M., Ritchie, J.C., 1994. Estimation of effective aerodynamic roughness of Walnut Gulch watershed with laser altimeter data. *Water Resour. Res.* 30, 1329–1337.
- Minnis, P., Mayor, S., Smith, W.L., Young, D.F., (1997). Asymmetry in the Diurnal Variation of Surface Albedo. *IEEE Transaction on Geoscience and Remote Sensing*, 35 (4), 879-891.
- Mölder, M., Grelle, A, Lindroth, A., Halldin, S., 1999. Flux-profile relationships over a boreal forest-roughness sub-layer corrections. *Agric. For. Meteorol.* 98–99, 645–658.
- Monin, A.S., Obukhov, A.M., 1954. Basic laws of turbulent mixing in the ground layer of the atmosphere near the ground. *Trudy Geofizicheskogo Instituta, Akademiya Nauk SSSR* 24(151), 163–187.
- Nakai, T., Sumida, A., Matsumoto, K., Daikoku, K., Iida, S., Park, H., Miyahara, M., Kodama, Y., Kononov, A.V., Maximov, T.C., Yabuki, H., Hara, T., Ohta, T., 2008a. Aerodynamic scaling for estimating the mean height of dense canopies. *Boundary-Layer Meteorol.* 128, 423–443.
- Nakai, T., Sumida, A., Matsumoto, K., Daikoku, K., Matsumoto, K., van der Molen, M.K., Kodama, Y., Kononov, A.V., Maximov, T.C., Dolman, A.J., Yabuki, H., Hara, T., Ohta, T., 2008b. Parameterisation of aerodynamic roughness over boreal, cool- and warm-temperate forests. *Agric. For. Meteorol.* 148, 1916-1925.
- Ni, W., Woodcock, C.E., 2000. Effect of canopy structure and presence of snow on the albedo of boreal conifer forests. *Journal of Geophysical Research*, 105 (D8), 11,879- 11,888.
- Oke, T.R., 1978. *Boundary Layer Climates*. (First Edn.) Methuen and Company limited, 435 pp.
- Oleson, K.W., Emery, W.J., Maslanik, J.A., 2000, Evaluating land surface parameters in the Biosphere-Atmosphere Transfer Scheme using remotely sensed data sets. *J. Geophys. Res.*, 105, 7275-7293.
- Padro, J., 1993. An investigation of flux-variance methods and universal functions applied to three landuse types in unstable conditions. *Boundary-Layer Meteorol.* 66, 413–425.
- Panofsky, H., Dutton, J., 1984. *Atmospheric Turbulence: Models and Methods for Engineering Applications*. Wiley, New York, 397pp.
- Physick, W.L., Garratt, J.R., 1995. Incorporation of a high-roughness lower boundary into a mesoscale model for studies of dry deposition over complex terrain. *Boundary-Layer Meteorol.* 74, 55-71.
- Pinty, B., Lavergne, T., Kaminski, T., Aussedat, O., Giering, R., Gobron, N., Taberner, M., Verstraete, M.M., Voßbeck, M. & Widlowski, J.L., (2008). Partitioning the solar radiant fluxes in forest canopies in the presence of snow, *Journal of Geophysical Research*, Vol.113, 13 pp. doi:10.129/2007JD009096.

- Pitman, A.J., A. Henderson-Sellers, F. Abramopolous, A. Boone, C.E. Desborough, R.E. Dickinson, J.R. Garratt, N. Gedney, R. Koster, E.A. Kowalczyk, D. Lettenmaier, X. Liang, J.-F. Mahfouf, J. Noilhan, J. Polcher, W. Qu, A. Robock, C. Rosenzweig, C.A. Schlosser, A.B. Shmakin, J. Smith, M. Suarez, D.L. Verseghy, P. Wetzler, E.F. Wood, Y. Xue, and Z.-L. Yang, 1999. Key results and implications from Phase 1(c) of the Project for Intercomparison of Land-surface Parameterization Schemes. *Climate Dynamics*, **15**, 673-684.
- Prata, A.J., Caselles, V., Coll, C., Sobrino, J.A., and Otle', C., 1995, Thermal remote sensing of land surface temperature from satellites: current status and future prospects. *Remote Sensing Reviews*, *12*, 175-224.
- Prueger, J.H., Kustas, W.P., Hipps, L.E., Hatfield, J. L., 2004. Aerodynamic parameters and sensible heat flux estimates for a semi-arid ecosystem. *J. Arid Environ.* *57*, 87-100.
- Prueger, J.H., Kustas, W.P., 2005. Aerodynamic methods for estimating turbulent fluxes. *Micrometeorology in Agricultural Systems, Agronomy Monograph no. 47*, 407-436.
- Qin, Z., and Karnieli, A., 1999. Progress in remote sensing of land surface temperature and ground emissivity using NOAA-AVHRR data. *International Journal of Remote Sensing*, *20*, 2367-2393.
- Raupach, M.R., 1979. Anomalies in flux-gradient relationships over forest. *Boundary-Layer Meteorol.* *16*, 467-486
- Raupach, M.R., 1992. Drag and drag partition on rough surfaces. *Boundary-Layer Meteorol.* *60*, 375-395.
- Raupach, M.R., 1994. Simplified expressions for vegetation roughness length and zero-plane displacement as functions of canopy height and area index, *Boundary-Layer Meteorol.* *71*, 211-216.
- Raupach, M.R., 1995. Corrigenda, *Boundary-Layer Meteorol.* *76*, 303-304.
- Raupach, M.R., Thom, A.S., Edwards, I., 1980. A wind-tunnel study of turbulent flow close to regularly arrayed rough surfaces. *Boundary-Layer Meteorol.* *18*, 373-397
- Raupach, M.R., Finnigan, J.J., Brunet, Y., 1996. Coherent eddies and turbulence in vegetation canopies: the mixing-layer analogy. *Boundary-Layer Meteorol.* *78*, 351-382
- Roerink, G.J., Su, Z., and Menenti, M. 2000. "S-SEBI: A simple remote sensing algorithm to estimate the surface energy balance." *Physics and Chemistry of the Earth, Part B: Hydrology, Oceans and Atmosphere*, *25(2000)2*, 147-157.
- Rowe, C.M., 1993. Incorporating landscape heterogeneity in the land surface albedo models, *J. Geophys. Res.*, *98*, 5037-5043.
- Schaaf, C., Strahler, A., Martonchik, J., Charlock, T., Rutan, D., Zeng, X., Liang, S., Chopping, M., Lyapustin, A., Rossow, W. 2006: Land White Paper: Global land surface albedo and anisotropy:. Available at

- ftp://ftp.iluci.org/Land_ESDR/Albedo_Schaaf_whitepaper3.pdf (accessed 2007-02-14).
- Sellers, P.J., Randall, D., Collatz, G., Berry, J., Dazlich, C.F.D., and Zhang, C., 1996. A revised land surface parameterization (SiB2) for atmospheric GCMs Part I: Model formulation, *J. Climate*, 9, 676–705.
- Sellers, P.J., Rasool, S.I., Bolle, H.J., 1990. A review of satellite data algorithms for studies of the land surface. *Bull Am Meteorol Soc* 71:1429–1447.
- Sobrino, J.A., Jiménez-Muñoz, J.C., Sòria, G., Gómez, M., Ortiz, A. Barella, Romaguera, M., Zaragoza, M., Julien, Y., Cuenca, J., Atitar, M., Hidalgo, V., Franch, B., Mattar, C., Ruescas, A., Morales, L., Gillespie, A., Balick, L., Su, Z., Nerry, F., Peres, L. Libonati, R. (2008). Thermal remote sensing in the framework of the SEN2FLEX project: field measurements, airborne data and applications, *International Journal of Remote Sensing*, 29 (17), 4961 - 4991
- Stull, R.B., 1988. *An introduction to Boundary Layer Meteorology*, Kluwer academic Publishers, Dordrecht, 666 pp.
- Su, Z., 2002. The Surface Energy Balance System (SEBS) for estimation of turbulent heat flux. *Hydrology and Earth System Sciences*, 6, 85-99.
- Su, Z., Timmermans, W. J., van der Tol, C., Dost, R., Bianchi, R., Gómez, J.A., House, A., Hajsek, I., Menenti, M., Magliulo, V., Esposito, M., Haarbrink, R., Bosveld, F., Rothe, R., Baltink, H.K., Vekerdy, Z., Sobrino, J.A., Timmermans, J., van Laake, P., Salama, S., van der Kwast, H., Claassen, E., Stolk, A., Jia, L., Moors, E., Hartogensis, O., and Gillespie, A., 2009. EAGLE 2006 – Multi-purpose, multi-angle and multi-sensor insitu and airborne campaigns over grassland and forest. *Hydrology. Earth System Sciences*, 13, 833–845.
- Teuling, A.J., Seneviratne, S.I., Stöckli, R., Reichstein, M., Moors, E., Ciais, P., Luyssaert, S., van den Hurk, B., Ammann, C., Bernhofer, C., Dellwik, E., Gianelle, D., Gielen, B. Grünwald, Klumpp, K., Montagnani, L., Moureaux, C., Sottocornola, M., Wohlfahrt, G., 2010. Contrasting response of European forest and grassland energy exchange to heatwaves. *Nature Geosci.* Sept. 5, DOI: 10.1038/NGEO950.
- Thom, A.S., 1971. Momentum absorption by vegetation, *Quat. J. Roy. Meteorol. Soc.* 97, 414 – 428.
- Tiktak, A. and Bouten, W., 1992. Modelling soil water dynamics in a forested ecosystem, III. Model description and evaluation of discretization. *Hydrol. Processes* 6: 445–454.
- Tillman, J.E., 1972. The indirect determination of stability, heat and momentum fluxes in the atmospheric boundary layer from simple scalar variables during dry unstable conditions. *J. Appl. Meteorol.* 11, 783–792.
- Timmermans, W.J., Kustas, W.P., Anderson, M.C., French, A.N., 2007. An inter-comparison of the surface energy balance algorithm for land

- (SEBAL) and two-source energy balance (TSEB) modelling schemes. *Remote Sensing Environment*, 108, 369-384.
- Van der Maas, M.P., 1990. Hydrochemistry of two Douglas fir ecosystems and a heather ecosystem in the Veluwe, The Netherlands. Dutch Priority Programme on Acidification, 102.1-01. National Institute of Public Health and Environmental Hygiene (RIVM), Bilthoven, The Netherlands, 60 p.
- Van der Tol, C., van der Tol, S., Verhoef, A., Su, Z., Timmermans, J., Houldcroft, C. and Gieske, A.S.M., 2009. A Bayesian approach to estimate sensible and latent heat over vegetated land surface. *Hydrol. Earth Syst. Sci.* 13, 749-758.
- Van Dijk, A., Moene, A.F. and De Bruin, H.A.R., 2004. The principles of surface flux physics: theory, practice and description of the ECPACK library, Internal Report 2004/1, Meteorology and Air Quality Group, Wageningen University, Wageningen, The Netherlands, 99 pp.
- Van Heerd, R.M., Kuijlaars, E.A.C., Teeuw, M. P., van't Zand, R.J., 2000. Productspecificatie AHN 2000 (Rijkswaterstaat—Adviesdienst Geoinformatie en ICT, Report MDTGM 2000.13). Available online at: <http://www.ahn.nl>.
- Verhoef, A., McNaughton, K.G., and Jacobs A.F.G., 1997. A parameterization of momentum roughness length and displacement height for a wide range of canopy densities. *Hydrol. Earth Syst. Sci.*, 1, 81-91.
- Verhoef, W., 1985. Earth observation modeling based on layer scattering matrices. *Remote Sensing of Environment*, 17, 165-178.
- Verhoef, W., 1998. Theory of radiative transfer models applied in optical remote sensing of vegetation canopies. PhD Thesis, Wageningen Agricultural University, 310 pp.
- Verhoef, V., Bach, H., 2003. Simulation of hyperspectral and directional radiance images using coupled biophysical and atmospheric radiative transfer models. *Remote Sensing of Environment* 87, 23-41.
- Webster, R., Nortcliff, S., 1984. Improved estimation of micronutrients in hectare plots of the Sonning series. *Journal of Soil Science*, 35, 667-672.
- Weligepolage, K., Gieske, A.S.M. and Su, Z., 2012. Surface roughness analysis of a conifer forest canopy with airborne and terrestrial laser scanning techniques. *Int. J. Appl. Earth Observation and Geoinformation*, 14, 192-203.
- Wesely, M.I., 1988. Use of variance techniques to measure dry air-surface exchange rates. *Boundary-Layer Meteorol.* 44, 13-31.
- Wesson, K. H., Katul, G. and Lai, C.T., 2001. Sensible heat flux estimation by flux variance and half-order time derivative methods. *Water Resour. Res.* 37(9), 2333-2343.

- Wyngaard, J.C., Cote, O.R., Izumi, Y., 1971. Local free convection, similarity and the budgets of shear stress and heat flux. *J. Atmos. Sci.* 28, 1171-1182.
- Zobitz, J.M., Keener, J.P., Schnyder, H., Bowling, D.R., 2006. Sensitivity analysis and quantification of uncertainty for isotopic mixing relationships in carbon cycle research. *Agric. For. Meteorol.* 136, 56-75.

Bibliography

Summary

The main objective of this study is to integrate tower-based measurements with EO data for estimating spatially and temporally distributed surface variables of a forest canopy for improved quantification of surface-atmosphere interactions. This study mainly focuses on three of the most important surface variables for estimating surface fluxes, namely the aerodynamic roughness, land surface albedo and land surface temperature.

In *chapter 2*, a framework is presented for estimating aerodynamic roughness parameters: the momentum roughness length (z_0) and the displacement height (d_0) of a coniferous forest stand using remote sensing data. The specific objective of the study is to make use of high resolution Terrestrial Laser Scanning (TLS) data together with Airborne Laser Scanning (ALS) data to digitally map the upper canopy surface in order to generate high resolution digital Canopy Height Models (CHMs). The digital CHMs were subsequently used to extract surface geometric parameters of the upper canopy surface. Eventually the surface geometric parameters were used as input variables in the selected morphometric models to estimate aerodynamic roughness parameters. It was observed that the estimated values of z_0 and d_0 depend very much on the selected model. Comparison of model estimated roughness parameters against the literature values for similar surface types has shown that the technique can be successfully applied to estimate forest surface roughness by tuning some of the model parameters to resemble the forest structure of the study area.

Chapter 3 describes the use of these two aerodynamic methods to estimate momentum roughness length and displacement height of Douglas fir forest using simultaneous micrometeorological and flux measurements. When the flux-gradient method was used to objectively determine z_0 and d_0 , corrections for roughness sub-layer effects proved to be important. A new iterative method is employed to solve the set of equations when the corrections were made. In the absence of experimentally determined roughness sub-layer height, the corrections of Harman and Finnigan (2007) yielded the best overall estimates of aerodynamic parameters. Comparison with results of over 25 other studies has shown that the results obtained in this work fit the general trend rather well. Two quadratic relationships are proposed to predict d_0 and h_a based on the observed mean tree height. These simple relationships can be easily incorporated to large scale land surface models, provided that spatially distributed tree height information is available. The flux-variance technique is shown to be robust even when measurements are made in the roughness sub-layer. However the technique cannot be objectively used to estimate z_0 and d_0 as no explicit method exists to select the exact value for coefficient C_1 .

A detailed investigation of stand level surface albedo variability of a patchwork forest is presented in *chapter 4*. The top of the canopy reflectance in the visible and near-infrared domain retrieved from airborne and satellite imageries were integrated to estimate spatially distributed surface albedo while the tower-based radiation measurements in the solar-reflective region were used to obtain the temporal variation of surface albedo over a needleleaf forest canopy. The diurnal variation of surface albedo is consistent with the previous findings for needleleaf forest canopies. The spatial mean surface albedo values estimated from remote sensing data for needleleaf (pure Douglas fir), broadleaf (pure Beech) and mixed forest classes are 0.09, 0.13 and 0.11 respectively. Both visual characteristics and descriptive statistics indicate that with increased pixel size, the spatial variability of albedo progressively decreases. The semivariogram analysis was more insightful to perceive the nature and causes of albedo spatial variability in different forest classes in relation to sensor spatial resolution.

Finally a theoretical basis for directional LST estimation from top of the atmosphere radiance measurements is presented along with a spatio-temporal analysis of remotely sensed LST and concurrently carried out ground-based radiation together with contact temperature measurements in a Douglas fir forest. For the analysis we used remotely sensed TIR data from Airborne Hyperspectral Scanner to estimate spatially distributed LST of forested area. The AHS sensor, with 10 thermal bands covering the range between 8 and 13 μ m of the electromagnetic spectrum is an example of the new generation of airborne sensors with multispectral thermal infrared capabilities. The data acquired from the AHS sensors provided the opportunity to retrieve the directional LST of the forest canopy with a very high spatial resolution for both nadir and oblique view angles. Also the concurrent tower-based temperature measurements provided limited ground truth for a spatio-temporal analysis of surface temperature in an area covered with Douglas fir trees. The method adopted here for concurrent determination of LST and LSE is the widely-used TES algorithm together with the MODTRAN4 preprocessor for calculating the required atmospheric contributions. AHS derived average temperature values are generally in good agreement with the tower based component temperature measured at 24 m level whereas the component temperatures (trunk) measured at 17 m are consistently higher. It may be noted that in comparison with off-nadir radiometric temperature the TES method provides average LST with RMSE around 1.9K while the corresponding value with respect to component temperature measured at 24 m is around 1.4 K.

Samenvatting

Het doel van deze studie was om fysische grootheden van een bos beter te bepalen door middel van aardobservatiedata en metingen vanaf torens in het bos. Door het combineren van beide metingen kan de uitwisseling tussen bos en atmosfeer beter worden geschat in tijd en ruimte. Deze studie richt zich voornamelijk op drie van de belangrijkste grootheden, namelijk de aerodynamische ruwheid, het albedo en de oppervlaktetemperatuur.

In *hoofdstuk 2* wordt een kader gepresenteerd voor het schatten van twee aerodynamische parameters uit aardobservatie data: de ruwheidslengte voor moment (z_0) en de verplaatsingshoogte (d_0) van een naaldbos. Het doel is om de met behulp van laser scans op de grond ('Terrestrial Laser Scanning', TLS) met hoge resolutie in combinatie met laser scans vanuit een vliegtuig (airborne laser scanning, ALS) een kaart te maken van de hoogte van het naaldendak. Hieruit is een hoge resolutie digitaal kruinhoogtemodel (Canopy Height Model, CHM) gemaakt. Het CHM is vervolgens gebruikt om geometrische eigenschappen van het oppervlak van het bos af te leiden. Deze eigenschappen zijn tenslotte gebruikt als invoergegevens in morfometrische modellen die de aerodynamische ruwheidsgrootheden berekenen. Het bleek dat de geschatte waarden van z_0 en d_0 in behoorlijke mate afhingen van de keuze van het model. Uit een vergelijking met waarden uit de literatuur voor vergelijkbare oppervlaktes bleek dat de techniek goed gebruikt kan worden voor het afstemmen van parameters aan de structuur van het bos in het studiegebied, om zo de aerodynamische ruwheid nauwkeuriger te schatten.

Hoofdstuk 3 beschrijft het gebruik van deze twee aerodynamische methodes voor het schatten van de ruwheidslengte voor moment en de verplaatsingshoogte voor een Douglas spar plantage met gebruik van gelijktijdige micro-meteorologische metingen en metingen van fluxen. Correcties voor de ruwheidslaag bleken belangrijk bij de toepassing van de flux-gradiëntmethode. Een nieuwe methode is gebruikt voor deze correcties. In deze methode wordt een stelsel van vergelijkingen iteratief opgelost. De correcties van Harman en Finnegan (2007) toegepast. Deze bleken, bij gebrek aan experimentele waarden van de hoogte van de ruwheidslaag, de beste schattingen van de aerodynamische parameters op te leveren. Een vergelijking met 25 andere studies liet zien dat de resultaten van deze studie in overeenstemming zijn met de algemene trend. Verder zijn twee kwadratische relaties ontwikkeld waarmee d_0 en h_a kunnen worden berekend uit de gemiddelde hoogte van de bomen. Deze eenvoudige relaties kunnen gemakkelijk worden gebruikt in oppervlaktemodellen voor grote gebieden, mits de ruimtelijke verdeling van de hoogtes van de bomen bekend is. Er is aangetoond dat de flux-variantiemethode robuust is, zelfs wanneer de

metingen in de ruwheidslaag zijn gedaan in plaats van erboven. De techniek kan echter niet objectief worden gebruikt om z_0 en d_0 te schatten, omdat er geen methode bestaat om de exacte waarde van de coëfficiënt C_1 te bepalen.

Hoofdstuk 4 presenteert een gedetailleerde studie naar de variaties in het albedo in een heel bos dat eruit ziet als een lappendeken van soorten, leeftijden, dichtheden en boomsoorten. De weerkaatsing van zichtbare en nabij-infrarode straling is bepaald uit vliegtuigopnames en satellietbeelden. Deze beelden zijn samengevoegd om de ruimtelijke verdeling van het albedo te bepalen. Metingen vanaf een toren zijn gebruikt om de variaties in de tijd van het albedo in een naaldbos te meten. De dagelijkse gang van het albedo komt overeen met eerdere resultaten voor naaldbos. Het ruimtelijk gemiddelde albedo zoals geschat met aardobservatiedata was 0.09 voor naaldbos (Douglas spar), 0.13 voor loofbos (beuken), en 0.11 voor gemengd bos. Zowel visuele kenmerken als beschrijvende statistiek geven aan dat de ruimtelijke variabiliteit van het albedo progressief afneemt met toenemende pixelgrootte. De semi-variogramanalyse bleek het meeste inzicht te bieden in het karakter en de oorzaken van de ruimtelijke variabiliteit van het albedo in verschillende bostypes in verhouding tot de ruimtelijke resolutie van de sensor.

Tenslotte is een theoretische basis gelegd voor het schatten van oppervlaktetemperatuur (LST) uit directionele metingen van straling vanaf de top van de atmosfeer. Ook is een ruimtelijke en temporele analyse gemaakt van LST gemeten met een satelliet, en zijn er metingen verricht aan de temperaturen in een Douglas spar bos met thermistors die bevestigd waren aan naalden, stammen en bodem. Voor de analyse hebben we infrarode stralingsmetingen (TIR) gebruikt van de 'Airborne Hyperspectral Scanner (AHS)', een instrument dat op een vliegtuig is gemonteerd, om de ruimtelijke verdeling van LST in het bos te meten. De AHS sensor heeft 10 thermale (infrarode) banden tussen 8 en 13 μm in het elektromagnetische spectrum. De sensor is een voorbeeld van een nieuwe generatie van vliegtuigsensoren uitgerust met multi-spectrale infrarode detectoren. De data van de AHS sensoren maakten het mogelijk om directionele LST van het bos te extraheren met zeer hoge ruimtelijke resolutie. De metingen betroffen zowel loodrechte observaties als observaties onder een schuine hoek. Gelijktijdige metingen vanaf de toren leverden de aanvullende data voor een ruimtelijke en temporele analyse van oppervlaktetemperatuur in een Douglas spar bos. De methode die hier gebruikt is voor de bepaling van LST en LSE is het veelgebruikte TES algoritme, in combinatie met de MODTRAN4 pre-processor om de vereiste atmosferische bijdragen te berekenen. The gemiddelde temperatuur bepaald uit de AHS metingen kwam goed overeen met de veldmetingen op 24 meter hoogte, terwijl de contacttemperaturen gemeten op de stammen in het bos (op 17 m hoogte) consequent hoger waren. Het

TES algoritme schat the gemiddelde LST met een kwadratisch gemiddelde fout (RMSE) van ongeveer 1.9K, terwijl de kwadratisch gemiddelde fout van de LST gemeten in het veld met thermistors op 24 m hoogte ongeveer 1.4K was.

ITC Dissertation List

http://www.itc.nl/research/phd/phd_graduates.aspx